Morphology of alluvial fans

Pauline Delorme

UNIVERSITÉ SORBONNE PARIS CITÉ

USPC
Université Sorbonne
Paris Cité

Thèse préparée

à l'INSTITUT DE PHYSIQUE DU GLOBE DE PARIS
École doctorale STEP'UP- ED N°560
IPGP - Équipe de dynamique des fluides géologiques

Morphologie des cônes alluviaux

par
Pauline Delorme

présentée et soutenue publiquement le
2 octobre 2017

Thèse de doctorat de Sciences de la Terre et de l'environnement

dirigée par François Métivier
& Laurie Barrier

devant un jury composé de:

Bonnet Stéphane Professeur (GET- University de Toulouse)	Rapporteur
Lagrée Pierre-Yves Directeur de recherche (Institut Jean Le Rond ∂'Alembert)	Rapporteur
Ferrari Cécile Professeur (IPGP-PSS- Université Paris Diderot)	Examinatrice
Tal Michal Maître de conférence (CEREGE- Université Aix-Marseille)	Examinatrice
Barrier Laurie Maître de conférence (IPGP- Université Paris Diderot)	Co-encadrante de thèse
Métivier François Professeur (IPGP- Université Paris Diderot)	Directeur de thèse

Remerciements

Je tiens, tout d'abord, à remercier François et Laurie qui m'ont fait confiance et m'ont donné l'opportunité de réaliser cette thèse. Merci à Laurie qui m'a permis de faire le lien entre les cônes de laboratoire et les cônes naturels et à François dont l'enthousiasme quotidien est une grande source de motivation. J'ai eu la chance de profiter du savoir-faire d'Olivier, grâce à qui j'ai énormément appris sur l'art du travail bien fait (j'admets ne pas être sure d'avoir retenu toutes les règles...).

Je tiens aussi à remercier toutes les personnes qui ont contribué à ce travail, notamment les Éric(s): Éric Lajeunesse, toujours disponible pour une discussion autour du café du matin et Éric Gayer le roi du traitement de MNT ! Sans oublier Clément pour ses remarques toujours constructives bien que parfois désagréables (ou l'inverse...). Ainsi que Anaïs, de qui j'ai beaucoup appris au cours de nos nombreuses discussions que ce soit sur la biblio, les manips ou autres... Les expériences n'auraient jamais pu être mises en place sans l'expertise d'Angela, Hélène et Ramond.

Je souhaite aussi remercier tous les membres du laboratoire de DFG, qui contribuent à créer une très bonne ambiance de travail. Un merci particulier à Laura qui a accepté, sans trop râler, de partager mon bureau pendant ces trois années...

Merci aux membres du jury d'avoir accepté d'évaluer ce travail, ainsi qu'aux membres de mon comité de suivi de thèse dont les discussions annuelles ont fortement enrichi ce travail.

J'ai eu la chance au cours de cette thèse de partir deux mois au *Saint Anthony Falls Laboratory* à Minneapolis. Ainsi, je remercie tous ceux qui ont rendu ce projet possible, l'école doctorale STEP'UP qui a financé ce voyage et toutes les personnes qui m'ont accueillie sur place, Chris Paola, Vaughan Voller et Jean-Louis Grimaud.

Les deux années passées à faire de la médiation scientifique au Palais de la découverte ont été très enrichissantes. Merci donc à toute l'équipe géoscience du palais : Manue, Monica, Olivier, Arnaud et Vincent.

Mon aventure à l'IPGP a commencé bien avant mon arrivée en thèse je tiens donc à remercier toutes les personnes que j'ai pu croiser au cours de ma scolarité en licence ou en master (Sonia, Marianne, Seb, Sophie, Damian, Lilian, Lambert, Adélaïde, Laura, Audrey, Sarita, Florent) sans vous les cours n'auraient pas été aussi "agréables". Un merci particulier à Pichou : on a parcouru un sacré chemin depuis ce premier cours de math de L1 :p.

L'IPGP est aussi un lieu de rencontre où plein de générations de doctorants et post-docs se croisent, merci à tous les vieux et jeunes doctorants qui font de cet institut un lieu de travail si agréable, particulièrement aux "gens du 4" avec qui j'ai pu partager de nombreuses pauses.

Merci à toutes les personnes formidables que j'ai rencontrées durant ce moment de vie à l'IPGP. Tous vous nommer serait trop long, mais merci aux Vieux, au CDLM, aux gens de l'ENS, à ceux qui hantent l'IPGP le week-end et les jours fériés et à Thé-lepathie pour avoir été là durant cette dernière année même à distance. Merci spécial à Phil, Emmelyne, Céline et Yasmine qui ont pris le temps de relire ce manuscrit.

Enfin merci à ma famille, mes parents, frères et sœurs, qui m'ont toujours soutenue et encouragée. Un merci particulier aux deux autres géologues de la famille : Uncle Dom et Geneviève.

Résumé

Les cônes alluviaux sont des dépôts sédimentaires qui se mettent en place à la sortie des reliefs en érosion. Cette position leur confère un rôle d'archive sédimentaire. Leur géométrie est déterminée par les trois paramètres clés que sont le débit d'eau, la taille des sédiments et le débit de sédiment. Dans ce manuscrit, nous présentons trois séries d'expériences qui permettent de quantifier indépendamment l'influence de chacun des paramètres d'entrée sur la morphologie du cône. Nous montrons que le profil longitudinal du cône est contrôlé par la rivière qui le construit.

Lorsque le flux de sédiment est faible, la rivière alimentant le cône est au seuil de mise en mouvement des sédiments. En conséquence, sa pente, et donc celle du cône, dépendent uniquement de la taille des sédiments charriés et du débit d'eau. Cette pente augmente avec la taille des sédiments et diminue avec le débit d'eau.

Les cônes composés de sédiment de mobilité différentes permettent d'illustrer l'influence de la taille des sédiments sur leur pente. Dans nos expériences, à l'instar des cônes naturels, le dépôt est ségrégé: les sédiments les moins mobiles se déposent en amont du cône, où la pente est plus forte. Cette ségrégation nous permet d'estimer la composition du mélange initial à partir de la géométrie du dépôt.

Enfin, nous avons montré que lorsque le débit sédimentaire augmente, la pente du cône s'élève au dessus de sa valeur seuil. Dans ce cas, puisque la rivière dépose les sédiments, le débit sédimentaire diminue vers l'aval, ce qui induit un profil concave. Nous montrons ainsi que la pente proximale du cône enregistre la valeur de ce débit sédimentaire.

Finalement, nous présentons des résultats préliminaires permettant de prendre en compte l'enregistrement de la variation des forçages dans la stratigraphie du cône, et envisageons des pistes pour appliquer ces observations aux cônes naturels.
Mots clefs: cône alluvial, rivière, seuil de mise en mouvement, archive sédimentaire

Abstract

Alluvial fans are sedimentary deposits growing at the outlet of drainage areas. This position makes them valuable sedimentary records. Three key parameters determine their geometry: the water discharge, the sediment size and the sediment discharge. In this manuscript, based on three series of experiments, we quantify independently the influence of each parameter on the structure of the deposit. We find that the morphology of the fan is controlled by the river that builds it.

For a low sediment discharge, the river that feeds the fan is at the threshold of sediment motion. As a result, its slope, and therefore that of the fan, depend only on the size of the sediment and on the water discharge. The slope increases with sediment size and decreases with water discharge.

Experimental alluvial fans composed of bimodal sediment, like to their natural counterparts, are segregated. The less mobile sediments are deposited first, near the fan apex, where the slope is steeper. This segregation allows us to estimate the composition of the sediment mixture from the fan geometry.

When the sediment discharge injected at the apex increases, the slope of the fan departs from its threshold value. Sediments are deposited along the fan, thus causing the sediment discharge to decrease downstream, generating a concave profile. As a consequence, the proximal slope of the fan records the sediment discharge.

Finally, we present preliminary results showing how the stratigraphy of the fan records variations of the forcing (sediment and water discharges). We then discuss the applicability of these observations to the natural fans.
Key words: alluvial fan, river, threshold of motion, sedimentary record

Table des matières

Contents

Introduction

Les surfaces continentales sont le lieu d'interactions complexes entre les phénomènes tectoniques et climatiques. Leur évolution est contrôlée par l'action de l'érosion et du dépôt de sédiment. La dénudation des reliefs, par des processus d'altération et d'érosion, permet la production de sédiment. Ces sédiments sont ensuite transportés depuis les reliefs jusqu'aux zones de dépôts par différents processus : transport fluviatile, glissement de terrains, coulée de boue. Au niveau des surfaces continentales, la majorité de la matière érodée est transportée par les rivières vers des bassins sédimentaires intracontinentaux ou océaniques (Allen, 2009). Cependant, le long de leur parcours les rivières peuvent rencontrer des zones de stockage, dans lesquelles les sédiments peuvent s'accumuler pendant des périodes de temps plus ou moins longues (Romans et al., 2016). Pour quantifier les transferts de masse ayant lieu à la surface terrestre, il est nécessaire de comprendre les mécanismes à l'origine de l'érosion, du transport et du dépôt des sédiments.

La compréhension de ces processus passe par l'étude d'objets sédimentaires ayant préservés des marqueurs du transfert de sédiments. À la sortie des bassins versants, on observe souvent la formation d'un dépôt sédimentaire de forme circulaire : le cône alluvial. Les cônes alluviaux permettent l'accumulation et la préservation d'une grande partie de la charge sédimentaire (celle transportée par charriage). Leur position à la sortie des reliefs pourrait donc permettre de reconstituer les flux émanant de ceux-ci.

Dans le cadre de cette thèse, nous nous sommes donc concentrés sur l'étude des cônes alluviaux. En particulier, nous avons essayé de mettre en évidence les relations entre les forçages (débit d'eau, débit de sédiment et taille des sédiments) et la morphologie des cônes construits en aval. L'idée est donc de mettre en évidence les informations, enregistrées dans les dépôts des cônes alluviaux, qui pourraient permettre de reconstruire les paramètres ayant conduits à leur formation. Pour ce faire, nous avons choisi d'utiliser l'approche expérimentale qui permet de considérablement réduire les échelles de temps et d'espace, ainsi que de contrôler les paramètres d'entrée.

Les résultats obtenus par cette étude sont présentés dans ce manuscrit sous la forme de six chapitres. Le premier chapitre fait une synthèse des connaissances. Les trois chapitres suivants sont chacun consacrés à l'étude d'un paramètre en particulier dans des conditions simplifiées (paramètres d'entrée maintenus constants). Les deux suivants proposent d'utiliser les résultats des premiers chapitres, pour étudier des cas plus proches de la réalité.

Dans le premier chapitre, nous proposons un état des connaissances sur les cônes alluviaux. Nous définissons le cône alluvial et présentons les relations connues entre la morphologie des cônes alluviaux et les paramètres d'entrées (débit d'eau, débit de sédiment et taille des sédiments). Il existe déjà de nombreuses études visant à quantifier l'influence de ces paramètres sur

la morphologie et la dynamique des cônes alluviaux, cependant celles-ci reposent souvent sur des lois empiriques déterminées à partir de cas particuliers. Elles ne sont donc pas généralisables. Ce constat nous permet de présenter les objectifs de ce travail (Chapitre 1).

Le second chapitre est focalisé sur l'étude de l'influence du débit d'eau et de la taille des sédiments. En utilisant une approche expérimentale, nous montrons que lorsque le débit de sédiment alimentant le cône alluvial est très faible, la pente du cône atteint une valeur seuil. Cette pente seuil est déterminée par le débit d'eau et la taille des sédiments alimentant le cône (Chapitre 2).

Dans le troisième chapitre, toujours en s'appuyant sur une démarche expérimentale, nous mettons en évidence l'influence de la composition des sédiments alimentant le cône sur sa morphologie. Nous nous intéressons au cas d'un cône construit par deux types de sédiments, et montrons une corrélation entre la géométrie du dépôt sédimentaire et la nature des sédiments. Cette description géométrique permet de contraindre la composition initiale du mélange sédimentaire (Chapitre 3).

Le quatrième chapitre reprend le dispositif expérimental utilisé dans le second chapitre, afin d'étudier l'influence du débit sédimentaire sur la pente du cône. Nous montrons que lorsque ce débit augmente, la pente du cône s'éloigne de sa valeur seuil. Cet écart au seuil génère la formation d'un profil concave (Chapitre 4).

Dans le cinquième chapitre, nous étudions numériquement les modifications enregistrées dans la stratigraphie et la géométrie du cône alluvial lorsque les paramètres d'entrée, débit d'eau et composition du mélange sédimentaire, varient (Chapitre 5).

Pour finir, le sixième chapitre présente des pistes pour appliquer nos résultats aux objets naturels. Pour ce faire, nous étudions des cônes naturels, déjà bien documentés dans la littérature, afin de mettre en évidence les données qu'il est nécessaire d'acquérir sur le terrain pour reconstruire les paramètres d'entrée (Chapitre 6).

Les démarches expérimentales ainsi que les techniques d'acquisitions des données sont présentées en annexe.

Chapitre 1

État de l'art

1.1 Les cônes alluviaux

Les cônes alluviaux sont des dépôts sédimentaires qui se mettent en place à la sortie de bassins versants en érosion (Fig. 1.1). Lorsqu'un écoulement fluvial ou gravitaire, chargé en sédiment, atteint une zone plane, le changement de pente associé provoque le dépôt des sédiments. L'écoulement, n'étant plus confiné dans une vallée, peut s'écouler radialement dans toutes les directions à partir de l'apex (point amont à partir duquel la rivière émerge du relief). Le dépôt, formé en aval, acquiert une forme caractéristique de portion de cône, d'angle d'ouverture Θ et de rayon R (Drew, 1873; Bull, 1977; Rachocki and Church, 1990; Blair and McPherson, 1994, 2009, Fig. 1.1b).

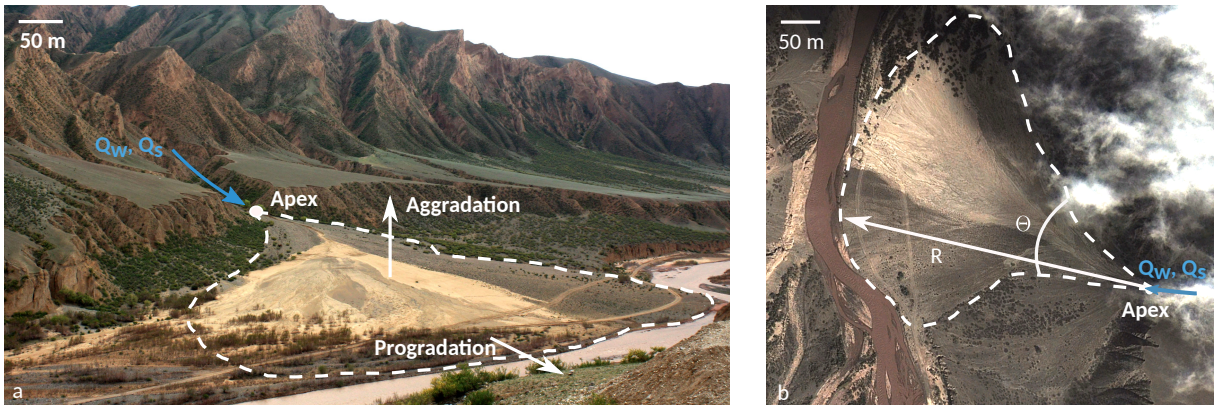

FIGURE 1.1 : Cône alluvial Tian Shan, Chine. a) Vue de face. b) Photo aérienne Google Earth. Lignes pointillées : contour du cône. Les dépôts les plus clairs sont les plus récents.

On trouve des cônes alluviaux sur toute la surface du globe quel que soit le contexte tectonique et climatique (Weissmann et al., 2010). Ils sont regroupés en trois catégories définies principalement par les processus de transport et de dépôt des sédiments (Stanistreet and McCarthy, 1993; Galloway and Hobday, 1996). En suivant la classification de Stanistreet and McCarthy (1993), on distinguera trois types de cônes alluviaux (Fig. 1.2)

- Les cônes de débris (Fig. 1.2a). Ces cônes sont les plus petits avec une étendue radiale comprise entre 1 et 20 km. Ils sont également les plus pentus avec une pente pouvant atteindre 15°. Ils sont principalement constitués de sédiments grossiers et leur surface est

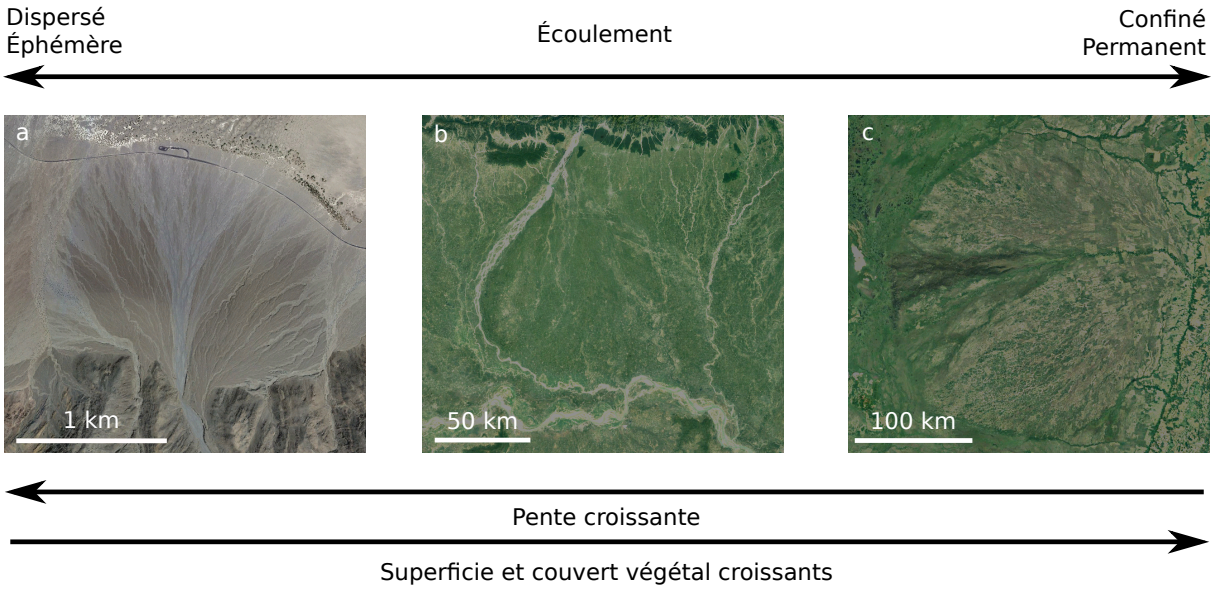

FIGURE 1.2 : Classification des différents types de cône. a) Cône de débris, Grotto canyon, Vallée de la Mort, USA. b) Cône chenalisé en tresse, la Kosi, Inde. c) Cône à écoulement méandriforme, le Taquari, Brésil. Images Landsat issues de *Google Earth*.

très peu végétalisée. Leur mode de formation est lié à des processus gravitaires (coulées de boue et de débris) ne faisant intervenir qu'occasionnellement le transport de sédiments par les rivières. Ce type de cônes ne sera pas considéré dans cette étude.

- Les cônes chenalisés en tresse (Fig. 1.2b). Ces cônes sont alimentés par une rivière en tresse formant des barres longitudinales et transversales. Ils ont généralement une étendue radiale allant de la dizaine à la centaine de kilomètres et des pentes moyennes pouvant varier de 0.1° à 2°. On observe souvent de la végétation sur les berges des chenaux. On distingue deux cas, tout d'abord les cônes avec des écoulements chenalisés en tresse peu profonds. Ces écoulements forment des cônes petits avec une pente forte et transportent principalement des graviers. On les trouve majoritairement dans les zones semi-arides. Les cônes du Tian Shan en Chine font, par exemple, partie de cette catégorie (Guérit, 2014). À l'autre extrémité de cette catégorie on trouve les cônes avec des écoulements chenalisés en tresse profonds qui ont des pentes plus faibles et une grande étendue radiale. Ces cônes transportent principalement des sédiments fins et se mettent en place dans des zones humides (Saito and Oguchi, 2005). Un exemple type est le cône de la Kosi, Inde.

- Les cônes chenalisés à écoulement méandriformes aussi appelés « *Losimean* »(Low sinuosity meandering) (Fig. 1.2c). Ces cônes représentent une extrémité du spectre des cônes alluviaux. Ce n'est qu'après l'étude de McCarthy (1993) sur le cône de l'Okavango qu'ils ont été classifiés en tant que cônes alluviaux. Ils sont généralement très étendus radialement ($R \geqslant 150$ km) avec une pente très faible ($S \leqslant 0.1°$). Leur surface est végétalisée et présente des chenaux bien identifiés. On les trouve préférentiellement dans des zones humides et en extension.

Les cônes alluviaux se mettent en place à l'intersection entre les zones en érosion et les zones de

dépôts. Ces espaces peuvent être localisés à la confluence entre deux rivières ou dans des bassins sédimentaires. Dans le premier cas, le dépôt sera de taille limitée et ne sera pas préservé sur de longues échelles de temps. Au contraire, les bassins sédimentaires permettent la formation de plus grands cônes qui sont préservés sur des échelles de temps beaucoup plus longues. Dans ce cas-ci l'espace disponible pour l'accumulation des sédiments est donc contrôlé par l'action des failles qui engendrent la surélévation d'un bloc par rapport à un autre (Ritter et al., 1995). Dans le cas où le cône se jette dans une étendue d'eau (lac ou océan), l'espace disponible pour la sédimentation est contrôlé par les variations du niveau d'eau. Les cônes alluviaux sont construit par l'apport d'un flux sédimentaire, Q_s, transporté depuis un relief par une rivière, de débit Q_w. Ces trois facteurs (espace disponible pour la sédimentation, débits d'eau et de sédiment) représentent les conditions aux limites qui contrôlent la formation des cônes alluviaux (Rachocki and Church, 1990). Géométriquement, un cône alluvial est caractérisé (1) par son rayon R, qui représente la distance depuis l'apex au pied du cône, (2) un angle d'ouverture Θ qui en fonction de l'espace disponible peut s'étendre latéralement jusqu'à 180° (Fig. 1.1), et (3) son profil d'élévation h à partir duquel il est possible d'estimer la pente S du cône. Le rayon du cône ainsi que son angle d'ouverture sont principalement contrôlés par l'espace disponible verticalement et latéralement pour le dépôt des sédiments, tandis que la pente dépend majoritairement des flux (Q_w et Q_s) ainsi que des caractéristiques des sédiments transportés (leur taille d_s et leur densité ρ_s) (Rachocki and Church, 1990; Blair and McPherson, 2009).

Afin de différencier les cônes alluviaux des autres systèmes fluviaux, tels que les rivières alluviales ou les deltas, Blair and McPherson (1994) mettent en évidence les caractéristiques morphologiques qui les définissent. Le profil transverse des cônes alluviaux présente une forme convexe (Fig. 1.3c). Cette forme est une conséquence directe de l'axis-symétrie du dépôt. Le profil radial des cônes présente généralement une forme concave (Fig. 1.3b). La forme de ce profil radial

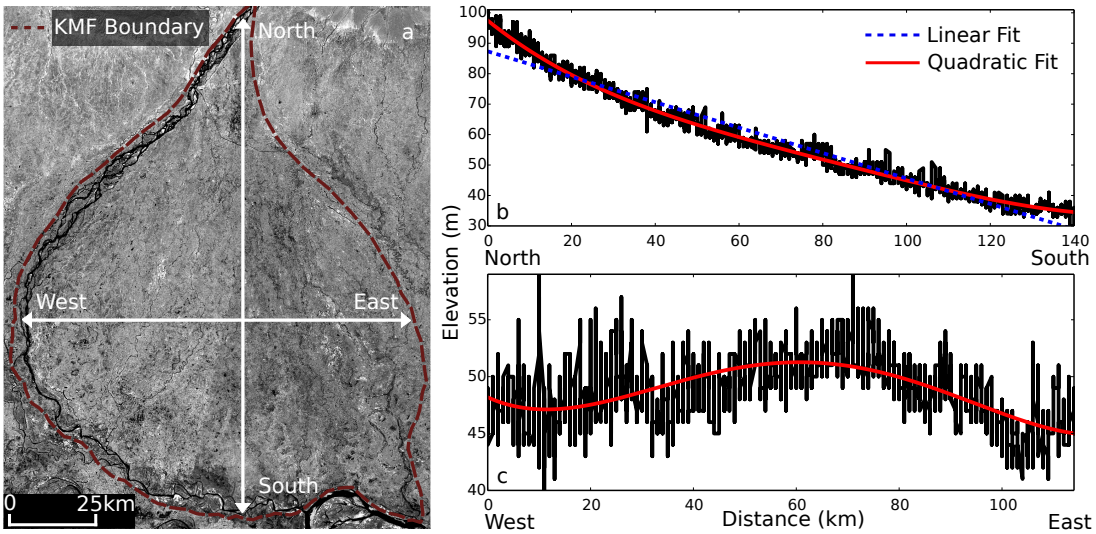

FIGURE 1.3 : (a) Image Landsat du cône de la Kosi (Inde) montrant la localisation de (b) un profil topographique radial (Nord - Sud), et (c) un profil topographique transverse (Est - Ouest). Données SRTM (source : Earth Explorer). *D'après Gaurav (2016).*

peut toutefois varier d'un cône à l'autre en fonction des conditions dans lesquelles il se forme. En

effet, Bull (1964) et Blair (1987a) mettent en évidence trois types de profil radial : (a) une pente relativement constante, (b) une pente qui diminue progressivement le long du cône, et (c) une pente composée de plusieurs segments linéaires dont la pente diminue vers l'aval. Les cônes ayant une pente constante sont associés à un processus de formation simple dans lequel les paramètres d'entrée (flux d'eau et de sédiments et tailles des sédiments) restent constants. Le profil concave des cônes est souvent expliqué soit par une diminution progressive de la taille des grains le long du cône, soit par une diminution du flux de sédiment en aval du cône (Stock et al., 2008). Les cônes segmentés, qui ont une pente composée de plusieurs segments, ont un profil également concave similaire à celui engendré par une diminution progressive de la taille des grains, excepté que leur pente présente des ruptures nettes qui sont généralement associées à un changement brutal de la taille des sédiments transportés (Bull, 1964). Ces profils sont caractéristiques des cônes composés de mélanges de graviers et de sables qui présentent une transition nette entre des dépôts grossiers en amont et des dépôts plus fin en aval (Miller et al., 2014).

Les cônes alluviaux sont des objets dynamiques qui évoluent dans le temps et dans l'espace. À grande échelle de temps, l'échelle de la formation du cône, le rayon R des cônes croît (progradation) et leur surface h s'élève (aggradation), sous l'effet du dépôt de sédiment (Rachocki and Church, 1990; Harvey et al., 2005, Fig. 1.1). À plus courte échelle de temps, celle de la mobilité de la rivière, les sédiments remplissent le chenal en commençant par la partie aval du cône. Ce front de remplissage remonte ensuite progressivement vers l'amont. Le dépôt des sédiments dans le chenal provoque ainsi une surélévation du lit. En conséquence, la rivière change d'orientation pour s'écouler en direction de la pente la plus forte, on parle alors d'avulsion (Field, 2001; Slingerland and Smith, 2004; Sinha, 2009). Un nouveau chenal se met ensuite en place et le cycle se répète. Ces cycles sont autogéniques : ils se mettent en place à la surface des cônes spontanément sans variation des conditions aux limites. La succession de ces cycles maintient l'équilibre du cône (Fraser and DeCelles, 1992). Entre deux phases chenalisées, on peut observer une période où l'écoulement n'est pas localisé, et forme une nappe qui recouvre entièrement ou partiellement la surface du cône (Decelles et al., 1991). La mobilité de l'écoulement se caractérise par la présence simultanée de zones actives et inactives à la surface du cône (les zones claires représentent la zone active, Fig. 1.1). L'axis-symétrie du cône est maintenue par les phénomènes d'avulsion qui permettent à des zones inactives de devenir actives et inversement (Gómez-Villar and Garcıa-Ruiz, 2000).

1.2 Reconstitution des paléo-flux

Les cônes alluviaux sont situés à l'interface entre les zones en érosion (reliefs), et les zones en sédimentation (vallées et plaines alluviales). Cette position en fait les premières archives sédimentaires à la sortie des reliefs terrestres (Hinderer, 2012; Latrubesse, 2015). On peut donc tenter, en les étudiant, de reconstruire les paléo-flux ayant permis leur mise en place. La quantification des flux sédimentaires, émanant des reliefs terrestres, est essentielle pour comprendre les transferts de masse sur les continents et à une échelle plus petite, l'histoire des topographies dont ils sont issus (Métivier and Gaudemer, 1997; Kuhlemann et al., 2002). La technique la plus utilisée pour reconstituer les paléo-flux sédimentaires est, à l'heure actuelle, la reconstruction volumique (Kiefer et al., 1997; Jayko, 2005; Jolivet et al., 2014; Guerit et al., 2016). L'utilisation de cette

technique nécessite d'avoir accès à deux types d'informations ; (a) une cartographie 3D du dépôt, et (b) l'âge du dépôt.

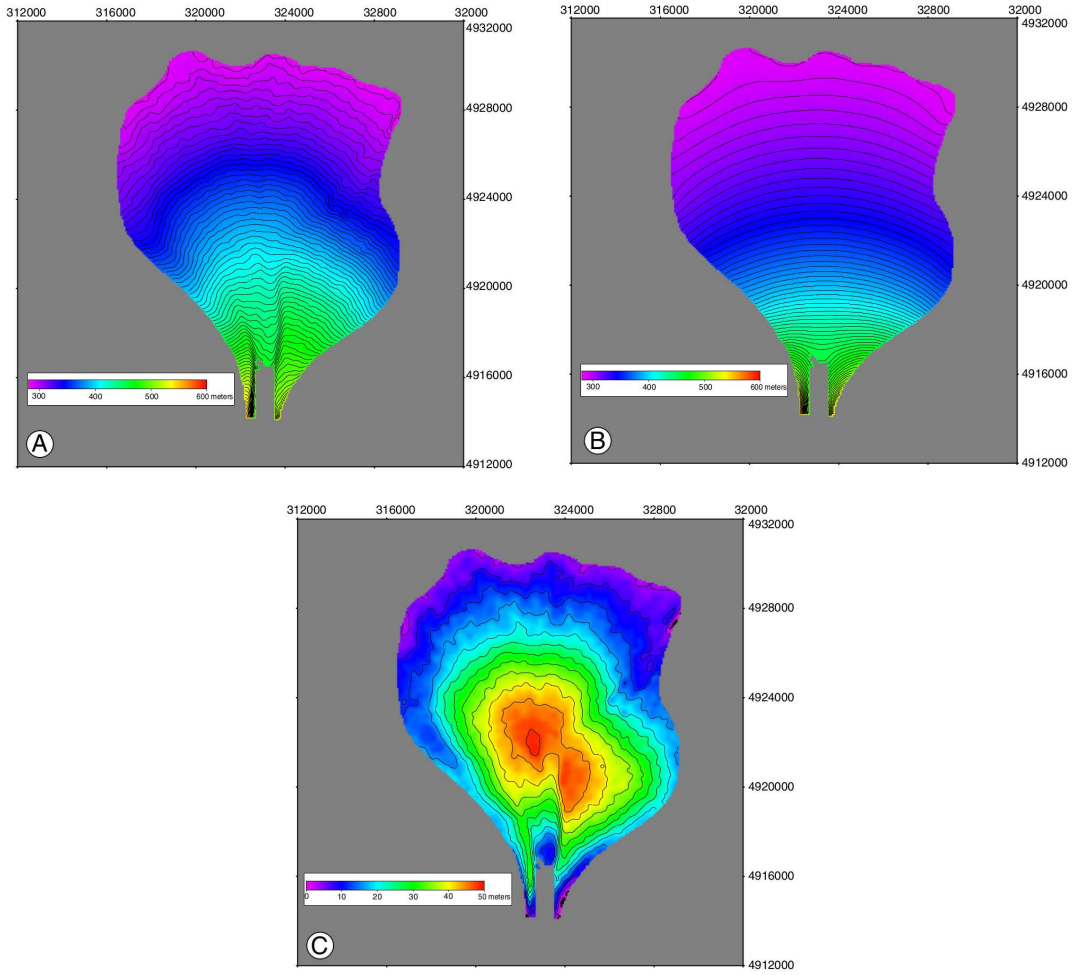

FIGURE 1.4 : Mesure du volume de sédiment stocké dans le cône alluvial Holocène de Kuitun (Tian Shan, Chine). A) Modèle numérique de terrain de la topographie actuelle du cône, données SRTM3. B) Topographie de la base du cône Holocène estimée à partir de la pente du cône Pléistocène. C) Différence d'altitude entre A) la topographie actuelle et B) la base du cône. Cette différence correspond à l'épaisseur de sédiments stockée pendant l'Holocène. *D'après Jolivet et al. (2014)*

Les cônes alluviaux présentent l'avantage d'être bien délimités spatialement. L'estimation du volume des dépôts peut donc être effectuée en utilisant des modèles numériques de terrain (DEM). Cependant, en fonction du contexte tectonique dans lequel un cône est construit, sa reconstruction 3D à partir de sa surface peut s'avérer inexacte. En effet, l'extrapolation directe du volume du cône à partir de sa surface suppose que celui-ci est construit sur une surface plane, ce qui n'est souvent pas le cas. Pour estimer le volume du dépôt le plus précisément possible, il est nécessaire d'avoir accès à la topographie de la base sur laquelle il repose (Jayko, 2005; Jolivet et al., 2014; Guerit et al., 2016, Fig. 1.4). Une fois le volume de sédiment connu, il est alors nécessaire de connaître l'âge du dépôt pour avoir accès au flux. La période d'activité des cônes alluviaux peut, par exemple, être estimée par des méthodes radiochronologiques, ou encore en

utilisant les isotopes cosmogéniques, tels que le ^{10}Be (France-Lanord et al., 2001).

En ayant accès à toutes ces informations, il est possible d'estimer les paléo-flux sédimentaires en utilisant la relation suivante (Guérit, 2014),

$$Q_s = \frac{V(1-\lambda)}{fP}, \tag{1.1}$$

où Q_s est le flux de sédiment émanant du relief, V le volume du cône alluvial, λ la porosité des sédiments, f la fraction de la charge sédimentaire transportée par la rivière qui est déposée dans le cône, et P la période d'activité du cône. Dans l'équation (1.1), la fraction de sédiment piégée dans le cône, f, est encore mal contrainte et rarement évaluée (Kiefer et al., 1997; Oguchi, 1997; Jolivet et al., 2014). Pour simplifier, on considère généralement que f, la fraction sédimentaire déposée dans le cône, correspond à la fraction du flux sédimentaire transportée en charge de fond (Guerit et al., 2016). Malgré ces incertitudes la reconstruction volumétrique permet d'estimer l'ordre de grandeur du taux de dénudation des bassins versants alimentant les cônes étudiés, si l'aire de ces derniers est connue.

Pour reconstruire l'histoire climatique d'une région, il est également nécessaire de quantifier les paléo-flux d'eau (McDonald et al., 2003; Leier et al., 2005; Davidson and Hartley, 2010; Waters et al., 2010). Trois méthodes sont principalement utilisées pour estimer les caractéristiques de l'écoulement à partir des dépôts formés : (a) l'analyse de la géométrie de l'écoulement (largeur, profondeur), (b) l'étude des formes sédimentaires présentes dans les chenaux (dunes, rides) et (c) la détermination du seuil de mise en mouvement des sédiments (Métivier and Barrier, 2010, et références incluses). Ces trois méthodes dépendent souvent de relations empiriques déterminées à partir de cas particuliers et ne sont donc pas généralisables.

Dans tous les cas, l'estimation des paléo-flux par les méthodes énoncées précédemment nécessite d'avoir accès à de nombreux paramètres (morphologie du chenal, taille des sédiments, période d'activité...) ce qui ne permet pas de proposer une méthode généralisée qui s'appliquerait à tous les cônes alluviaux. Or il a depuis longtemps été démontré (du moins qualitativement) que la morphologie des cônes alluviaux (notamment leur profil radial) est fortement influencée par les trois paramètres clés que sont : le débit d'eau Q_w, la taille des sédiments d_s et le débit de sédiment Q_s (Le Hooke and Rohrer, 1979; Parker et al., 1998a; Whipple et al., 1998). Ces trois paramètres sont dépendants, à plus grande échelle par la tectonique et le climat (Lustig, 1965; Blair, 1987b). Dans la section suivante, nous passerons brièvement en revue les relations existantes entre la morphologie des cônes et ces différents paramètres afin de mieux comprendre comment reconstituer les paléo-flux à partir de la morphologie actuelle des cônes alluviaux.

1.3 Relation entre morphologie et forçages

Sur le terrain, l'influence de chacun des paramètres est difficile à quantifier, d'une part parce que les mesures en elles-mêmes sont difficiles à réaliser et d'autre part parce que la variation des paramètres se fait souvent de manière simultanée. Il est donc compliqué d'isoler leur influence respective. Ces études sont donc complétées par des études expérimentales et théoriques dans lesquelles chacun des paramètres peut être étudié indépendamment. De plus, l'utilisation de modèles à petite échelle permet de réduire considérablement l'échelle de temps nécessaire à la

formation d'un cône alluvial (Schumm et al., 1987; Paola et al., 2009; Clarke, 2015).

En laboratoire, les modèles expérimentaux sont conçus en rapport avec les paramètres que l'on veut étudier. C'est, par exemple, dans l'optique d'étudier l'influence de la tectonique et des variations eustatiques sur la mise en place de bassin sédimentaire que l'*« Experimental Earthscape Facility (XES) Basin »* a été conçu au *Saint Anthony Falls Laboratory* (Fig. 1.5a). Ce dispositif, unique en son genre, permet de créer des zones de subsidence à l'aide de pistons qui déforment la surface sur laquelle le dépôt se forme. Un drain disposé à l'extrémité du bassin permet également d'ajuster le niveau de base de la rivière (Paola et al., 2001; Heller et al., 2001). Pour étudier

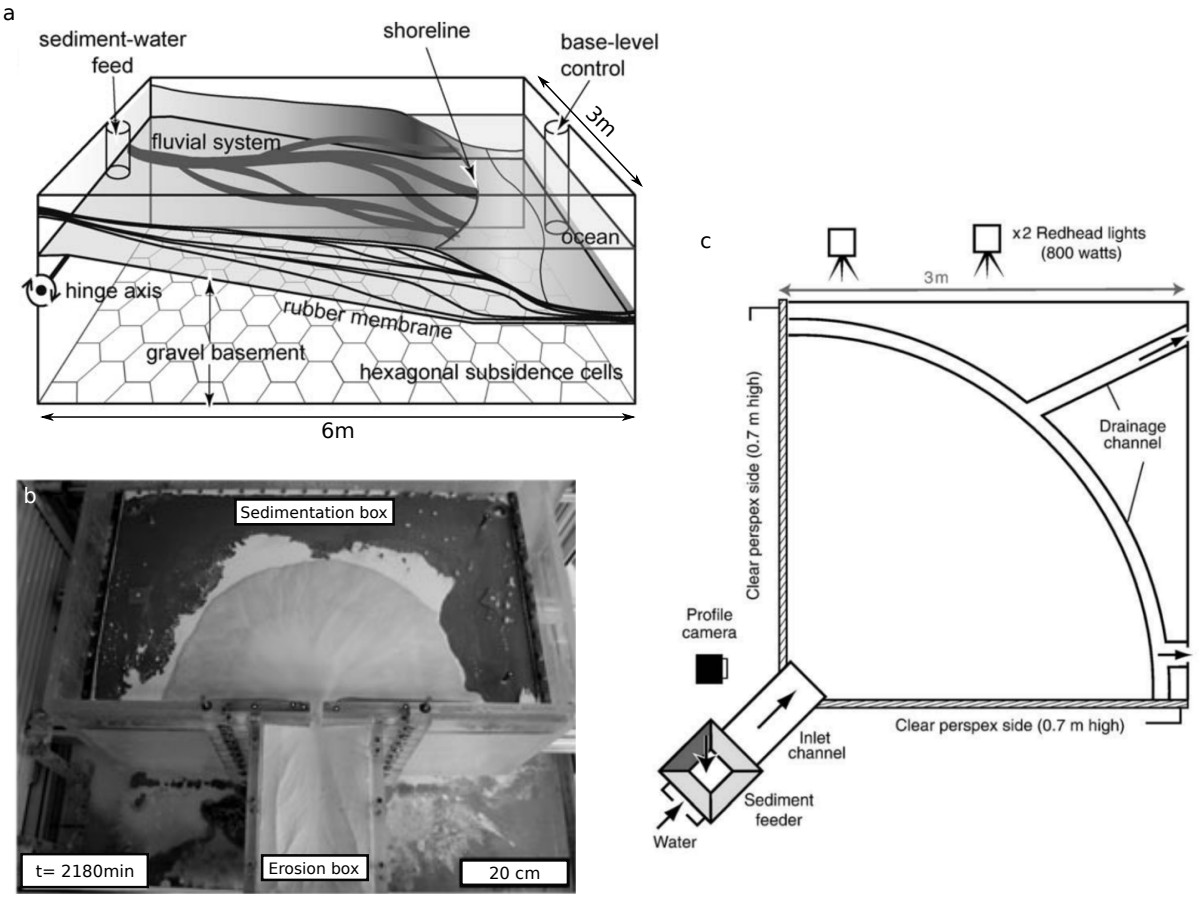

FIGURE 1.5 : Exemple de dispositifs expérimentaux utilisés. a) L'*« Experimental Earthscape Facility (XES) Basin »* (Kim et al., 2006). b) Le système couplé bassin versant cône alluvial utilisé par Rohais et al. (2012). c) Le dispositif utilisé par Clarke et al. (2010).

l'influence de la quantité de pluie, et donc du climat, sur la formation des cônes alluviaux, le laboratoire *Géosciences Rennes* a, quant à lui, développé un système couplant bassin versant et cône alluvial (Rohais, 2007, Fig. 1.5b). Ce dispositif est constitué de deux boites : Une première boite en érosion qui peut être surélevée pour simuler une surrection tectonique. Cette boite est placée sous un brumisateur pour simuler la pluie. Les sédiments érodés dans cette boite sous l'action de la pluie sont transportés jusqu'à une deuxième boite, en sédimentation, dans laquelle ils se déposent. Cette boite en sédimentation peut être abaissée pour simuler une subsidence. Enfin, il existe de nombreux systèmes expérimentaux conçus sans la possibilité de faire varier l'espace disponible pour la mise en place du dépôt, par exemple ceux de Whipple et al. (1998)

et Clarke et al. (2010) (Fig. 1.5c). Ces dispositifs sont conçus pour comprendre l'influence des paramètres tels que les flux (Q_w et Q_s) et la taille des grains (d_s). Le cône se construit sur une surface plane qui n'est pas mobile. L'angle d'ouverture latérale de ces dispositifs peut varier d'un modèle à l'autre et atteindre 180°.

1.3.1 La tectonique et le climat

Les variations tectonique et climatique impactent la formation des cônes alluviaux en modifiant les conditions aux limites à différentes échelles. Tout d'abord, à l'échelle régionale, la tectonique et le climat contrôlent l'espace disponible pour la mise en place des cônes alluviaux. En effet, comme nous l'avons vu précédemment, les grands cônes alluviaux se construisent dans des espaces créés par l'action des failles et/ou la diminution du niveau de base (Blair, 1987b; Whipple and Trayler, 1996; Harvey, 2002; Pang et al., 2016). Lorsque l'espace disponible pour la sédimentation varie, les frontières du cône évoluent simultanément. Ainsi, les variations tectonique et climatique peuvent être enregistrées dans la stratigraphie du cône par la progradation et la rétrogradation des dépôts du cône (Horton et al., 2004; Hartley et al., 2005; Harvey, 2005; Whittaker et al., 2011). Une diminution du niveau de base peut aussi provoquer l'incision du cône (Waters et al., 2010; Pope et al., 2016).

Des modélisations numériques et expérimentales corroborent ces observations de terrain (Muto et al., 2016). En utilisant les équations de conservation de la masse, Whipple and Trayler (1996) montrent que la taille des cônes alluviaux est contrôlée principalement par les événements tectoniques, les variations climatiques n'ayant qu'une influence secondaire. L'incision et la formation de terrasses peuvent être reproduites en laboratoire en imposant un abaissement continue du niveau de base (Muto and Steel, 2004). À l'aide de modélisations numériques combinant le bassin en érosion et la zone de dépôt, plusieurs études mettent en évidence la signature stratigraphique (progradation et rétrogradation du front de sédiments grossiers) des événements climatiques et tectoniques (Coulthard et al., 2002; Clevis et al., 2003; Armitage et al., 2011).

À l'échelle du bassin versant, la tectonique et le climat agissent conjointement sur les flux d'eau et de sédiment qui atteignent l'apex du cône (Bonnet and Crave, 2003). En effet, la surrection du relief favorisera une érosion plus forte en mettant plus de matériel à disposition, tandis que lors d'un période glaciaire les flux d'eau seront plus faibles, limitant l'érosion et donc le flux de sédiment (Frostick and Reid, 1989). Les études de terrain montrent que les alternances entre érosion (incision du cône) et dépôt (aggradation du cône) sont corrélées aux cycles glaciaires (Weissmann et al., 2005; Guerit et al., 2011; Cesta and Ward, 2016). Enfin, les variations climatiques affectent la végétation et ainsi modifie la capacité du sol à produire des sédiments (Lustig, 1965; Macklin et al., 2002; Candy et al., 2004; Harvey, 2005).

Nous avons vu que les variations tectoniques et climatiques produisent des variations des paramètres d'entrée dont les signatures ne sont pas aisément distinguables dans la stratigraphie du cône. Pour distinguer les effets climatiques et tectoniques, il est nécessaire de considérer les échelles de temps auxquelles ils agissent. En utilisant un modèle numérique, Paola et al. (1992a) suggèrent qu'il existe une échelle de temps caractéristique de réaction aux variations, qui dépend des dimensions de l'objet sédimentaire. Ainsi, ils montrent que la réponse du système à une perturbation tectonique est plus lente que pour une perturbation climatique. En conséquence, les

variations tectoniques ne seront enregistrées dans la stratigraphie que si celles-ci se produisent sur des échelles de temps supérieures à l'échelle caractéristique. Une variation brutale due à un séisme, par exemple, sera difficilement observable dans la stratigraphie (Allen and Densmore, 2000; Marr et al., 2000). Au contraire, le système réagit plus rapidement au variations climatiques, un signal haute fréquence dans la stratigraphie est donc interprété comme le marqueur de variations climatiques (Allen and Densmore, 2000).

Enfin, à l'échelle du cône alluvial et de son basin versant, la tectonique et le climat contrôlent principalement les paramètres d'entrée (taille des sédiments, d_s, flux d'eau, Q_w, et de sédiment, Q_s). Il est donc indispensable de comprendre comment ces paramètres influencent la morphologie et la stratigraphie des cônes pour pouvoir a posteriori reconstruire les paléo-flux.

Dans les sections suivantes, nous présentons brièvement l'état des connaissances concernant l'influence de ces trois paramètres sur la dynamique de croissance et la morphologie des cônes alluviaux, afin d'introduire les objectifs de cette thèse.

1.3.2 La taille des sédiments

Les études de terrains ont permis de mettre en évidence une forte corrélation entre la taille des sédiments composant les cônes alluviaux et la pente de ceux-ci. Ces études montrent que plus les sédiments sont grossiers, plus la pente du cône est forte (Blissenbach, 1952; Bluck, 1964; Denny, 1965; Rice, 1999, Fig. 1.6). Cependant, sur le terrain, plusieurs facteurs peuvent agir

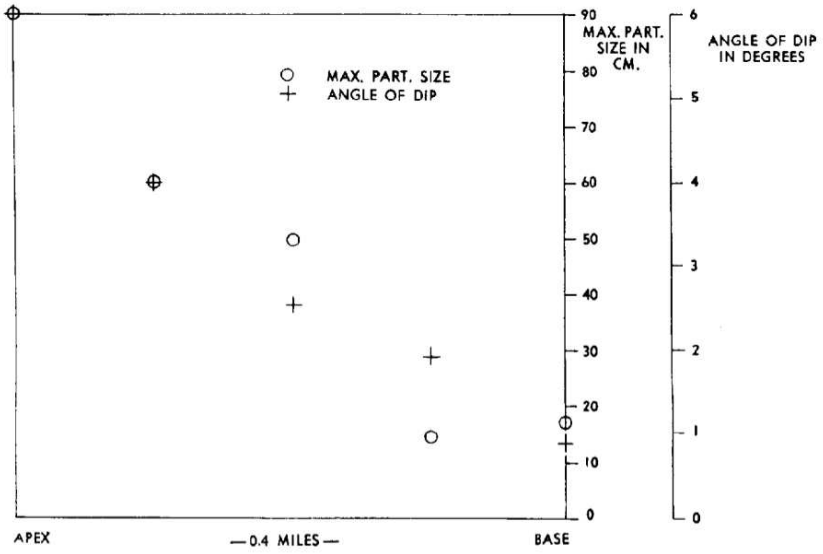

FIGURE 1.6 : Relation entre la taille des sédiments et la pente d'un cône alluvial, Aubrey Cliffs, Arizona. En ordonnée, taille des sédiments et pente locale, en abscisse distance par rapport à l'apex du cône. *D'après Blissenbach (1952).*

simultanément sur la pente (Stock et al., 2008). Il est donc difficile d'isoler l'influence de la taille des grains. Les modèles expérimentaux ont toutefois permis de lever cette ambiguïté et confirment les observations de terrain (Hooke, 1968; Le Hooke and Rohrer, 1979; Ikeda and Iseya, 1988). Pour comprendre cette dépendance, il est nécessaire de s'intéresser au seuil de mise en mouvement des grains. Ce seuil de mise en mouvement correspond à un équilibre entre la

force de friction exercée par le fluide sur le grain (qui dépend de la pente) et la force de gravité (Shields, 1936). À conditions identiques, pour qu'un gros grain soit mis en mouvement, la force de friction nécessaire doit être plus importante que pour un petit grain. On comprend donc, intuitivement, que la pente associée à la mise en mouvement d'un gros grain est plus importante que celle d'une rivière transportant des petits grains (Ikeda and Iseya, 1988).

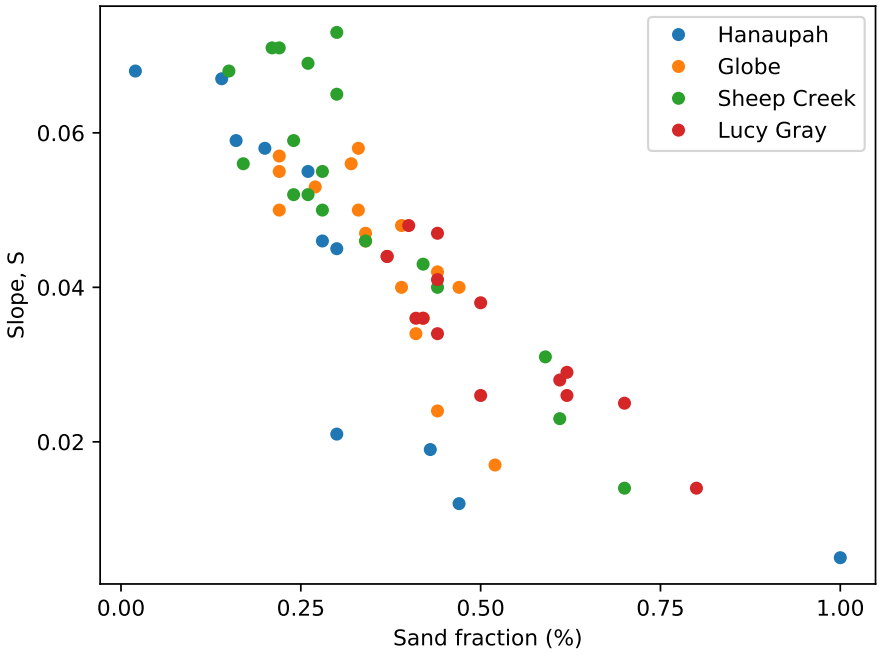

FIGURE 1.7 : Relation entre la fraction de sable et la pente de cônes. *Données issues de Stock et al. (2008).*

Dans la plupart des rivières naturelles, la taille des sédiments diminue vers l'aval, ce phénomène, appelé *downstream fining*, résulte soit de l'abrasion mécanique des grains au cours de leurs transport, soit d'un dépôt différentiel (Paola et al., 1992b; Smith and Ferguson, 1996; Fedele and Paola, 2007; Singer, 2008; Blom et al., 2016). La pente d'un cône étant corrélée à la taille des grains transportés par la rivière, une conséquence direct du *downstream fining* est la formation d'un profil radial concave. En utilisant les données de Stock et al. (2008), on peut montrer que sur les cônes alluviaux, il existe une forte corrélation entre la proportion de sédiment fins qui composent le lit de la rivière et la pente locale. La pente des cônes diminue vers l'aval quand la proportion de grains grossiers diminue (Fig. 1.7).

La présence de plusieurs tailles de grains dans les sédiments naturels soulève le problème du transport de sédiments polydisperses. Les mécanismes de transport de sédiment s'appliquant à un mélange de sédiment de plusieurs tailles sont encore mal compris (Meyer-Peter and Müller, 1948; Wilcock and Crowe, 2003; Houssais and Lajeunesse, 2012). Par conséquent, les lois de transport utilisées à l'heure actuelle sont souvent simplifiées : on ne prend en compte, par exemple, qu'une taille de sédiment (Parker, 1978a; Parker et al., 1998a; Nicholas and Quine, 2007).

Lorsque les cônes sont composés de deux types de sédiment, de mobilité distincte (gravier et sable par exemple), il a été observé expérimentalement et sur le terrain que les sédiments sont ségrégés en fonction de leur mobilité.

1.3.3 Les flux

Influence du flux de sédiment sur la dynamique des cônes alluviaux

Les cônes alluviaux résultent du dépôt de sédiments transportés par une rivière, la quantité de sédiment qui émerge à leur apex contrôle leur vitesse de croissance (Reitz and Jerolmack, 2012; Powell et al., 2012). Au premier ordre, si l'on considère un cône alluvial comme un demi-cône de pente constante, son volume est

$$V = \frac{\pi S R^3}{6}, \tag{1.2}$$

pour un cône d'angle d'ouverture π, de pente S et de rayon R (Fig. 1.1). En considérant que tous les sédiments sont piégés dans le cône, son volume est lié au flux de sédiment par la relation suivante,

$$V = \frac{Q_s t}{1-\lambda}, \tag{1.3}$$

où t est le temps de construction du cône et λ la porosité des dépôts. En utilisant les équations (1.2) et (1.3), on trouve que le rayon du cône croît proportionnellement à $(Q_s t)^{1/3}$. Ainsi, plus le flux de sédiment est important plus le cône grandit vite.

Le flux de sédiment contrôle aussi la dynamique interne des cônes. Des études de terrains montrent, par exemple, que la fréquence d'avulsion d'une rivière est dépendante du flux de sédiment (Sinha, 1998; Assine, 2005). Plus le flux de sédiment est important, plus le chenal se comble rapidement, entraînant une avulsion. Cette dépendance a été confirmée et quantifiée expérimentalement (Bryant et al., 1995; Ashworth et al., 2004; Reitz et al., 2010).

Influence des flux sur la morphologie des cônes alluviaux

En plus de contrôler la dynamique de croissance des cônes alluviaux, les flux d'eau et de sédiment ont aussi une influence sur leur morphologie, notamment sur leur pente.

Le flux d'eau : Le flux d'eau, Q_w, est difficile à mesurer sur le terrain. En effet, les chenaux sont souvent éphémères et les mesures effectuées de façon épisodique lors de mission de terrain (Stock et al., 2008; Gaurav et al., 2015; Métivier et al., 2016). Pour suppléer ce manque d'information, l'aire du bassin versant alimentant le cône est souvent utilisée comme substitut pour le débit d'eau. En utilisant ce proxy, les observations de terrain montrent que la pente des cônes alluviaux diminue lorsque l'aire drainée (*i.e.* le débit d'eau) augmente (Drew, 1873; Denny, 1965; Saito and Oguchi, 2005; Blair and McPherson, 2009, Fig. 1.8). Cette observation est confirmée par les modèles numériques et expérimentaux de Densmore et al. (2007) et Rohais et al. (2012) qui mettent en évidence une diminution de la pente des cônes lorsque l'intensité des précipitations augmente.

Le flux de sédiment : La mesure de flux de sédiment, Q_s, sur le terrain s'avère être encore plus compliquée. En effet, la rivière transporte des sédiments principalement en période de crue ce qui rend les mesures particulièrement difficiles et dangereuses. De plus, à l'heure actuelle, la mesure du flux de sédiment s'effectue par échantillonnage ponctuel, ce qui ne permet d'avoir qu'une estimation locale du flux de sédiment (Meunier et al., 2006; Liu et al., 2008). Dans les cônes

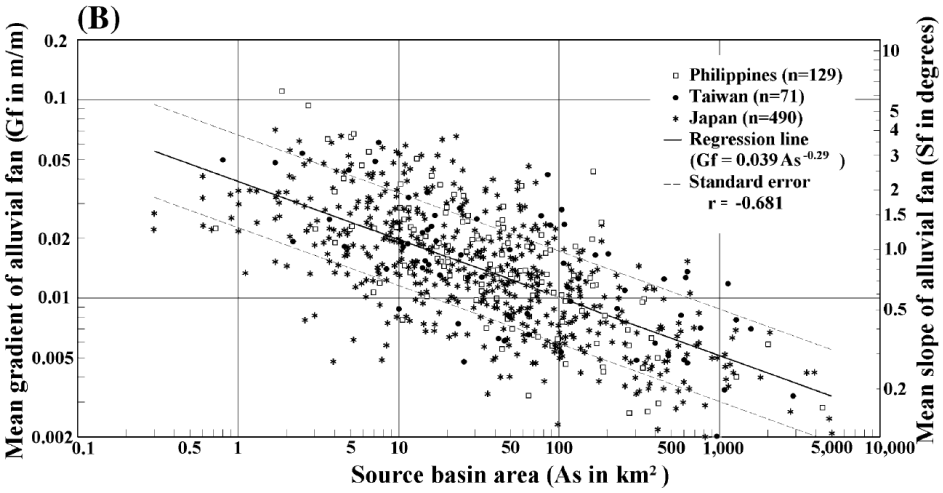

FIGURE 1.8 : Relation entre la pente du cône et l'aire du bassin versant (utilisée comme proxy pour le débit d'eau). *D'après Saito and Oguchi (2005).*

alluviaux, les sédiments se déposent tout au long de la rivière. Le flux de sédiment diminue donc vers l'aval. En utilisant une loi de transport empirique déterminée expérimentalement par Ikeda and Iseya (1988), Stock et al. (2008) ont montré qu'il existe une corrélation entre la diminution du flux de sédiment en aval et celle de la pente des cônes. Cette diminution de la pente des cônes en aval a donc pour conséquence de générer un profil en long concave. Ces observations sont confirmées par des modèles expérimentaux dans lesquels une augmentation du flux de sédiment entraîne une augmentation de la pente (Whipple et al., 1998; Ashworth et al., 2007). Cette augmentation de la pente n'est cependant pas linéaire. Il est nécessaire de bien comprendre les lois de transport qui contrôlent la mise en mouvement des sédiments pour pouvoir quantifier l'influence de ce flux sur la pente des cônes (Guerit et al., 2014).

Le rapport des flux Q_s/Q_w : D'un point de vue expérimental, l'influence des flux d'eau et de sédiment sur la géométrie des cônes est souvent exprimée en terme de rapport de ces flux, Q_s/Q_w. La pente des cônes augmente quand le rapport des flux augmente (Le Hooke and Rohrer, 1979; Paola et al., 1992a; Whipple et al., 1998; Clarke et al., 2010; Powell et al., 2012). Cette dépendance de la pente au rapport des flux a été initialement proposée par Parker et al. (1998a). Les auteurs s'appuient sur l'équation de conservation de la masse et trois relations internes qui décrivent l'écoulement et le transport de sédiment :

- la résistance du fluide, en utilisant une relation de Chézy (Paola et al., 1999),
- une loi de transport des sédiments (Meyer-Peter and Müller, 1948),
- la largeur sur laquelle les sédiments sont transportés (B_{ac}), définie comme une portion du cône,

$$B_{ac} = \chi \Theta r, \tag{1.4}$$

avec χ une fraction allant de 0 à 1 (lorsque $\chi = 1$, l'écoulement est en nappe sur toute la surface du cône), Θ l'angle d'ouverture du cône, et r son rayon. Cette définition implique

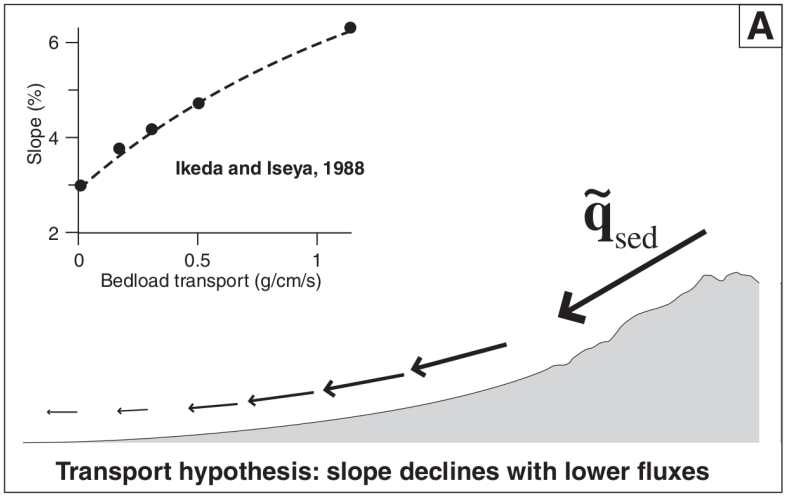

FIGURE 1.9 : Modèle conceptuel de l'influence du flux de sédiment sur la pente des cônes alluviaux. Hypothèse de Drew (1873) : la diminution du flux de sédiment Q_s (illustrée par les flèches) en aval provoque une diminution de la pente. Le graphique modifié de Ikeda and Iseya (1988) illustre cet effet dans un chenal, les pentes obtenues sont approximativement celles atteintes par les cône alluviaux. *D'après Stock et al. (2008).*

que la rivière s'élargisse vers l'aval (Parker et al., 1998a).

En utilisant ces trois relations, les auteurs suggèrent qu'il existe une fonction f telle que,

$$S = f\left(\frac{Q_s}{Q_w}\right) \tag{1.5}$$

Cette relation implique que lorsque le flux de sédiment devient nul, la pente du cône est nulle. Ce qui n'est pas compatible avec l'existence d'une pente au seuil. En effet, les expériences de Seizilles et al. (2013) ont montrées que lorsqu'une rivière ne transporte pas de sédiment sa pente n'est pas nulle. Elle est contrôlée par le débit d'eau et le seuil de mise en mouvement des sédiments (Section. 2.1).

De plus, lorsque l'on représente la pente en fonction du rapport des flux de différentes études, on observe qu'il n'existe pas de relation universelle entre ces deux paramètres (Fig. 1.10). Pour chaque jeu de données, on voit apparaître une tendance permettant de relier l'évolution de la pente au rapport des flux, mais aucune loi ne permet de satisfaire les données des différentes expériences. Notamment, si l'on se concentre sur les données de Clarke et al. (2008), on observe que pour un même rapport de flux, la pente n'est pas constante. La pente est d'autant plus faible que les flux absolus sont fort, ce qui suggère une prédominance de l'influence du flux d'eau par rapport au flux de sédiment.

Enfin, le modèle de Parker et al. (1998a) considère que la largeur du chenal est une portion du cône. Au contraire, plusieurs études montrent que la largeur des rivières alluviales s'ajuste au flux d'eau et de sédiment (Glover and Florey, 1951; Henderson, 1961; Parker, 1978a,b; Seizilles et al., 2013). Il est donc nécessaire de contraindre la largeur de la rivière pour estimer le flux de sédiment à la surface des cônes.

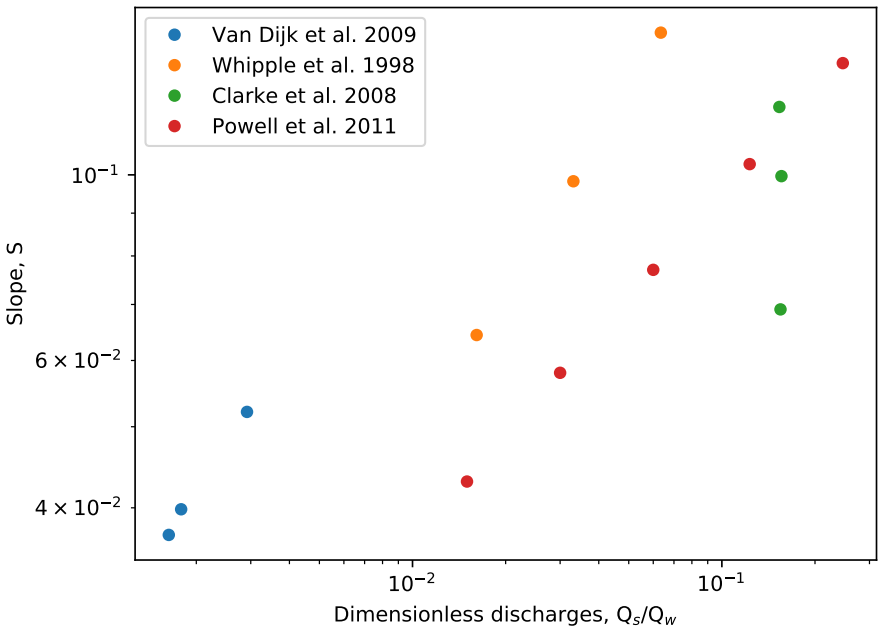

FIGURE 1.10 : Pente du cône en fonction du rapport des flux. *Modifié d'après Van Dijk et al. (2009).*

Dans cette section, nous avons montré que la pente des cônes alluviaux est liée aux paramètres d'entrée (d_s, Q_w et Q_s). La pente des cônes alluviaux augmente avec la taille des grains ainsi que le débit de sédiment. Au contraire, elle diminue avec l'augmentation du débit d'eau. Cependant, l'influence de ces trois paramètres n'est généralement pas quantifiée indépendamment. Pourtant, l'étude des résultats de Clarke et al. (2010), suggère que l'influence du débit d'eau et de sédiment doit être considérée individuellement et non pas sous forme de rapport.

1.3.4 Influence respective des paramètres d'entrée sur la pente du cône

C'est précisément dans le but d'isoler l'influence des différents paramètres d'entrée (d_s, Q_w et Q_s) sur la pente du cône que Guerit et al. (2014) ont mis en place une expérience formant un cône alluvial confiné dans un plan vertical. Dans cette expérience, pour s'affranchir du problème de la largeur de la rivière, le dépôt se construit entre deux plaques de Plexiglass distantes de 2.5 cm. La largeur de l'écoulement est ainsi bien contrainte. De plus, pour éviter les relations empiriques imposées par la nature turbulente de l'écoulement, le fluide utilisé est un mélange visqueux d'eau et de glycérol de masse volumique $\rho = 1210\ \mathrm{kg\,m^{-3}}$ et de viscosité $\eta = 40$ mPa s. Ce fluide permet de générer un écoulement laminaire caractérisé par un nombre de Reynolds $Re \approx 10$. Finalement, pour simplifier la mesure de la loi de transport, les grains utilisés sont mono-disperse. Il s'agit de billes de verre de diamètre $d_s = 477\ \mu$m et de densité $\rho_s = 2485\ \mathrm{kg\,m^{-3}}$ (Fig. 1.11).

Pour étudier l'influence des différents paramètres toutes les expériences ont été réalisées avec les mêmes grains tout en faisant varier indépendamment les débits de fluide et de sédiment. Lorsque le flux de sédiment qui alimente le cône est très faible, la pente du cône est contrôlée par le seuil de mise en mouvement des sédiments. Ainsi, Guerit et al. (2014) montrent que lorsque

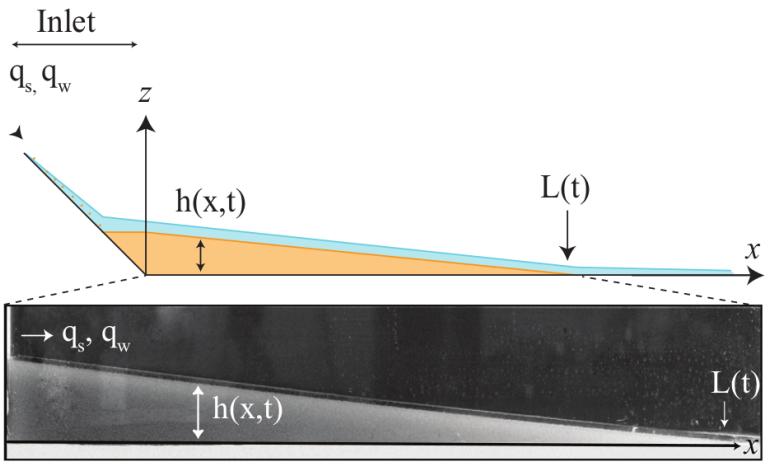

FIGURE 1.11 : Dispositif expérimental et définition des variables ; q_s et q_w les flux par unité de surface de sédiment et d'eau, $h(x,t)$ la hauteur du cône, et $L(t)$ la longueur maximum du cône. *D'après Guerit et al. (2014).*

le flux de sédiment tend vers zéro, la pente du cône tend vers une valeur seuil qui est contrôlée, au premier ordre, par la taille des sédiments d_s et qui varie en proportion de $1/\sqrt{Q_w}$. Dans ces conditions, le flux de sédiment contrôle uniquement la vitesse de croissance du cône. Lorsque le flux de sédiment augmente, le profil du cône est modifié. Les sédiments déposés le long du cône ajoutent une déviation quadratique au profil linéaire de celui-ci. Cette déviation est alors proportionnelle à q_s.

Cette étude met ainsi en évidence une hiérarchie entre les différents paramètres qui contrôlent la pente du dépôt. En effet, lorsque le flux de sédiment est faible, celui-ci peut être négligé, au premier ordre, et la pente du cône est contrôlée par la taille des sédiments et le débit d'eau. Par contre, plus le flux de sédiment augmente, plus la pente s'éloigne de sa valeur seuil. Les sédiments étant déposés le long du cône, cet écart au seuil se caractérise par la formation d'un profil concave. La forme de ce profil est interprétée comme la signature du transport sédimentaire. Pour aller plus loin, il serait cependant nécessaire de tester cette théorie sur un cône complet.

Les observations présentées dans ce chapitre nous permettent de définir le cadre dans lequel s'incrit notre étude, cela nous amène donc à présenter les objectifs de cette thèse.

1.4 Objectifs de la thèse

Pour comprendre l'évolution des surfaces terrestres, il est nécessaire de reconstituer les mouvement de masse à la surface de la Terre. De par leur position à l'interface entre les zones d'érosion et les zones de dépôts, les cônes alluviaux apparaissent comme un témoin primordial des transferts de masse à la sortie des reliefs continentaux. Les reconstitutions de paléo-flux sédimentaire se font, à l'heure actuelle, par reconstruction de volume. Cette technique permet d'estimer l'ordre de grandeur des flux ayant construits les cônes, cependant la période d'activité du cône, nécessaire à cette estimation, est source d'incertitude. Grâce aux observations de terrain et à l'utilisation de modèles expérimentaux les études antérieures ont montrées que la pente des

cônes alluviaux est contrôlée par les flux d'eau et de sédiment et la taille des sédiments. L'idée est donc de reconstituer les paléo-flux à partir de la pente des cônes alluviaux. Pour résoudre ce problème inverse il est indispensable de quantifier l'influence des flux d'eau et de sédiment et de la taille des grains sur la pente du cône.

Comme nous l'avons vu, la pente du cône est généralement exprimée en fonction du rapport des flux (Parker et al., 1998a; Whipple et al., 1998). Cette relation rend compte de l'augmentation de la pente du cône avec le débit de sédiment et de sa diminution avec le débit d'eau. Cependant, cette relation ne permet pas l'existence d'une pente seuil, atteinte lorsque le flux de sédiment devient nul (Seizilles et al., 2013). Il est donc nécessaire de découpler les effets des débits d'eau et de sédiment pour comprendre leur influence respective sur la pente des cônes.

Concernant l'influence de la taille des grains sur la morphologie des cônes alluviaux, l'augmentation de la pente des cônes alluviaux avec la taille des grains est bien documentée, que ce soit dans le milieux naturel ou expérimentalement (Blissenbach, 1952; Ikeda and Iseya, 1988). Lorsqu'un cône est composé de plusieurs tailles de grains, les observations de terrain et expérimentales montrent qu'un mécanisme de ségrégation permet de séparer les sédiments grossiers des sédiments fins (Reitz and Jerolmack, 2012; Miller et al., 2014). La position de ce front de ségrégation dépend des paramètres d'entrée (Q_s, Q_w et d_s), ainsi que de la proportion de sédiment fin et grossier (Paola et al., 1992a). Pour reconstruire ces paramètres d'entrée, il serait intéressant d'étudier la géométrie des cônes composés de plusieurs tailles de grain.

Afin de quantifier l'influence de ces paramètres d'entrée sur la morphologie des cônes alluviaux, nous avons choisi d'utiliser la modélisation expérimentale. Nous avons donc conçu deux dispositifs expérimentaux permettant de construire des cônes alluviaux dans des conditions contrôlées. Les expériences sont réalisées en ne faisant varier qu'un seul des paramètres à la fois. Nous avons réalisé trois jeux d'expériences pour répondre aux questions suivantes :

- Existe-t-il une pente seuil, dépendant uniquement des sédiments transportés et du débit d'eau, atteinte lorsque le flux de sédiment, alimentant le cône, est très faible ?
- Comment la géométrie des cônes est-elle modifiée lorsque les sédiments les composant ne sont pas uniformes ?
- Peut-on reconstruire le flux de sédiment à partir de la pente des cônes alluviaux ?

Pour répondre à ces questions, il est important de comprendre les mécanismes physiques, agissant aux différentes échelles, qui contribuent à la formation des cônes alluviaux. En effet, les cônes alluviaux sont formés par des rivières, qui établissent spontanément leur lit sous l'effet du transport sédimentaire. Le flux de sédiment à la surface du cône dépend donc du flux de sédiment dans la rivière qui le construit.

Pour comprendre la formation d'un cône alluvial, nous devons donc identifier les propriétés transmises d'une échelle à l'autre, depuis le mouvement d'un grain sédimentaire jusqu'au dépôt alluvial, en passant par la rivière. Pour chacune des expériences réalisées, nous nous sommes attachés à caractériser les mécanismes agissant depuis l'échelle du mouvement du grain sédimentaire, en passant par l'échelle de la rivière pour enfin aboutir à la formation du cône. La figure (1.12), représente ces différentes échelles.

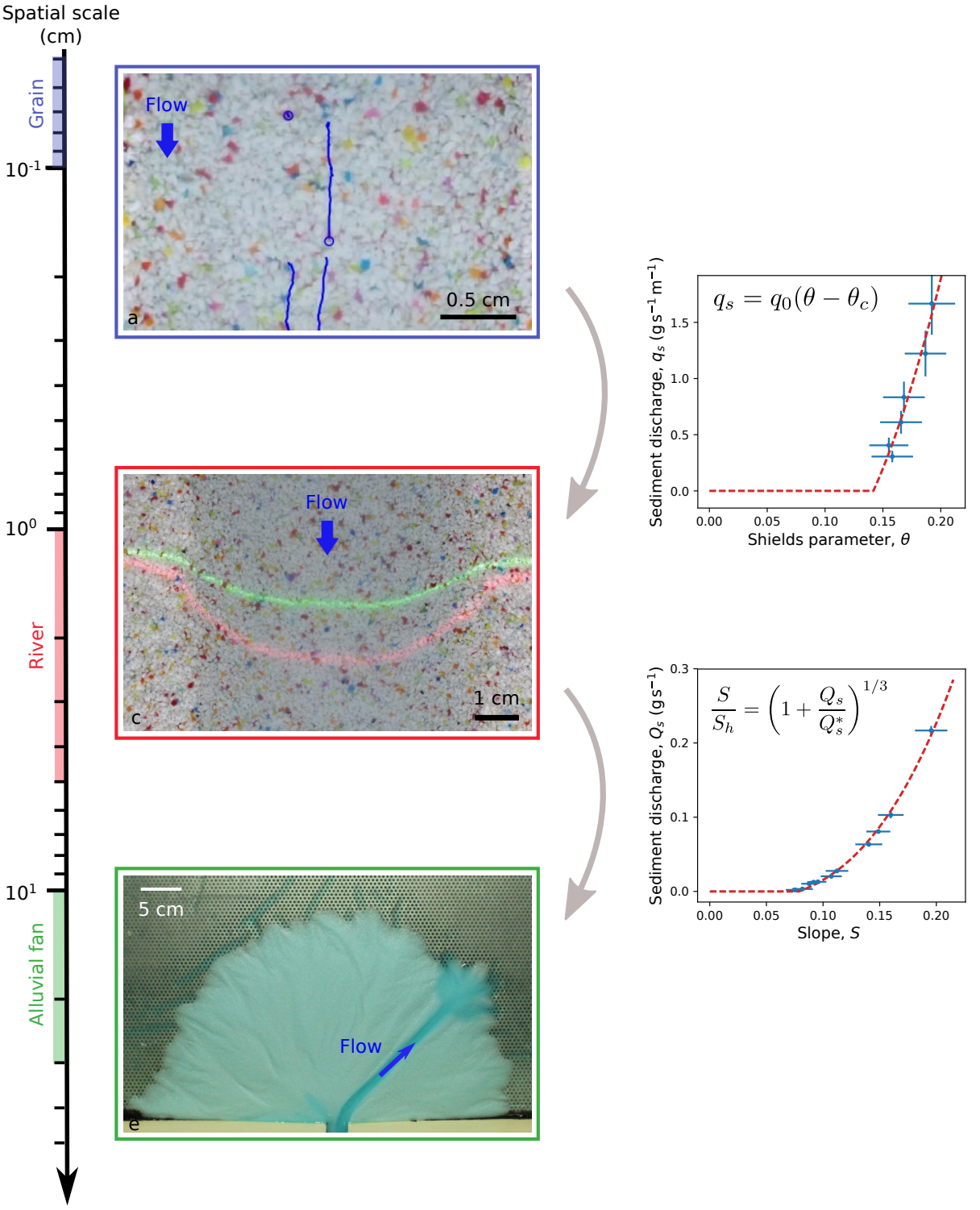

FIGURE 1.12 : Expériences utilisées pour caractériser les mécanismes physiques, agissant à différentes échelles, qui permettent de comprendre la morphologie des cônes alluviaux. a) Suivi de la trajectoire des grains, les lignes bleues représentent la trajectoire d'un grain, *D'après Abramian et al. (prep)*. b) Caractérisation du seuil de mise en mouvement des sédiments, loi de transport à seuil à l'échelle du grain. c) Formation d'une rivière en laboratoire. Les lignes laser verte et rouge permettent de mesurer la morphologie de la rivière *D'après Seizilles et al. (2013) et Abramian et al. (prep)* . d) Influence du flux de sédiment sur la pente d'une rivière alluviale, loi de transport à seuil à l'échelle de la rivière. e) Formation d'un cône alluvial en laboratoire.

La plus petite échelle concerne la mise en mouvement d'un grain sous l'action d'un fluide (Appendice A). Pour comprendre les mécanisme agissant à cette échelle, nous utilisons l'expérience mise en place par Seizilles et al. (2014). Cette expérience utilise un chenal de 3.2 cm de large dans lequel s'écoule un fluide transportant une charge sédimentaire variable (Fig. 1.12a). Le but est de quantifier le seuil à partir duquel le grain est mis en mouvement. Ce seuil est caractérisé par le nombre de Shields critique, θ_c (Shields, 1936),

$$\theta_c = \frac{\tau_c}{(\rho_s - \rho) g d_s}, \tag{1.6}$$

avec τ_c le cisaillement critique du fluide, ρ_s et ρ la densité des sédiments et du fluide, d_s le diamètre des grains et g la constante gravitationnelle. En réalisant des expériences avec un débit sédimentaire variable, Seizilles et al. (2014) obtiennent une loi de transport à seuil, qui relie la valeur du flux de sédiment au nombre de Shields (Fig. 1.12b),

$$q_s = q_0(\theta - \theta_c), \tag{1.7}$$

où q_0 est un flux de sédiment caractéristique qui dépend des caractéristiques physiques du grain et du fluide. Un suivi de la trajectoire des grains, par analyse vidéo, montre que les grains se déplacent majoritairement dans la direction de l'écoulement, mais qu'il existe aussi une composante transverse de se déplacement (Seizilles et al., 2014). Les grains se comportent individuellement comme des marcheurs aléatoires, ce qui génère un flux diffusif transverse à la direction de l'écoulement. Ce flux de sédiment diffusif est caractérisé par une longueur de diffusion l_d.

En considérant la loi de transport (Eq. 1.7) et la longueur de diffusion déterminées expérimentalement, il est possible de passer à l'échelle supérieure et de s'intéresser au comportement d'une rivière transportant des sédiments (Section 4.1). Pour comprendre ce mécanisme, nous utilisons les expériences de Seizilles et al. (2013) et Abramian et al. (prep). Ces expériences consistent à faire s'écouler un fluide transportant, ou non, une charge sédimentaire sur un lit de sédiment et d'observer la forme de la rivière en résultant (Fig. 1.12c). Au bout d'un certain temps la rivière formée atteint une forme d'équilibre, qui est contrôlée par les paramètres d'entrée . Lorsque la rivière ne transporte pas de sédiment, sa morphologie (pente, largeur et profondeur) est contrôlée par le débit de fluide et la taille des sédiments. Cette morphologie correspond à une forme au seuil (Section 2.1). Lorsque l'on ajoute un flux de sédiment en entrée, le flux diffusif (observé à l'échelle du grain) apparaît. Celui-ci est compensé par un flux gravitaire due à la présence des berges, qui déplace les sédiments depuis les berges vers le centre du chenal. L'apparition de ces flux entraîne une modification de la forme de la rivière qui s'éloigne du seuil en suivant une loi de puissance (Fig. 1.12d). Par exemple, sa pente S s'écrit,

$$\frac{S}{S_h} = \left(1 + \frac{Q_s}{Q_s^*}\right)^{1/3}, \tag{1.8}$$

où S_h est la pente au seuil, Q_s le flux de sédiment imposé en entrée du système et Q_s^* un flux de sédiment caractéristique, qui dépend du préfacteur q_0 de la loi de transport ainsi que de la longueur de diffusion l_d.

Les cônes alluviaux sont construits par une rivière, qui parcourt toute leur surface au fil de

ses avulsions. Le cône alluvial hérite donc sa pente de la rivière qui le forme. Lors de la formation des cônes alluviaux les sédiments se déposent, le flux de sédiment diminue donc vers l'aval. La pente de la rivière alimentant le cône s'ajuste à cette diminution du flux de sédiment, générant un profil concave. Pour vérifier que la pente du cône suit l'évolution du flux de sédiment, nous étudions la pente d'un cône expérimental construit par une rivière (Fig. 1.12e).

Ces mécanismes et le passage d'une échelle à l'autre seront décrits plus en détail tout au long de ce manuscrit.

Chapter 2

Fan near the threshold of sediment motion

Dans le but d'étendre les résultats de Guerit et al. (2014) à un cône complet, nous avons conçu un dispositif expérimental qui permet de construire un cône avec un angle d'ouverture de 180°, alimenté par un chenal unique. De récentes études suggèrent que la forme d'une rivière, ne transportant pas de sédiments, est contrôlée par le seuil de mise en mouvement des sédiments (Seizilles et al., 2013). Dans ce cas, les caractéristiques géométriques de la rivière (pente, largeur et profondeur) sont décrites par des lois d'échelles, qui permettent de relier ces critères morphologiques à la taille des sédiments que transporte la rivière ainsi qu'à son débit (Glover and Florey, 1951; Henderson, 1961; Seizilles et al., 2013; Métivier et al., 2017). Dans le but d'appliquer cette théorie aux cônes alluviaux, nous construisons un cône alluvial avec un débit de sédiment très faible afin d'être dans les conditions les plus proche possibles du seuil de mise en mouvement des sédiments. Pour faciliter la compréhension des phénomènes physiques, nous utilisons un sédiment mono-disperse ainsi qu'un fluide visqueux. À l'aide de cette expérience nous mettons en évidence l'influence du débit fluide et de la taille des sédiments sur la morphologie du cône alluvial.

2.1 Alluvial river at the threshold of sediment motion

When a river flows on an alluvial bed, its geometry spontaneously evolves towards a stationary shape (Lacey, 1930). This equilibrium shape is controlled by the threshold of sediment motion (Glover and Florey, 1951; Henderson, 1961; Seizilles et al., 2013). When sediment grains are immersed in a river, two forces act on them: a normal force, induced by gravity and a tangential force induced by gravity and flow-induced stress τ (Fig. 2.1). When the river is at equilibrium, it is assumed that everywhere across the bed, sediments are at the threshold of motion (Eq. 2.1).

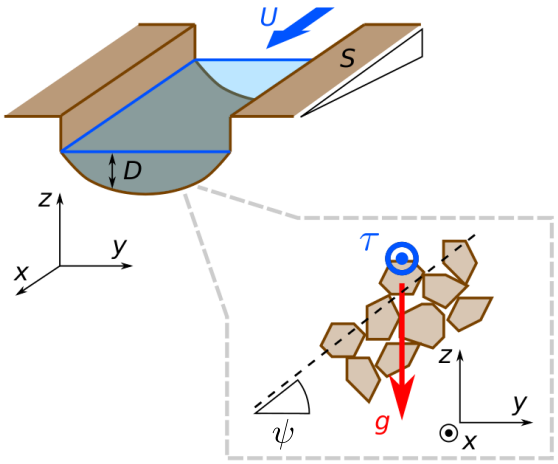

Figure 2.1: Schematic representation of a laboratory river. Both the depth D and the velocity U are functions of the transverse coordinate y. The river is invariant in the streamwise direction x. *From Seizilles et al. (2013).*

$$\left(\frac{\mu\,\tau}{\theta_c(\rho_s-\rho)gd_s}\right)^2+\sin^2\psi=\mu^2\cos^2\psi, \tag{2.1}$$

where μ is the friction coefficient, τ the flow-induced stress, θ_c the critical Shields parameter (Appendix A), ρ and ρ_s the fluid and sediment density, g the acceleration of gravity and ψ the bed-angle in the transverse direction. For a laminar flow, within the shallow-water approximation, the flow-induced stress reads,

$$\tau=\rho gDS, \tag{2.2}$$

where S is the longitudinal slope of the channel, and D its depth. The shallow-water approximation involves that $\cos\psi\approx 1$, Eqs. (2.1) and (2.2) together form a first-order differential equation:

$$\left(\frac{SD}{\mathcal{L}}\right)^2+\left(\frac{\partial D}{\partial y}\right)^2=\mu^2, \tag{2.3}$$

where $\mathcal{L}$ is a characteristic length which depends on sediment and fluid physical properties,

$$\mathcal{L}=\frac{\theta_c(\rho_s-\rho)d_s}{\mu\rho}. \tag{2.4}$$

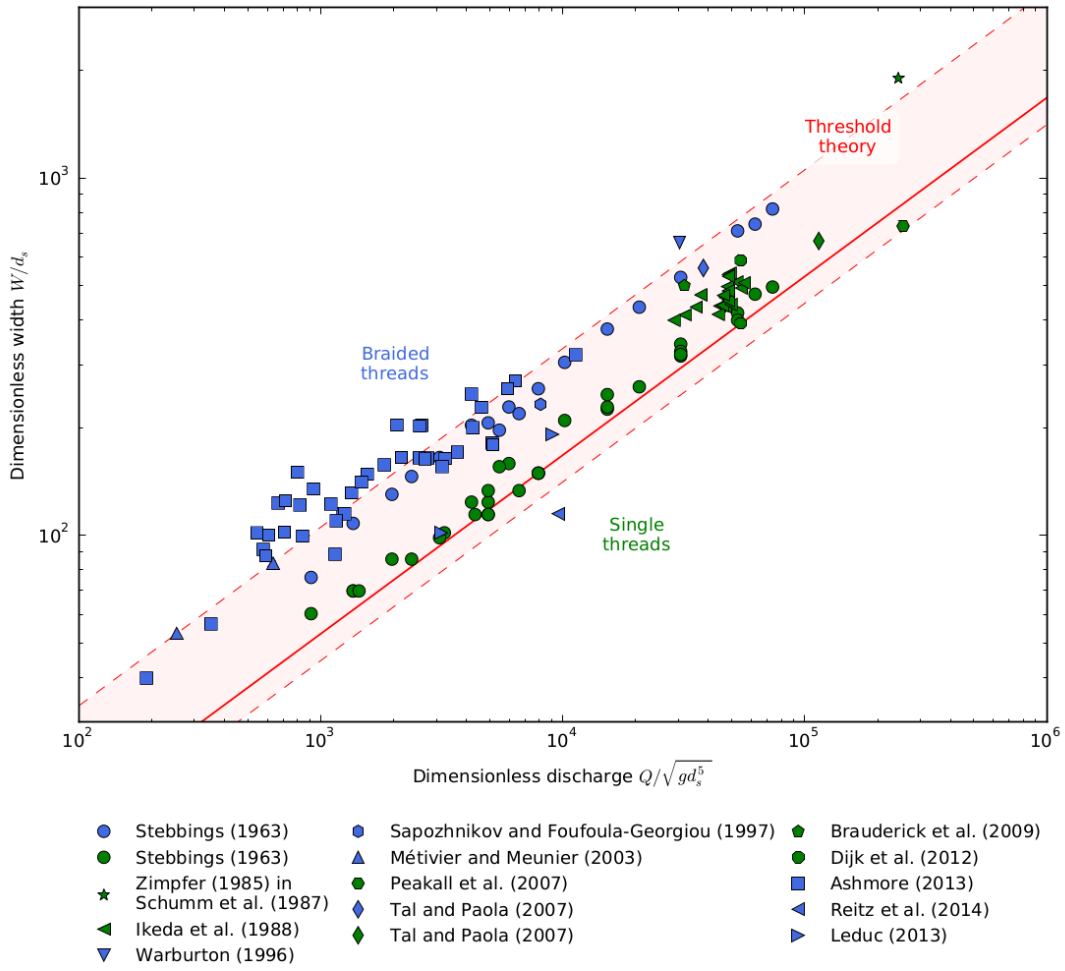

Figure 2.2: Lacey's law and threshold theory in laboratory experiments. Green: single-thread channels; blue: threads from braided rivers. Red line corresponds to the threshold theory. Shaded area and dashed lines indicate uncertainty about the parameters in experiments. *From Métivier et al. (2017).*

A solution of Eq. (2.3) gives the cosine cross-section of the channel,

$$D = \frac{\mu \mathcal{L}}{S} \cos\left(\frac{Sy}{\mathcal{L}}\right). \tag{2.5}$$

To go further, we need to consider the mass and momentum balance for the fluid,

$$Q_w = \int_{\text{channel}} UDdy. \tag{2.6}$$

Within the shallow-water approximation, the fluid friction at the bottom of the channel balances the gravity. As a consequence the momentum balance leads to Poiseuille velocity profile,

$$U = \frac{gSD^2}{3\nu}, \tag{2.7}$$

where ν is the fluid kinematic viscosity. Finally, by combining the shape of the cross-section (Eq. 2.5), the water mass balance (Eq. 2.6) and the momentum balance (Eq. 2.7), we obtain

two scaling laws linking a viscous river width, W_h, and slope, S_h, to the water discharge and sediment characteristics,

$$S_h = \mu \left(\frac{4g}{9\nu}\right)^{1/3} \left(\frac{\theta_c}{\mu}\frac{\rho_s - \rho}{\rho} d_s\right)^{4/3} \frac{1}{Q_w^{1/3}} \tag{2.8}$$

$$W_h = \frac{\pi}{\mu}\left(\frac{9\nu}{4g}\right)^{1/3} \left(\frac{\mu}{\theta_c}\frac{\rho}{(\rho_s - \rho)d_s}\right)^{1/3} Q_w^{1/3} \tag{2.9}$$

This threshold theory holds for laboratory and natural rivers in its turbulent version which reads,

$$W_H = \frac{\pi}{\mu^{3/4}}\left(\frac{\theta_c}{\mu}\ \frac{\rho_s - \rho}{\rho}\ d_s\right)^{-1/4} \sqrt{\frac{3}{2^{3/2}\,\mathcal{K}(1/2)}} \frac{\sqrt{Cf}}{g^{1/4}} \sqrt{Q_w}, \tag{2.10}$$

where $\mathcal{K}(1/2) \approx 1.85$ is the elliptic integral of the first kind, and C_f is Chézy's coefficient of fluid friction (Devauchelle et al., 2011; Gaurav et al., 2015; Métivier et al., 2017, Fig. 2.2).

Then, to compare the slope of our experimental fan to the one of an alluvial river at the threshold of sediment motion, we need to produce an experimental fan fed with a single channel and a low sediment discharge.

2.2 Experimental set-up

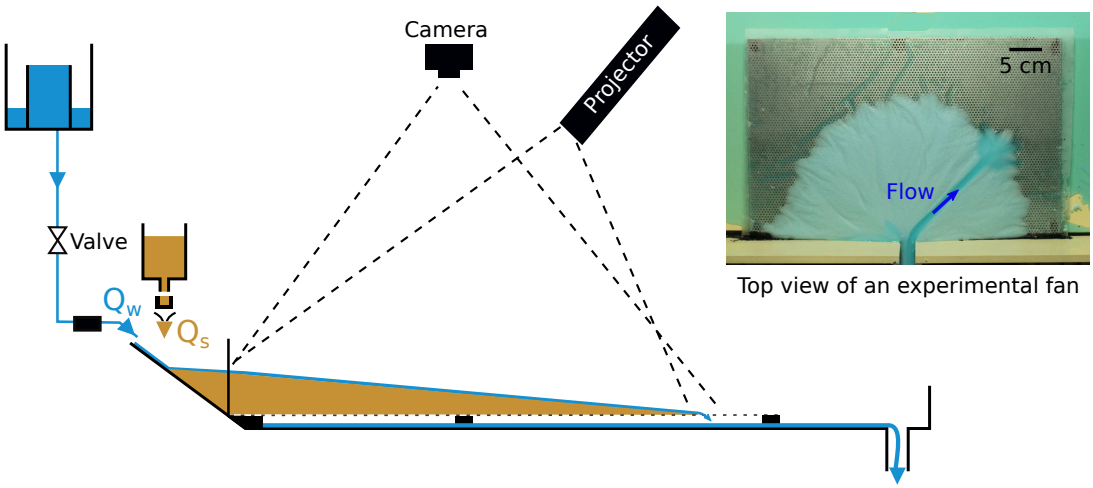

Figure 2.3: Schematic representation of the experimental set-up used.

We use a 80 cm-wide and 50 cm-long tank to produce our experimental fan. At the back of the tank a 15 cm-high vertical wall simulates the mountain front. In the center of this wall, a 2.5 cm-wide tilted channel directs sediment and fluid mixture toward the tank. The opposite side of the tank is bounded by a trench to evacuate fluid. To prevent fluid accumulation at the outlet of the fan, the fan is built on a 60 cm-wide and 30 cm-long shelf covered with a 200 μm sieve mesh. This facility allows us to build a fan with an opening angle of 180° (Fig. 2.3). The fluid discharge is kept constant using a header tank and we monitor its value using an electromagnetic flowmeter (Kobold, MIK-5NA10AE34R). A conveyor-belt supplies sediment into the channel,

this feeder-system is set on a scale (Ohaus, Explorer 35) to measure the sediment discharge. Every experimental measurement is automatically saved to a database (details of the experiment monitoring are presented in Appendix B).

To avoid empirical closing relations implied by turbulent flow, we use a viscous fluid which is a mixture of water (40 %) and glycerol (60 %). This fluid is characterized by a density $\rho = 1150\,\mathrm{kg\,m^{-3}}$ and an associated kinematic viscosity $\nu = 7\,10^{-6}\ \mathrm{m^2\,s}$. These physical properties are set by the composition of the mixture (Appendix B.2). To ensure constant fluid discharge we regularly measure the density of the fluid. We offset the water evaporation, surveyed through regular density measurement, by adding water to the mixture. The resulting flow is laminar with a Reynolds number of about 50. The fluid is mixed with a well-sorted uniform sediment composed of corundum grains with a median diameter $d_{50} = 415\ \mu$m and a density of $\rho_s = 3900\ \mathrm{kg\,m^{-3}}$ (Fig. 2.4a). The grain size is measured using image analysis and the density using a pycnometer. This sediment is also defined by a characteristic friction coefficient $\mu = 0.7$ and a critical Shields number $\theta_c = 0.14$ (Fig. 2.4b, measurement method is described in Appendix A).

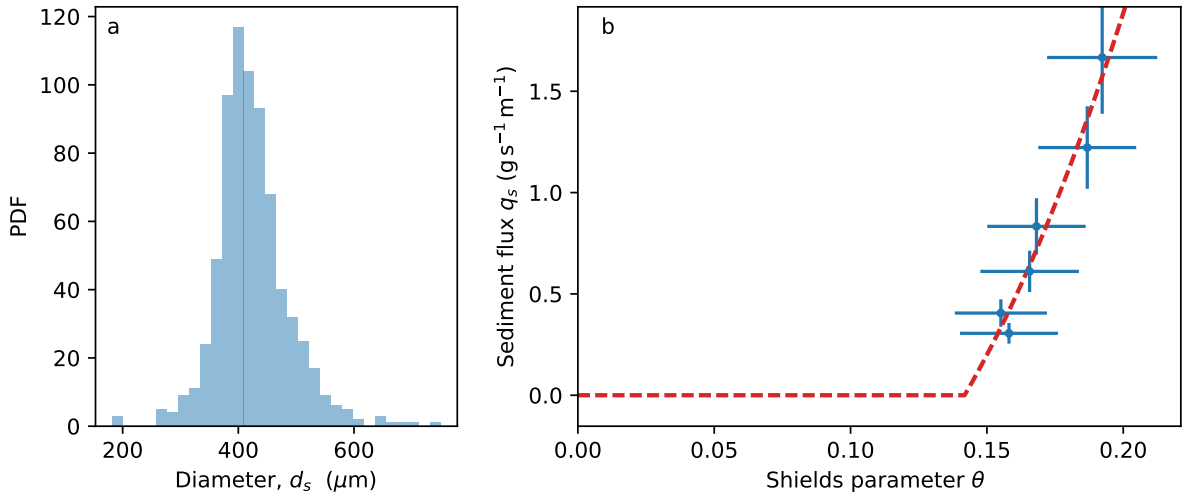

Figure 2.4: a) Probability density function of sediment diameter. b) Transport law $q_s = q_0(\theta - \theta_c)$, $q_0 = 162 \pm 5$ g s^{-1} m^{-1}, $\theta_c = 0.14 \pm 0.005$.

In order to remain near the threshold of sediment motion and quantify the influence of the fluid discharge on the fan slope, we perform six experiments. The sediment discharge, Q_s, remains fixed at a low value, whereas the fluid discharge, Q_w, varies between experiments (Table 2.1).

Table 2.1: Experimental parameters for the six runs.

Run	Fluid discharge Q_w ($\mathrm{L\,min^{-1}}$)	Sediment discharge Q_s ($\mathrm{g\,min^{-1}}$)
1	0.9 ± 0.01	0.2 ± 0.002
2	0.8 ± 0.01	0.2 ± 0.002
3	0.4 ± 0.01	0.2 ± 0.002
4	0.3 ± 0.01	0.2 ± 0.002
5	0.25 ± 0.01	0.2 ± 0.002
6	0.2 ± 0.01	0.2 ± 0.002

2.3 Fan growth

At the beginning of the experiment the surface of the experimental set-up is bare. We start the fluid and sediment feed at the same time and keep them constant during all the experiment. An axisymmetrical deposit spontaneously forms very rapidly. To monitor the fan evolution, we acquire top-view pictures using a camera (Canon EOS 100D with a lens: Canon 28-105 mm f/3.5-4.5 APO Macro 0.5m/1.6ft Ultrasonic) fixed above the tank center. We record an image every ten minutes (Fig. 2.5).

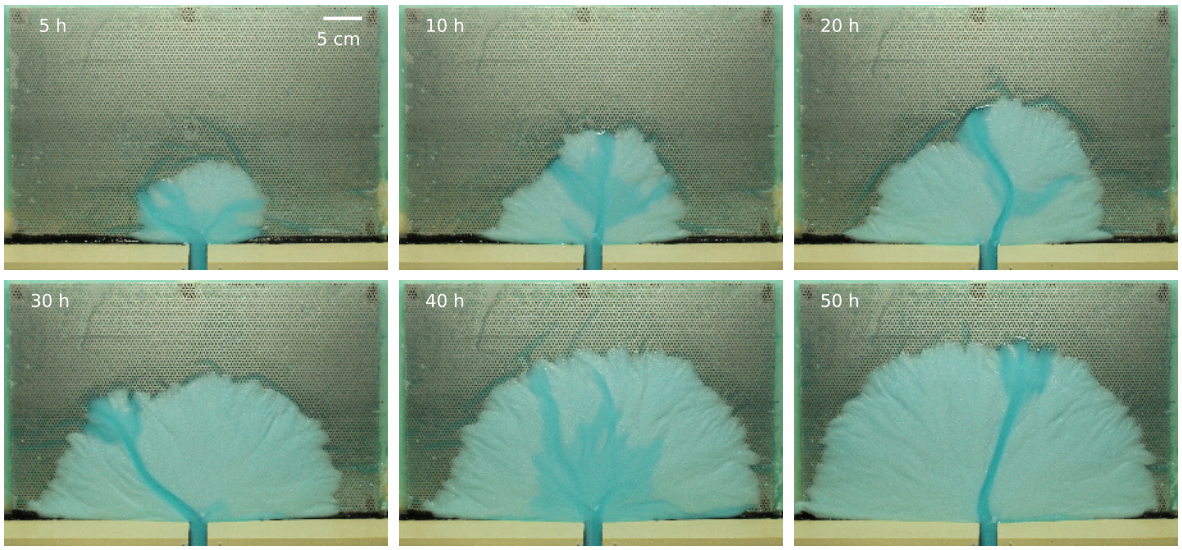

Figure 2.5: Top view pictures of the experimental fan at different time.

The growth of our fan is similar to the one of Van Dijk et al. (2009) and Reitz and Jerolmack (2012); the fan is built by alternating sheet flows and channelized flows. However, we observe that the period where sheet-flow dominates rarefies with time so that the fan becomes mostly fed by a single channel. This channel avulses with time and flows across all the fan surface maintaining its axisymmetry (Fig. 2.5). The mechanism of avulsion is driven by the sediment deposition and its frequency correlated to the sediment discharge (Bryant et al., 1995; Reitz and Jerolmack, 2012). Using high frequency pictures, we observe the filling of the channel, which leads to an avulsion (Fig. 2.6). The cycle starts with a straight channel with well-defined banks. Sediment

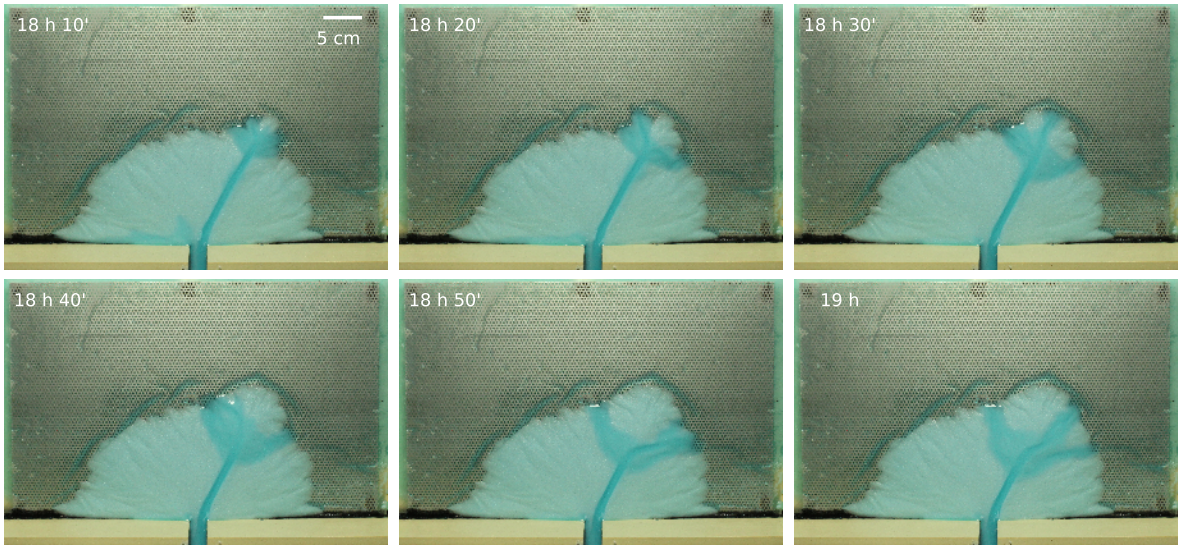

Figure 2.6: High frequency pictures, 10 min apart, channel filling from the distal to the proximal part.

deposition initiates at the downstream end of the channel and progressively propagates upwards. This deposition front pushes the flow to spill over the banks and carves a new channel. Sheet-flow occurs during the transient between flooding of the channels that fills and inception of the new channel.

Using the still image we acquired, we can measure the evolution of the fan radius. To do so, we develop an algorithm that automatically locates the fan toe (Appendix C.1). Because the fan color is well defined, we can detect its boundary by applying a threshold. Then we measure the average radius from the apex to the boundary. For this, we approximate the fan boundary by a semi-circle. The observed variability between the measured distance and this average radius is less than 5%. After a transient of about three hours, the fan radius evolves linearly with the cubic root of time (Fig. 2.7).

This evolution agrees with mass balance of the fan. As we assume our deposit is perfectly semi-conical, its volume V reads

$$V = \frac{\pi S R^3}{6}, \tag{2.11}$$

where R is the fan radius and the aperture angle equals π. Assuming that all the sediment injected is trapped into the fan, we find

$$V = \frac{Q_s\, t}{\rho_s(1-\lambda)}. \tag{2.12}$$

Using Eqs.(2.11) and (2.12), we recover the result of (Reitz and Jerolmack, 2012),

$$R = \left(\frac{6\, Q_s}{\rho_s(1-\lambda)\pi S}\right)^{1/3} t^{1/3}. \tag{2.13}$$

The growth rate of the fan depends primarily on the sediment discharge, the aperture angle of

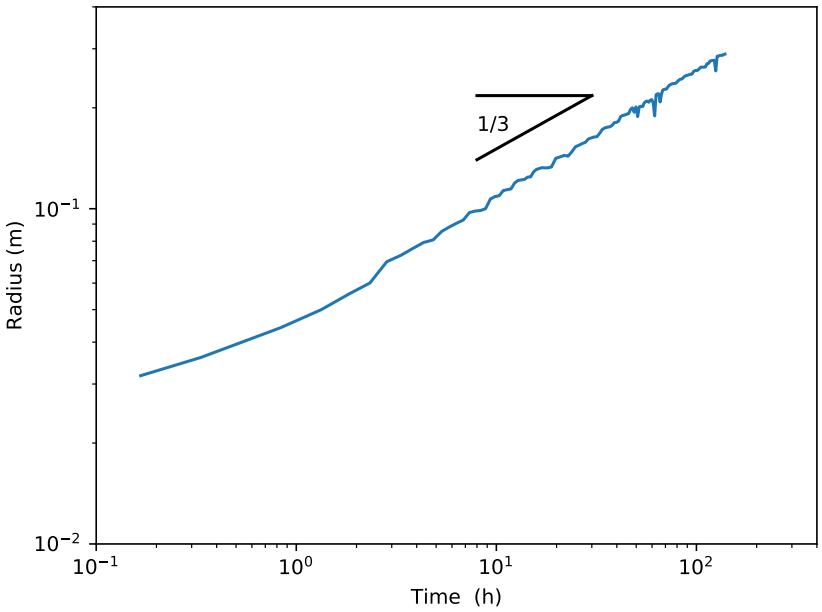

Figure 2.7: Evolution of the fan radius with time.

the fan and its slope.

Two parameters remain to be set in Eq. (2.13): the porosity of the deposit, λ, and its slope, S. To estimate these parameters, we use the digital elevation model (DEM) of our experimental fan. A DEM is acquired using the projection of a Moiré pattern (Limare et al., 2011, method is described in Appendix C.2).

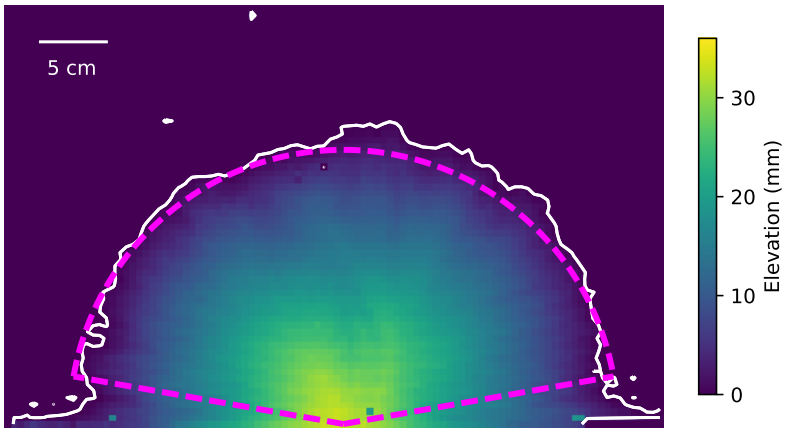

Figure 2.8: Topography acquisition. White dot: detection of the fan contours. Magenta dashed line: average radius

As a DEM gives the elevation of each pixel, we integrate the elevation of each pixel over the fan surface to calculate its volume. We then compare this value to the volume of sediment injected into the fan (Eq. 2.12). We measure the volume of our six experimental fans every hour, and we represent this volume as a function of the volume injected into the fan (Fig. 2.9). Both

volumes are linearly correlated. This then enables us to calculate the value of the porosity as the slope of the line that passes through the experimental points is equal to $1-\lambda$. With this method, we estimate the porosity of the deposit, $\lambda \approx 0.4$.

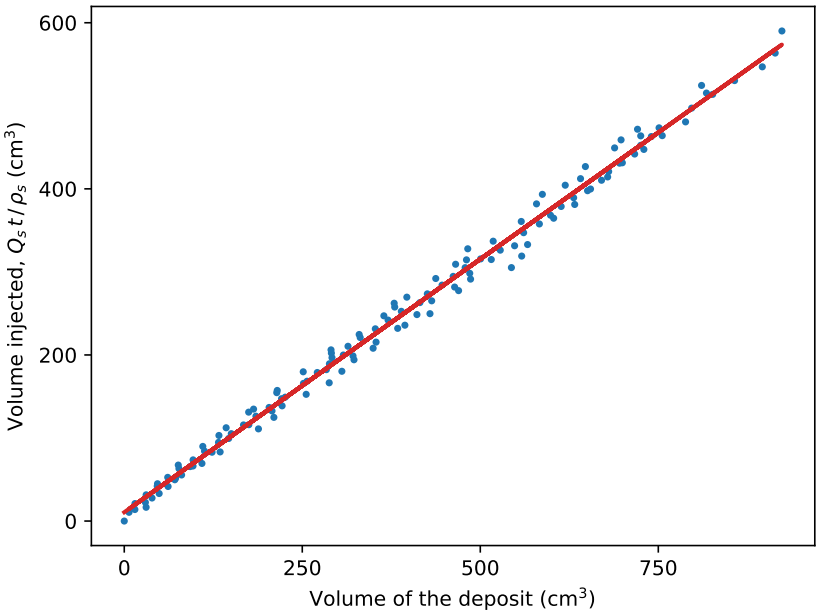

Figure 2.9: Volume of sediment injected into the experiment versus volume of the deposit. Red line: linear fit.

DEMs are also used to estimate the slope of our experimental fans. On each DEM, we first automatically locate the fan toe (white line in Fig. 2.8). We then approximate this boundary by a semi-circle (magenta dashed line in Fig. 2.8). Within this area, we measure the fan radial-profile along 34 radii, 5° apart from each other. The resulting profiles are similar to each other with a variability of less than 10% (Fig. 2.10a). Contrary to the observation of Van Dijk et al. (2009), we do not observe a significant variation of the slope between the centerline slope and the slope of the fan flanks (Fig. 2.10b). As a consequence, we assume that the fan is axisymmetric and that its slope is the same as the one of the river that feeds it.

To study the dynamics of the fan growth, we acquire DEMs every hour and plot the time-evolution of the spatially averaged profile (Fig. 2.11a). To the first order, the slope remains constant during the fan growth. This constant slope is reached after a transient of about 10 hours (Fig. 2.11b). At the beginning of the experiment, the slope is higher and then it reaches its equilibrium value. Once equilibrium is achieved, we still observe a small, within 5%, variability of the slope. One possible explanation for this variability, is the alternation of sheet flows and channelized flows (Van Dijk et al., 2009). When the flow is channelized, the local fluid discharge is higher consequently, the slope shallows. Hence, to the first order, the fan growth is self similar.

As a consequence, we conclude that an experimental fan fed with uniform sediment and constant fluid and sediment discharges is characterized by its slope only, and that this slope is spatially and temporally constant. Therefore, understanding the dynamics of a fan growth reduces to understanding what controls its slope.

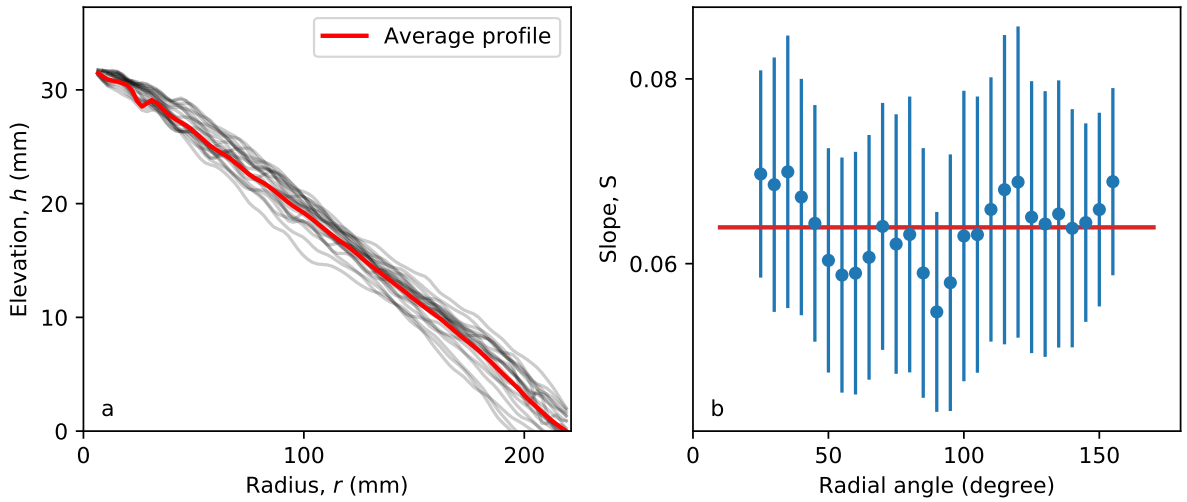

Figure 2.10: Variation of the fan slope at different angles. a) Fan profiles at different angles. Red line: average profile. b) Mean slope of the fan as a function of the angle. Red line: mean slope of the fan.

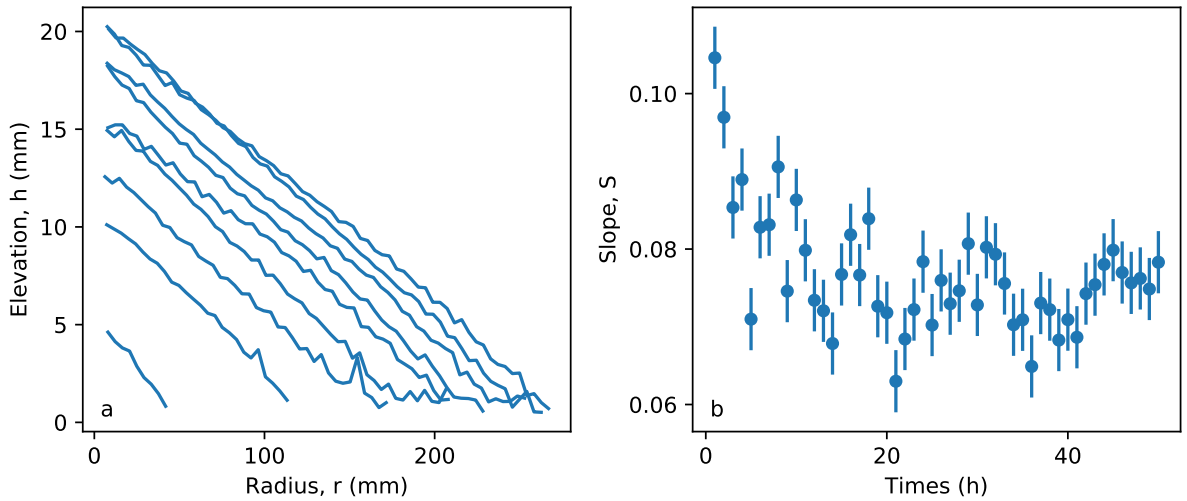

Figure 2.11: Evolution of the fan slope. a) Fan profile at different time. Six hours separate two consecutive lines. b) Slope of the fan as a function of time.

2.4 Threshold fan

To compare our experimental measurements to the threshold theory, we measure the slope of our experimental fan and the width of the river that feeds it. An experimental fan differs from an experimental river by the fact that it can not be formed without sediment deposition so that grains in the feeding channel are never exactly at the threshold of motion. Yet, we force the channel to remain close to the threshold of sediment motion by imposing a very low sediment discharge (0.2 g min^{-1}, approximately 25 grains per second). To verify that the river that built the fan is near the threshold of sediment motion, we first compare its width to the theoretical width of an alluvial river at equilibrium, W_h (Fig. 2.12). To do so, we manually locate, on top view pictures, the banks of the river. We measure the river width on 10 positions along its course and average them. We repeat the measurement each hour during the fan construction for our six experiments. The error bars in Fig. (2.12) represent the variability of the channel width over space and time. The red line is the theoretical width calculated using Eq. (2.9).

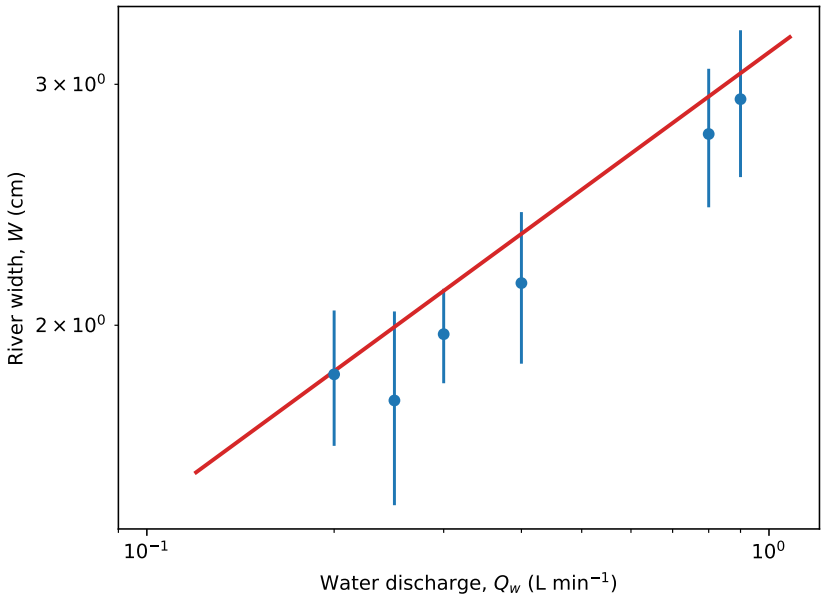

Figure 2.12: Width of the feeding channel as function of the water discharge, red line threoritical width Eq. (2.9).

As predicted by the equilibrium theory, the width of the channel scales as the water discharge to the power one third (Seizilles et al., 2013). Looking carefully, however, we note that the width of the channel is slightly smaller than the width of a threshold channel. This overestimation is about 10%, and it is of the same order as the width variability. Consequently, to the first order, we assume that the width of the river accords with the equilibrium theory.

Now, we focus on the fan slope. In the previous section (Section. 2.3) we demonstrated that the slope of the fan stays constant during its growth, and made the assumption that the slope of the fan is the one of the river that builds it. As a consequence, to compare the slope of the fan to the theoretical one (Eq. 2.8), we represent the space and time averaged slope as a function of the fluid discharge (Fig. 2.13). The red line is the slope we calculated using Eq. (2.8). We observe

that our experimental slopes follow the trend of the theory, they evolve with the fluid discharge power minus one third. Yet, the theory underestimate the slope by a factor of approximately two (red dashed line in Fig. 2.13). Seizilles de Mazancourt (2013) and Métivier et al. (2017) observe the same underestimation for experimental rivers (Seizilles de Mazancourt, 2013; Métivier et al., 2017).

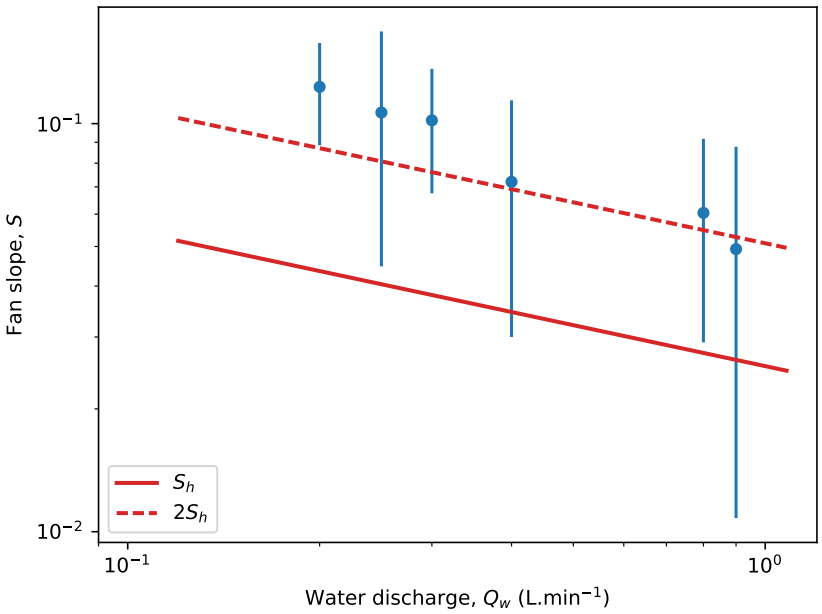

Figure 2.13: Slope of the fan as function of the water discharge, red line threshold slope, red dashed line = $2S_h$.

To understand the origin of this offset from the theory, we look at the scaling relationship between the slope and the water discharge,

$$S_h = \mu \left(\frac{4g}{9\nu}\right)^{1/3} \left(\frac{\theta_c}{\mu}\frac{\rho_s - \rho}{\rho} d_s\right)^{4/3} \frac{1}{Q_w^{1/3}}. \tag{2.14}$$

In this equation the values of the acceleration of gravity, g, the friction coefficient, μ, the sediment density and diameter, ρ_s and d_s, are well determined. The fluid characteristic, ρ and ν, are monitored during the run, and their variability is less than 5%. The fluid discharge Q_w, can be overestimated because we neglect the water infiltration, and because we consider that all the fluid injected in the experiment flows through one single channel. As mentioned earlier, the flow occurs sometimes in two channels, or as a sheet-flow. Because the fluid discharge influence on the slope is to the power one third, we would need to divide it by eight to resolve this underestimation. This seems unreasonable. The last parameter of Eq. (2.14), is the critical Shields number θ_c. Despite the fact that we carefully estimated this parameter using an independent and specific set-up (Appendix A), this measurement remains a matter of debate (Charru et al., 2004; Andreotti et al., 2012). In Eq. (2.14), the critical Shields number is raised at the power four over three, so an error on its measurement could have a high influence on the value of the threshold slope. The critical Shields number, θ_c, is also involved in the theoretical estimation of the river width at

the equilibrium but, in contrast to the slope, it is only raised at power one third (Eq. 2.9). As a consequence, an error on the measurement of the critical Shields parameter has a much smaller influence on the width than on the slope.

2.5 Conclusion

In this chapter we propose to use the theoretical framework developed for alluvial rivers to study the relation between the fan slope and the fluid discharge Q_w and grain size d_s (Seizilles et al., 2013). We generate six experimental alluvial fans fed with low sediment discharge in order to be as close as possible to the threshold of sediment motion. This procedure enables us to produce a fan mainly fed by a single-thread channel. This channel spontaneously avulses, to maintains the fan axisymmetry. For constant input parameters (Q_w, Q_s and d_s), the slope of our experimental fan also remains constant. We find that for a given sediment size, despite an uncertainty on the prefactor, the slope of the fan is controlled by the water discharge and scales with the water discharge to the power minus one third. The slope of the fan is controlled by the river that builds it. As a consequence, the aperture angle of the fan does not influence the fan slope. The aperture angle of the fan and the imposed sediment discharge control the growth rate of the fan.

In natural systems, however, alluvial fans are composed of a variety of sediments. Thus we can not transpose our results directly to natural fans. To go further we need to investigate the influence of a non-uniform sediment mixture, and to quantify the impact of the sediment discharge on the dynamics of fan growth. Reitz and Jerolmack (2012) and Miller et al. (2014) have shown that the formation of an alluvial fan fed with bimodal sediments leads to the formation of segregated and imbricated fans. The next chapter elaborates on these previous works, and explores the relation between the composition of the sediment mixture and the fan profile.

The result of Guerit et al. (2014) suggests that the sediment discharge causes a departure from threshold, in particular near the fan apex where the sediment discharge is the highest. In chapter 4, we extend this experimental set-up to quantify the influence of the sediment discharge on a complete fan.

Chapter 3

Bimodal laboratory fan

Dans ce chapitre, nous étudions l'influence d'une distribution bimodale de sédiment sur la morphologie du cône. Ces expériences ont été réalisées au *Saint Anthony Falls Laboratory (SAFL)*, Université du Minnesota à Minneapolis en collaboration avec Chris Paola et Vaughan Voller. Le but étant de mettre en évidence la relation, au premier ordre, entre les différents sédiments et la morphologie du cône, dans le cas stationnaire (débits d'eau et de sédiment constants). Ce chapitre est un article publié dans E-surf (Delorme et al., 2017).

Abstract

Using laboratory experiments, we investigate the growth of an alluvial fan fed with two distinct granular materials. Throughout the growth of the fan, its surface maintains a radial segregation, with the less mobile sediment concentrated near the apex. Scanning the fan surface with a laser, we find that the transition between the proximal and distal deposits coincides with a distinct slope break. A radial cross section reveals that the stratigraphy records the signal of this segregation. To interpret these observations, we conceptualize the fan as a radially symmetric structure that maintains its geometry as it grows. When combined with slope measurements, this model proves consistent with the sediment mass balance and successfully predicts the slope of the proximal-distal transition as preserved in the fan stratigraphy. While the threshold channel theory provides an order-of-magnitude estimate of the fan slopes, driven by the relatively high sediment discharge in our experimental system, the actual observed slopes are 3-5 times higher than those predicted by this theory.

3.1 Introduction

When a river leaves a mountain range to enter lowlands, it hits shallow slopes and loses valley confinement. This abrupt change causes it to deposit its sedimentary load into an alluvial fan (Bull, 1977; Rachocki and Church, 1990; Blair and McPherson, 1994; Harvey et al., 2005; Blair and McPherson, 2009). As the river builds this sedimentary structure, its bed rises above the surrounding land, and its channel becomes unstable. At this point, either the river erodes its banks to migrate laterally, or, during a large flood event, it overflows, and in a process referred to as "avulsion", establishes a new course for its channel (Field, 2001; Slingerland and Smith, 2004; Sinha, 2009). In both cases, the river constantly explores new paths to fill up hollows in the deposit surface and preserve its radial symmetry. The resulting deposit acquires the conical shape which characterizes alluvial fans.

As the first sedimentary archive along the river's course, an alluvial fan records the history of its catchment (Hinderer, 2012). Indeed, the geometrical reconstruction of a fan provides an estimate of its volume which, through mass balance, yields the average denudation rate of the catchment (Kiefer et al., 1997; Jayko, 2005; Jolivet et al., 2014; Guerit et al., 2016). Furthermore, when the river transports multiple grain sizes, it usually deposits the coarser sediment (gravel) near the fan apex, and the finer sediment (sand) at its toe. This segregation produces a gravel-sand transition front which moves forward and backward as the fan adjusts to external forcing. In radial cross section, this series of progradations and retrogradations appears as a boundary between lithostratigraphic units, a pattern often interpreted as the signature of tectonic or climatic events (Paola et al., 1992a; Clevis et al., 2003; Charreau et al., 2009; Whittaker et al., 2011; Dubille and Lavé, 2015).

To interpret the morphology and stratigraphy of an alluvial fan, we need to understand how it translates the input signal (e.g., water and sediment discharges) into its own geometry (e.g., its size, downstream slope and stratigraphy). For instance, Drew (1873) observed that the lower the water discharge Q_w, the steeper the fan slope. More recent observations point at the influence of the sediment discharges Q_s on the slope, often in the form of the ratio

Q_s/Q_w. In general, the slope steepens when this ratio increases (Parker et al., 1998a,b). At first sight, the shape of an alluvial fan is well approximated by a cone, but a closer look often reveals a steeper slope near the apex (Le Hooke and Rohrer, 1979; Blair, 1987a; Blair and McPherson, 2009; Miller et al., 2014). Possible explanations for this include the decrease in sediment discharge caused by deposition (transport hypothesis), or the downstream fining of the sediment (threshold hypothesis) (Blissenbach, 1952; Rice, 1999; Stock et al., 2008; Miller et al., 2014). In practice, the variations of grain-size, slope and sediment discharge along a fan are correlated. When the sediment is broadly distributed in size, these variations are smooth, whereas a bimodal distribution generates a segmented fan (Bull, 1964; Williams et al., 2006).

Only seldom do field measurements allow us to separate the various parameters affecting the morphology of a fan, making it difficult to isolate their respective influence. One way around this problem is to use laboratory experiments, where small alluvial fans can be easily produced under well-controlled conditions (Schumm et al., 1987; Parker, 1999; Paola et al., 2009; Clarke, 2015). When water and sediment are injected onto the bottom of a tank, a deposit spontaneously forms around its inlet. The formation of this deposit is remarkably similar to that of natural fans; in particular a network of migrating and avulsing channels distributes radially the sediment across the fan surface. As the forcing parameters vary, the deposit responds by adjusting its morphology. Muto and Steel (2004), for example, showed that a base level fall induces upstream channel entrenchment, terrace abandonment, and fan progradation.

The sediment discharge Q_s determines the growth rate of an experimental fan. Indeed, mass balance requires that the fan volume increase in proportion to the sediment input. Thus, as a consequence of the symmetry, the radius of the fan increases as $(Q_s t)^{1/3}$, where t is the time elapsed since the beginning of the experiment (Powell et al., 2012; Reitz and Jerolmack, 2012). Avulsions occur more frequently as the sediment discharge increases, showing that the internal dynamics of an experimental fan adjusts to the forcings (Bryant et al., 1995; Ashworth et al., 2004; Clarke et al., 2010; Reitz and Jerolmack, 2012). This adjustment allows the fan to maintain its conical shape which, at first order and for a single grain size, is characterized by its slope only.

Even in simplified experiments (constant inputs, single grain size), there is no clear consensus about the mechanism by which a fan selects its own slope. Most investigators observed that a low water discharge, a high sediment discharge, and coarse grains all contribute to a steeper fan (Le Hooke and Rohrer, 1979; Clarke et al., 2010). However, the respective influence of water and sediment discharges on the slope remains debated. Whipple et al. (1998), Van Dijk et al. (2009) and Powell et al. (2012) hypothesized that the slope is a function of the dimensionless ratio Q_s/Q_w. In contrast, Guerit et al. (2014) propose that all three parameters act independently. In their experiment, a fan composed of uniform sediment grows between two parallel plates that confine it to the vertical plane. They found that the flow maintains the deposit surface near the threshold of motion. As a result, a lower water discharge causes the fan to steepen. The sediment discharge perturbs the fan profile only moderately, by steepening the slope in proportion to its intensity. As the sediment is deposited along the fan, the slope returns to its threshold value as it approaches the toe; the associated curvature in this process being proportional to the sediment input.

Accordingly, the downstream curvature of an alluvial fan composed of uniform sediment can be interpreted as a signature of spatial variation in sediment transport. However, one can wonder what happens when the fan is composed of non-uniform sediment? When the grain size is broadly distributed, downstream fining can also affect the fan profile. This phenomenon occurs in flume experiments, where large grains concentrate near the inlet (Paola et al., 1992b; Smith and Ferguson, 1996). In the experiment of Reitz and Jerolmack (2012), the fan builds its upper part out of large grains, and deposits the smaller ones near its toe. Consequently, the proximal slope is significantly steeper than the distal one, a signal whose form is similar to the curvature induced by deposition. We should also expect that this segregation would also appear in the fan's stratigraphy, a process that, to our knowledge, has not been previously investigated in laboratory experiments.

Here, we investigate the impact of a bimodal sediment on the morphology and stratigraphy of an alluvial fan. To do so, we generate a laboratory fan fed with a mixture of two granular materials (Section. 3.2). Our experiment generates a segregated deposit, similar to the laboratory fan of Reitz and Jerolmack (2012). We first analyze its morphology, describing the growth of each part of the deposit independently . We then relate the spatial distribution of the sediment to the proximal and distal slopes (Section. 3.3). Based on these observations, and appealing to the threshold-channel theory, we propose a geometrical model to describe the fan deposit (Section. 3.4).

3.2 Experimental set-up

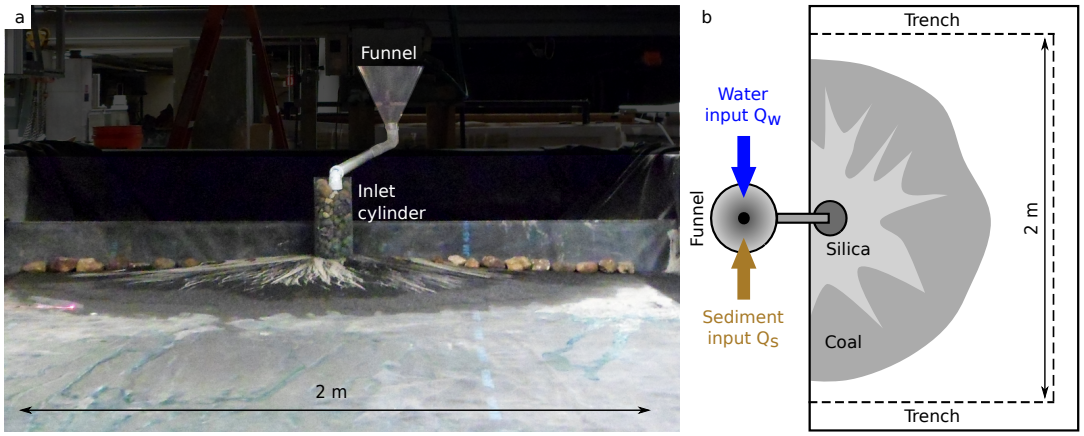

Figure 3.1: Experimental set-up. (a) Front-view picture. (b) Top-view representation.

Producing experimental alluvial fans has become common in geomorphology (Schumm et al., 1987; Bryant et al., 1995; Whipple et al., 1998; Ashworth et al., 2004; Van Dijk et al., 2009; Clarke et al., 2010; Powell et al., 2012; Reitz and Jerolmack, 2012; Clarke, 2015). Here we use a setup similar to that of, for example, Whipple et al. (1998) to generate a radially symmetric fan over a horizontal basal surface (Fig. 3.1). In our experiments, however, a bimodal sediment mixture allows the fan to form a segregated deposit, visualized by color.

The tank we use to produce alluvial fans is 2 m-wide, and more than 5 m-long. Its bottom

is covered with a black rubber tarpaulin. At the back of the tank, a 30 cm-high, vertical wall simulates the mountain front against which the fan leans. To prevent flow concentrations, large pebbles ($\sim$ 5 cm) are placed along the base of this back-wall. The three other sides are bounded by trenches to evacuate water (Fig. 3.1). It is noted that, even with these trenches, the surface tension maintains a 0.5 cm-deep sheet of water over the base of the tank. Assuming that this standing water affects only the base of the fan, we find that it represents less than 1% of its volume. Based on this simple calculation, we hereafter neglect its influence in our analysis and interpretation.

To ensure constant inputs of water and sediment into the experiment, we use a constant-head tank to supply the water, and an Archimedes screw to supply the grains. The fluxes of water and sediment merge in a funnel, which directs them toward the tank. Before reaching the fan, water and sediment flow through a 10 cm-wide, wire-mesh cylinder filled with pebbles. This device reduces the water velocity and homogenizes the mixture (Fig. 3.1).

Table 3.1: Physical characteristics of the sediment. The measurement method is presented in Appendix A. The friction coefficient μ is the tangent of the angle of repose.

	Density	Grain size	
	ρ_s (kg m^{-3})	d_{50} (μm)	d_{90} (μm)
Silica	2650 $\pm$ 50	130	200
Coal	1500 $\pm$ 50	400	800
	Critical Shields	Friction coefficient	
	θ_c	μ	
Silica	0.25 $\pm$ 0.02	0.42 $\pm$ 0.04	
Coal	0.19 $\pm$ 0.008	0.58 $\pm$ 0.04	

The mixture we used is composed of black coal and white silica grains, the colors of which are easily distinguished. The coal grains are larger and lighter than the silica grains (Table 3.1). To quantify the mobility of these grains, we measure their respective transport laws in independent experiments (Appendix A). We find that both transport laws, for pure coal and pure silica, exhibit an unambiguous threshold, below which there is no transport (Fig. 3.2). This threshold is about 0.34 N m^{-2} for coal, and 0.52 N m^{-2} for silica. Beyond this threshold, the sediment flux appears proportional to the distance to threshold, with a proportionality constant of 2.4 10^{-5} m^2 s^{-1} for coal and 4.8 10^{-6} m^2 s^{-1} for silica. As a result, the same shear stress τ induces a larger flux of coal than silica, at least when the two species are unmixed. In other words, despite their larger size, the coal grains are more mobile than the silica ones. This, of course, is due the first being lighter than the latter. To formalize this density-induced reversal of mobility, we need to introduce the Shields parameter θ, which is the ratio of the shear stress over the grain's weight (Shields, 1936):

$$\theta = \frac{\tau}{(\rho_s - \rho) g d_s}, \tag{3.1}$$

where ρ is the density of water, ρ_s is the density of sediment, g is the acceleration of gravity, and we approximate the grain size d_s with its median value d_{50}. For our sediments, the denominator in Eq. (3.1) is larger for silica than for coal, indicating that the density difference prevails over

grain size to govern the mobility of our grains. This is in contrast to the experiments of Reitz and Jerolmack (2012), where the mobility difference is driven by grain size. When expressing the threshold for transport in terms of the Shields parameter, we find $\theta_c = 0.19$ for coal, and $\theta_c = 0.25$ for silica (Table 3.1). These values reinforce the mobility contrast induced by density.

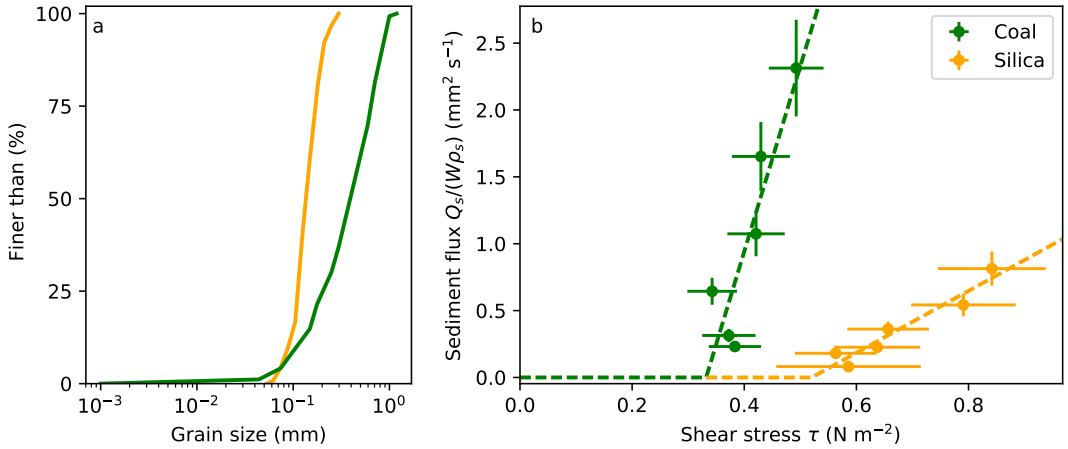

Figure 3.2: (a) Cumulative density function of the grain size. Orange: silica, green: coal. (b) Transport laws. Volumetric flux per unit width, as a function of dimensional shear stress. Dashed lines correspond to Eq. (A.10) fitted to the data (method in Appendix A, coefficients in Table 3.1).

When different grains are mixed, the shear stress exerted on each species depends on the mixture composition (Wilcock and Crowe, 2003; Houssais and Lajeunesse, 2012). The shear stress required to move the larger grains in a mixture is lower than for large grains alone, because the smaller ones cause them to protrude into the fluid. Conversely, small grains in a mixture require a higher shear stress because they are shielded from the flow by neighboring large grains (Einstein, 1950). For grains of different densities but uniform size, exposure and hiding are negligible (Viparelli et al., 2015). There exist no universal transport law accounting for all these phenomena, and deriving an empirical one for our mixture would be a daunting task. We thus use the transport laws of Fig. (3.2) to account for differential transport and estimate the mobility of our grains, although this is certainly a rough approximation. If it holds, at least qualitatively, we expect the rivers that build our experimental fans to segregate the sediment based on grain mobility, by depositing silica while transporting coal further downstream.

Table 3.2: Experimental parameters for the five runs.

Run	Water discharge Q_w (L min^{-1})	Sediment discharge Q_s (L min^{-1})	Silica fraction ϕ
1	2.6 ± 0.1	0.019 ± 0.001	0.5±0.05
2	2.6 ± 0.1	0.045 ± 0.001	0.5±0.05
3	2.6 ± 0.5	0.027 ± 0.001	0.25±0.02
4	2.4 ± 0.1	0.027 ± 0.001	0.25±0.02
5	2.6 ± 0.1	0.020 ± 0.001	0.8±0.08

An experimental run begins with an empty tank. When the mixture of water and sediment

reaches the horizontal bottom of the tank, it forms a half-cone deposit. Initially, a sheet flow spreads uniformly over this sediment body. After a few minutes, the flow confines itself into distinct, radial, channels (typically five or six). All these channels appear to transport sediment simultaneously. The experiment of Reitz and Jerolmack (2012) also produced about 5 channels, although only one of them was active at a time. Both configurations occur in the field (Weissmann et al., 2002; Hartley et al., 2010). In our experiments, bedload appears as the dominant transport mode, although a small amount of fine coal is suspended, and gets deposited on the banks. The width of our channels varies between about 1 and 2 cm. Assuming they share the total water discharge evenly, the typical Reynolds number of their flow is above 500, suggesting that, most of the time, they are turbulent. They avulse regularly to maintain the radial symmetry of the fan. During an avulsion, overbank flow occurs temporarily, a phenomenon also observed by Bryant et al. (1995) and Reitz and Jerolmack (2012). Our experiment stops when the deposit reaches the sides of the tank, typically after 3 to 4 hours.

As it grows, the fan deposits the silica grains upstream of the coal grains. Accordingly, the apex of the fan is mostly composed of silica, whereas coal constitutes most of its toe. The boundary between the two types of sediment follows the path of channels, thus adopting a convoluted shape. To explore the influence of the sediment composition on the morphology of the fan, we varied ϕ, the volumetric proportion of silica in sediment mixture, from 25% to 80% over five experiments (Table 3.2).

3.3 Self-similar growth of a segmented fan

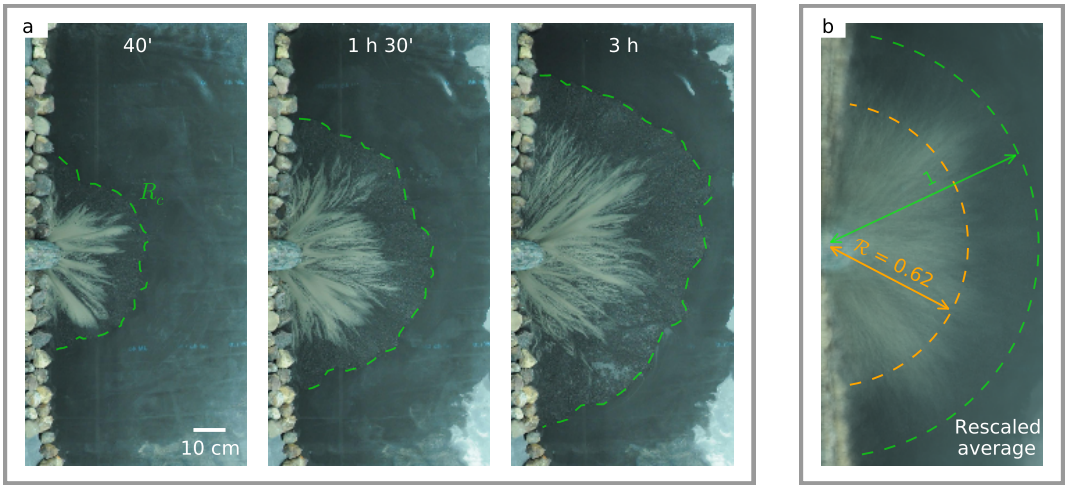

Figure 3.3: Top-view pictures of an experimental fan (run 2). (a) Time evolution. Green dashed line indicates fan toe, R_c. (b) Average of rescaled pictures. The 26 pictures are each 10-minutes apart. Dashed lines indicate silica-coal transition (orange) and fan toe (green). After rescaling, the fan length is one. Transition between silica and coal occurs at dimensionless distance $\mathcal{R}$ from apex.

During each run, we track the evolution of the fan surface with a camera (Nikon D90 with a wide-angle lens Nikon AF DX Fisheye-Nikkor 10.5 mm f/2.8G ED) fixed above the center of the

tank. We record an image every minute (Fig. 3.3a). The exact location of the boundary between silica and coal varies significantly during a run. For a run, however, this boundary appears at a constant location relative to the fan length. This fraction depends on the composition of the sediment mixture (Table 3.3). To confirm this observation, we manually locate the fan toe on 26 pictures, 10 minutes apart from each other (Fig. 3.3a). From these individual measurements, we estimate the average radius R_c of the fan with an accuracy of about 6% on each picture. We then rescale each picture with the corresponding value of R_c, thus normalizing the size of the fan to one. Finally, we average all the normalized pictures of an experimental run (Fig. 3.3b). By construction, the average picture shows a fan of radius one. It also confirms that the fan is radially symmetric, and reveals a somewhat blurred but localized transition between the silica and coal deposits. This observation suggests that the fan preserves the spatial distribution of coal and silica as it grows.

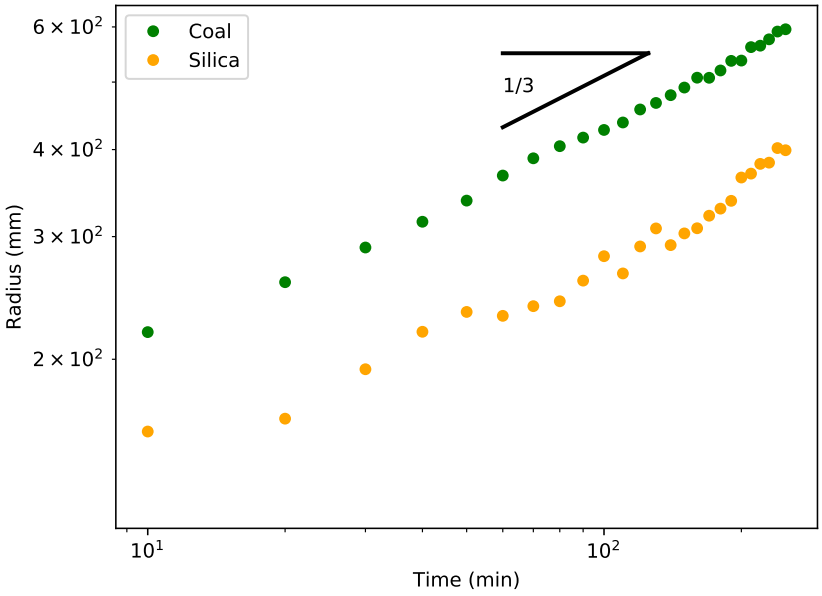

Figure 3.4: Evolution of the radial fronts of the silica (orange) and coal (green) deposits in run 2.

To verify the self-similarity of the fan growth, we analyze the evolution of its geometrical properties. To do so, we manually locate the silica-coal transition and the fan toe (Fig. 3.3a). We then calculate the average distance R_s from the apex to the transition. The boundary of the silica deposit being more convoluted than the toe, the standard deviation of R_s is about 19%. Both distances increase in proportion to the cube root of time (Fig. 3.4). Following Powell et al. (2012) and Reitz and Jerolmack (2012), we interpret this observation as a direct consequence of mass balance. Indeed, the total mass M of the deposit increases linearly with time:

$$M = Q_{s,m}\, t \tag{3.2}$$

where $Q_{s,m}$ is the total mass flux of sediment. To express this relation in terms of volumes, we need to measure the packing fraction λ of our sediment mixture. In general, this quantity

depends on the composition of the mixture. To estimate it, we measure the packing fraction of pure silica, of pure coal, and of a 50 % silica-coal mixture (red dots, Fig. 3.5). The three values are similar, with a mean of $55\% \pm 1\%$. Accordingly, we approximate the packing fraction of the entire deposit with this value, regardless of the composition of the sediment mixture. This approximation introduces an error of less than 5 %. We now define the volume discharge of sediment Q_s, such that

$$Q_{s,m} = Q_s(1-\lambda)\left(\phi\rho_{\text{silica}} + (1-\phi)\rho_{\text{coal}}\right) \tag{3.3}$$

and substitute Q_s for $Q_{s,m}$ in Eq. (3.2). The mass balance then reads

$$V = Q_s\, t \tag{3.4}$$

where V is the total volume of the deposit. In a self-similar fan, any distance scales like the cube root of the fan volume; in particular, both R_c and R_s increase in proportion to $(Q_s t)^{1/3}$. Our experimental fans conform to this scaling, thus supporting the hypothesis of a self-similar growth. A direct consequence of this self-similarity is that the relative location of the transition, defined by the ratio $\mathcal{R} = R_s \,/\, R_c$, remains constant throughout growth ($\mathcal{R} = 0.62 \pm 0.04$ for run 2, other runs are presented in Table 3.3, Figs. 3.3b and 3.4). This self-similarity means that, as it grows, the fan preserves its structure, which can therefore be extrapolated from the final deposit.

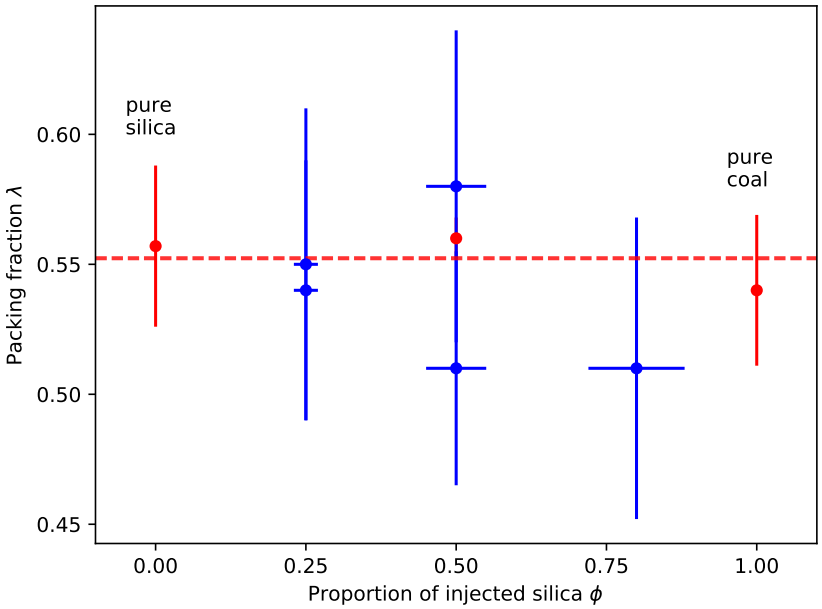

Figure 3.5: Packing fraction of the deposit as a function of the composition of the sediment mixture. Blue dots calculated from experiment. Red dots measured independently. The red dashed line is the mean packing fraction measured independently.

A few minutes after the experiment stops, all the surface water has drained away from the fan, leaving the entire deposit emergent. At this point, we scan the deposit's surface with a laser to measure its topography (OptoEngine MRL-FN-671, 1 W, 671 nm). A line generator converts

the beam into a laser sheet (60° opening angle, 1 mm thick), the intersection of which with the fan surface is recorded by a camera attached to the laser, about 2 m above the tank bottom (Sick Ranger E50, 12.5 mm lens). The precision of the measurement is better than 1 mm in every direction.

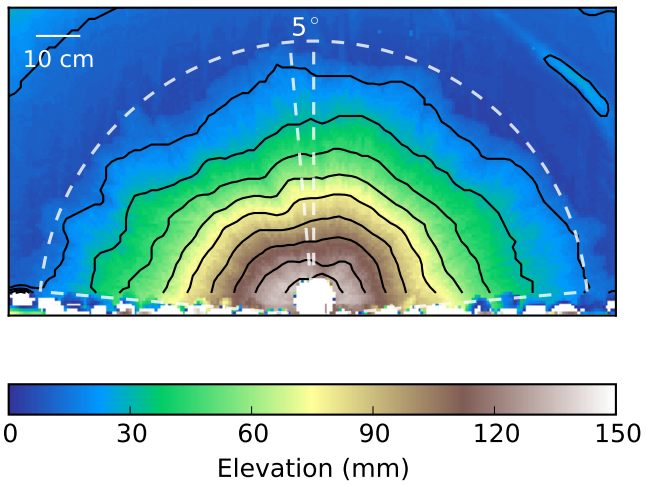

Figure 3.6: Digital elevation model of an experimental fan (run 2). Black lines: elevation contours 15 mm apart from each other. White dashed lines indicate the bounds used for averaging (only two sample radii 5 degree apart are represented for clarity).

Using the digital elevation model (DEM) of our experimental fan, we compute the final volume of our fans to check the total packing fraction of the deposit (blue dots, Fig. 3.5). Despite some dispersion, we find that the packing fraction of our deposit is about 54% ± 2%, close to the value estimated independently.

The elevation contours of the DEM are well approximated by concentric circles, another indication of radial symmetry (Fig. 3.6). This property suggests that we can compute the radially-averaged profile of the fan with minimal loss of information (Reitz and Jerolmack, 2012). To do so, we interpolate the DEM along 34 radii, 5° apart from each other, at the end of each run (Fig. 3.6). For each run, the resulting profiles are similar to each other, and differ from the mean by less than 7% (Fig. 3.7a). The average fan profile is steeper near the apex than at the toe and can be approximated by two segments of uniform slope. Natural fans sometimes feature a similarly segmented profile (Bull, 1964; Blair and McPherson, 2009; Miller et al., 2014). When we plot the downstream slope of this average profile as a function of the distance to the apex, the transition appears as a decreasing sigmoid curve (Fig. 3.7b). To evaluate the location of the transition, and the extension of the transition zone, we fit a hyperbolic tangent to the slope profile (Fig. 3.7b for run 2, other runs in Table 3.3). For run 2, we find that the slope plateaus to a value of about 0.29 near the apex, and to about 0.10 near the toe. We define the location of the transition as the inflection point of the sigmoid, which occurs at 55% ± 9% of the total fan length (Fig. 3.7b). The slope thus breaks where the sediment turns to coal, suggesting that these transitions are closely related (Table 3.3, $\mathcal{R} \approx 0.62 \pm 0.04$). The location of the transition depends on the mixture composition (Table 3.3). We now define the extension of the transition zone as the characteristic length of the sigmoid. For run 2, we find that the transition between

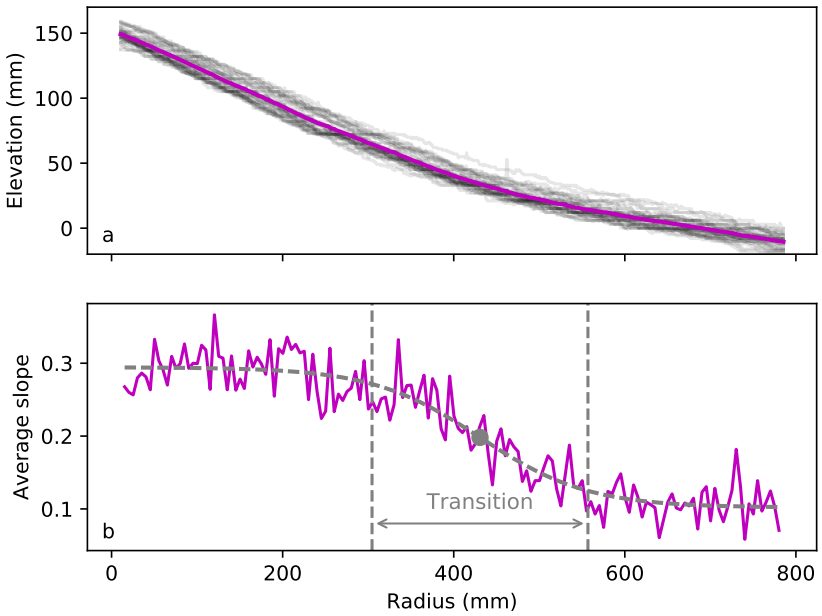

Figure 3.7: (a) Fan profiles at different angles (run 2). Gray: individual profiles; magenta: average profile. (b) Average downstream slope (magenta). Fitted hyperbolic tangent (dashed gray). Inflection point (gray dot) and boundary of the transition area (vertical dashed gray line).

the two segments of the fan occurs over a length of 32% of the total fan length. This value is almost independent of the sediment mixture (about 30% $\pm$ 3% on average for all runs). Miller et al. (2014) found a comparable value (about 22%) for natural and laboratory fans.

To investigate the relation between the slope break and the silica-coal transition, we now turn our attention to the internal structure of the deposit. After the water and sediment supplies have been switched off, the fan remains intact, and we can cut it radially to reveal a vertical cross section (Fig. 3.8). Silica and coal appear segregated, in accordance with the top-view pictures of the fan (Table 3.3), and with the experiments of Reitz and Jerolmack (2012). Silica concentrates near the apex, in the upper part of the deposit, whereas coal concentrates at the fan toe. The location of the silica-coal transition fluctuates, and generate an intricate stratigraphy that combines segregation at the fan scale, and stratification near the transition. The transition zone shows alternating layers of silica and coal, which extend over about one third of the cross-section area. In natural fans, such stratifications result from fluctuations of the sediment and water discharges, but this mechanism cannot be invoked in our experiments (Paola et al., 1992a; Clevis et al., 2003; Whittaker et al., 2011). Dry granular flows can also generate a similar pattern (Makse et al., 1997a,b). In our case, the succession of channel avulsions is another possible mechanism. Our observations do not allow us test these hypotheses.

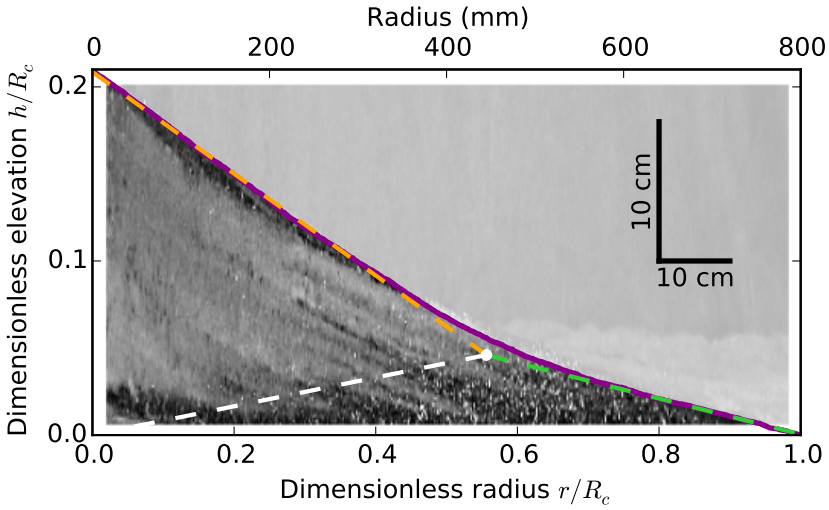

Figure 3.8: Average radial profile (magenta line), superimposed on radial cross section, for run 2. Dashed lines: slope of the silica (orange) and coal (green) deposits. White dashed line indicates silica-coal transition. Scale is for the picture. h and r are respectively the fan elevation and the distance to the apex.

3.4 Mass balance

Based on our laboratory observations, we propose a first-order geometrical model of an alluvial fan fed with a bimodal mixture of sediments. We consider a radially symmetric structure, which grows by expanding itself without changing its geometry. A consequence of these assumptions is that the geometry of the fan, at any time, is entirely determined by a fixed, two-dimensional template of its cross section (Fig. 3.9). The simplest possible template consists of two triangles with a common side. The proximal triangle defines the geometry of the silica deposit, and the distal one represents the coal deposit. Three dimensionless parameters define this template: the proximal slope S_s, the distal slope S_c and the relative location of the transition $\mathcal{R} = R_s/R_c$.

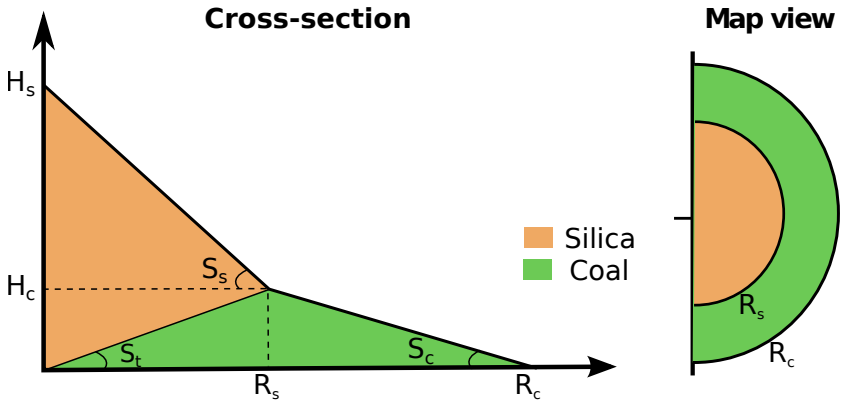

Figure 3.9: Representation of an alluvial fan (template). Silica: orange; coal : green.

The geometry of the template sets the proportion of silica and coal in the deposit. As a consequence, mass balance relates the three parameters that define the fan template to the

composition of the sediment mixture injected in the experiment, ϕ. Indeed, since the sediment discharge is constant, and assuming the deposit is fully segregated and the packing fraction is constant, we should have

$$\frac{V_s}{V_s + V_c} = \phi \,, \tag{3.5}$$

where V_s is the volume of silica in the deposit, and V_c that of coal. For a self-similar fan, this relationship holds at any time.

Table 3.3: Geometrical characteristics of the experimental fans, measured at the end of each run. The errors on $\mathcal{R}$ are due to fluctuations of the silica-coal transition.

Run	Slope ratio $\mathcal{S}$	Transition location $\mathcal{R}$	S_t/S_s $\mathcal{S}_t$
1	3 ± 0.3	0.56 ± 0.07	0.37 ± 0.08
2	2.9 ± 0.1	0.55 ± 0.09	0.36 ± 0.08
3	4 ± 0.6	0.41 ± 0.1	0.57 ± 0.12
4	4.6 ± 0.6	0.39 ± 0.1	0.61 ± 0.13
5	3.3 ± 0.3	0.83 ± 0.2	0.12 ± 0.03

The silica deposit is composed of two half-cones sharing their base. Its volume reads

$$V_s = \frac{\pi}{6} R_s^2 H_s \,, \tag{3.6}$$

where H_s is the elevation of the fan apex. To calculate the volume of coal in the deposit, we first evaluate that of a truncated half cone with slope S_c, radius R_c, and height H_c (the elevation of the transition). We then withdraw the volume of the lower cone of the silica deposit. The resulting volume reads

$$V_c = \frac{\pi}{6} \left(R_c^2 + R_c R_s \right) H_c \,. \tag{3.7}$$

The proximal and distal slopes are simply those of the corresponding right triangles:

$$S_s = \frac{H_s - H_c}{R_s} \quad \text{and} \quad S_c = \frac{H_c}{R_c - R_s}. \tag{3.8}$$

Using the four above equations, we finally relate the composition of the sediment mixture to the geometry of the fan, as a function of the slope ratio and the transition location:

$$\phi = \frac{(1-\mathcal{S})\mathcal{R}^4 - \mathcal{S}\mathcal{R}^3 - \mathcal{R}^2}{(\mathcal{R}+1)\left((1-\mathcal{S})\mathcal{R}^3 - 1\right)} \,, \tag{3.9}$$

where we have defined the ratio of proximal slope to distal slope $\mathcal{S} = S_s/S_c$. Equivalently we may express the composition of the sediment mixture as a function of the slope ratio and the slope of the transition:

$$\phi = \frac{1 - \mathcal{S}_t}{1 + \mathcal{S}_t \left((\mathcal{S}\mathcal{S}_t)^2 + 3\mathcal{S}\mathcal{S}_t + 2 \right)} \,, \tag{3.10}$$

where we have defined the ratio of transition slope to proximal slope $\mathcal{S}_t = S_t/S_s$.

If the template is a reasonable representation of the fan geometry, the location and the slope of the transition and the two surface slopes of the deposit should adjust to the composition of the

sediment input, according to Eqs. (3.9, 3.10). To evaluate this model, we measure the geometry of the fan at the end of every experimental run (Table 3.3). Using the radially averaged profile we first fit, using a linear regression, the proximal and distal slopes and calculate their ratio. Then, we estimate the location of the transition using the position of the inflection point (Section. 3.3). We find that, for all runs, the proportion of silica in the deposit, as deduced from our measurements through Eqs. (3.9, 3.10), matches the composition of the sediment mixture (Fig. 3.10).

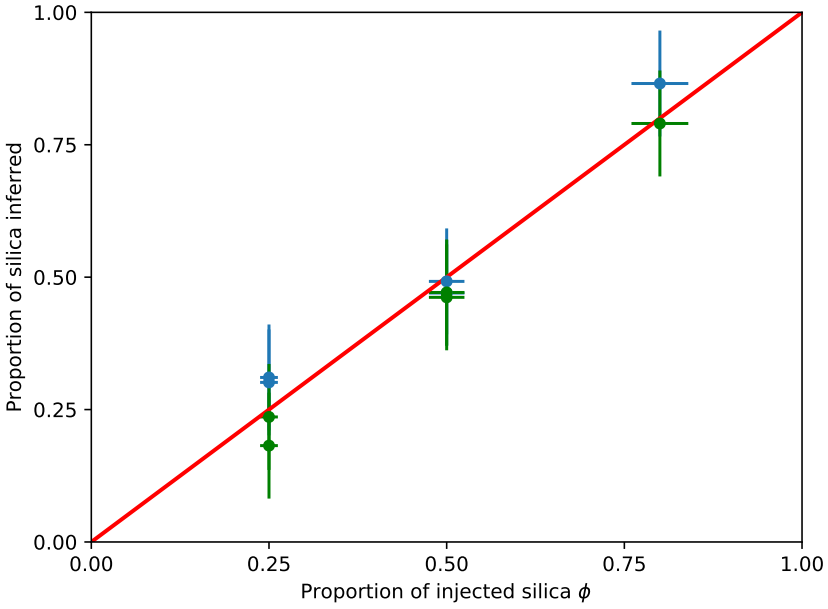

Figure 3.10: Proportion of silica inferred from the geometry of the deposit, after Eq. (3.9) (blue) and after Eq. (3.10) (green), as a function of the composition of the sediment input. Red line: perfect agreement.

At first order, we can thus represent our experimental fan as a radially symmetric, fully segregated structure which preserves its shape as it grows. These features determine the dynamics of the fan, and the geometry of its deposit. This model, however, involves two free parameters: the proximal and distal slopes. These are selected by the fan itself, by a mechanism that remains to be understood. Each deposit is built by a collection of channels, which select their own slope according to the composition of the bed, and to their sediment and water discharges. On the DEM of our experimental fans, the channels are virtually invisible, showing that their downstream slope is that of the fan (Fig. 3.6). It is thus reasonable to assume that the deposit inherits the slope of the channels that build it. The way a river selects its morphology is still a matter of debate, but it has been recently pointed out that most laboratory rivers, including those flowing over an experimental fan, remain near the threshold for sediment transport (Reitz and Jerolmack, 2012; Seizilles et al., 2013; Reitz et al., 2014; Métivier et al., 2017). Assuming a channel is exactly at threshold yields a theoretical relationship between its water discharge and its slope (Glover and Florey, 1951; Henderson, 1961). Could this theory inform us about the slope of our fans?

Returning to our experimental fans, we find them enmeshed in a collection of channels flowing radially (Fig. 3.11). These channels sometimes bifurcate downstream, but do not recombine as they would in a braided river. We would like to compare their slope to the prediction of the

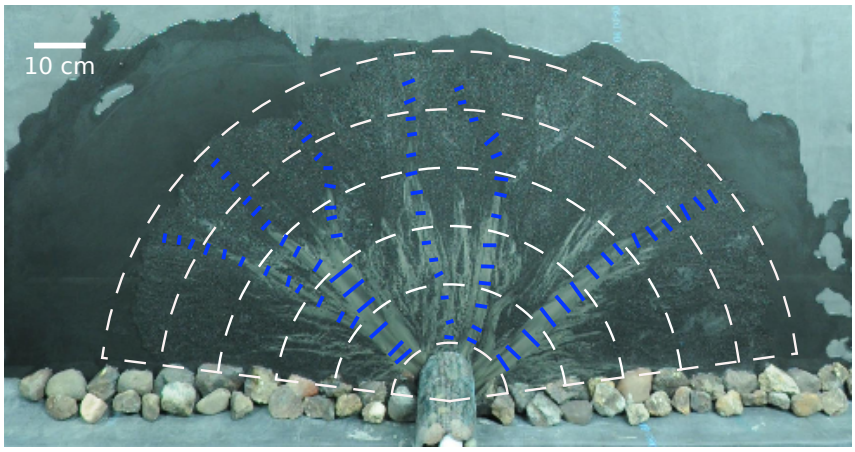

Figure 3.11: Top-view of an experimental fan superimposed with measurement bins (white), and channels cross sections (blue).

threshold-channel theory. Unfortunately, our experimental setup does not allow us to measure the water discharge of individual channels. If the flow distributes itself evenly among the channels, though, we can approximate their individual discharges to a fraction of the total discharge. To evaluate this approximation, we now analyze top-view pictures of our developing fans (about 15 pictures per run). We first divide the surface of each fan into five concentric bins, where we count the active channels and measure their widths (at least two cross sections per channel and per bin, Fig. 3.11). We then average the number of channels, and their width, over experimental runs. The resulting quantities depend on the time of their measurement, and on the distance from the apex, r. Further averaging over time yields radius-dependent quantities, whereas averaging over distance yields time-dependent quantities (Fig. 3.12).

When plotted as a function of radius, the width of the channels varies between about 1 and 2.5 cm, with no clear trend (Fig. 3.12a). The variability of the width is much larger in the proximal part of the fan than in its distal part. When plotted as a function of time, we find that the width is more consistent, with a relative variability of about 10% around a mean value of 1.3 cm (Fig. 3.12b). Overall, the channels appear reasonably homogeneous in size, suggesting that they share the total water discharge evenly.

The number of channels n_c varies between 5 and 6 across the fan (Fig. 3.12c). As expected for a radially oriented structure, we count fewer channels near the apex. We also find fewer channels near the toe, although the poor color contrast of the coal-dominated areas probably bias our count. This variability compares with the disparity we observe between runs. The number of channels is nearly constant over time (Fig. 3.12d). Hereafter, we choose $n_c = 5.5$, and divide the total water discharge accordingly.

We now wish to compare the slope of our experimental fans with the threshold theory, applied to the characteristic channel defined above. This theory assumes that the combination of gravity and flow-induced shear stress maintains the channel bed at the threshold of motion (Glover and Florey, 1951; Henderson, 1961; Seizilles et al., 2013). As a result, the width, depth and slope of the channel are set by its water discharge. In particular, according to the simplest version of this theory (Devauchelle et al., 2011; Gaurav et al., 2015; Métivier et al., 2017), the equilibrium slope

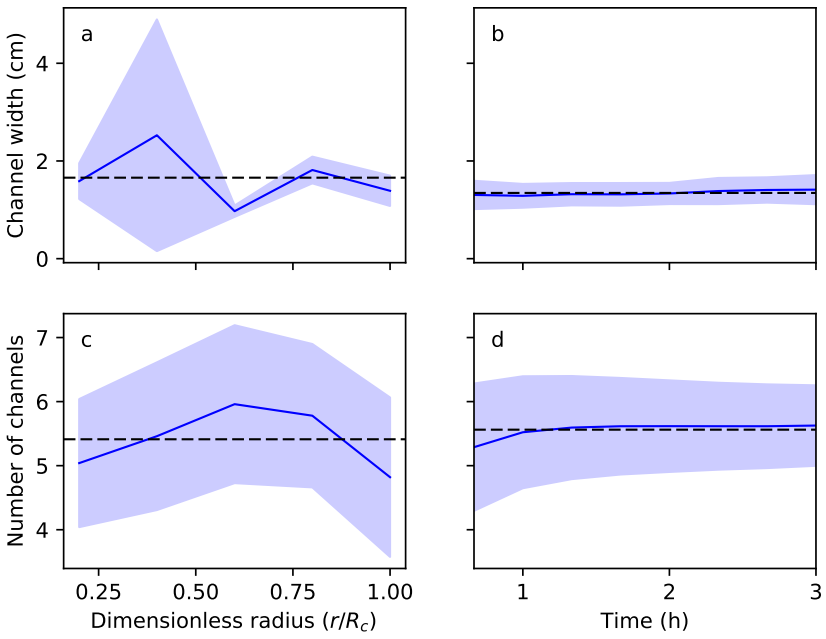

Figure 3.12: Evolution of active channels for all the runs. Channel width as a function of the dimensionless radius (a) and time (b). Number of channels as a function of dimensionless radius (c) and time (d). Black dashed line: average. Shaded area: variability over experimental runs.

reads

$$S_H = \left(g\ \mu^3 \left(\frac{\theta_c}{\mu} \frac{\rho_s - \rho}{\rho} d_s \right)^5 \right)^{1/4} \sqrt{\frac{2^{3/2}\,\mathcal{K}(1/2) n_c}{3\,C_f\,Q_w}}, \tag{3.11}$$

where μ is Coulomb's coefficient of friction (Table 3.1), $\nu = 10^{-6}$ m^{2}s^{-1} is the kinematic viscosity of water, $\mathcal{K}(1/2) \approx 1.85$ is the elliptic integral of the first kind, and C_f is Chézy's coefficient of fluid friction. The Chézy coefficient C_f depends on the bed roughness and the flow Reynolds number. For simplicity, we approximate C_f with a constant value of 0.02 (Moody, 1944; Chow, 1959). Since we imposed the same water discharge during all experimental runs, and found the number of channels n_c to be relatively constant, the slope corresponding to the threshold theory depends on the sediment only. We find $S_{Hs} \approx 0.042$ for silica, and $S_{Hc} \approx 0.023$ for coal, using Eq. (3.11).

Intuitively, we expect that, all things being equal, the fan slope increases with sediment discharge. Previous observations support this intuition, but there is no consensus yet about its physical origin, which involves the response of a single channel to sediment transport and its destabilization into multiple threads (Whipple et al., 1998; Ashworth et al., 2004). We do not find any correlation between sediment discharge and slope in our experiment (Fig. 3.13). Even after normalizing our measurements according to the threshold theory, the data points appear segregated according to the sediment species: the mean slope of the silica deposit is about $S_s/S_{Hs} = 5.6 \pm 2.0$, whereas we find $S_c/S_{Hc} = 2.9 \pm 1.5$ for coal ($S_s \approx 0.23$ and $S_c \approx 0.068$). The surface slopes of the two fan segments are thus significantly higher than predicted by the threshold theory.

A possible cause for this departure from the threshold channel could be the bimodal mixture

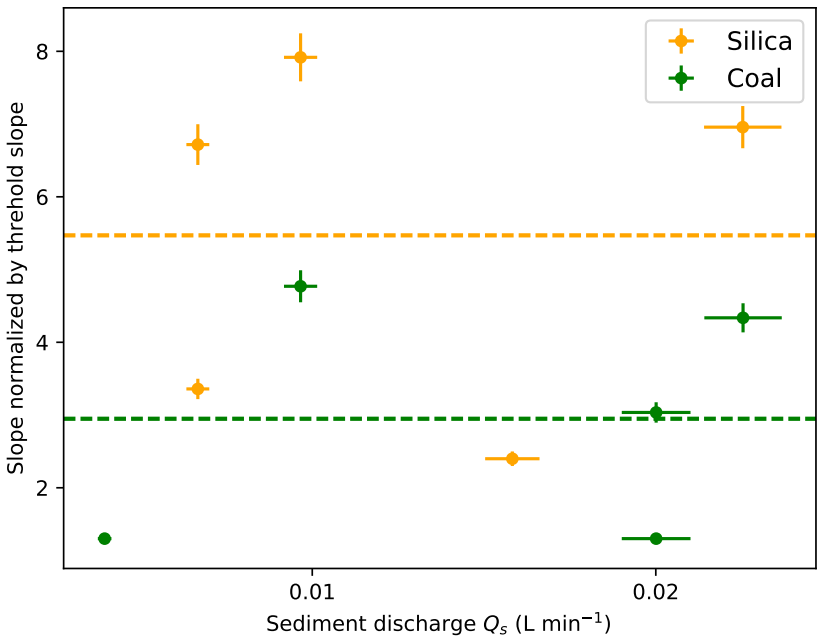

Figure 3.13: Slope normalized by the threshold slope, calculated with Eq. (3.11), as a function of the sediment discharge. Dashed lines: average slopes.

we use. To assess this hypothesis, we have produced an experimental fan with pure silica ($Q_s \approx 0.014$ L min^{-1}, $Q_w \approx 2.6$ L min^{-1}). We found that, like its bimodal counterparts, its slope was approximately five times higher than predicted by the threshold-channel theory ($S_s = 0.2$). Another possible explanation is the infiltration of surface water into the deposit. Indeed, based on Eq. (3.11), a lower water discharge induces a steeper channel. Measuring this leakage would be experimentally challenging. Finally, the breakdown of the threshold-channel theory could result from sediment transport, since active channels must be above threshold (Whipple et al., 1998; Guerit et al., 2014). In their one-dimensional experiment, Guerit et al. (2014) have shown that the higher the sediment input in their experiment, the more slope departs from its threshold value. Again, we cannot evaluate quantitatively this hypothesis in our experiments.

The proximal and distal slopes seem independent from sediment discharge (Fig. 3.13). For lack of a physical interpretation, we now treat this observation as an empirical fact, and attribute a fixed value to the ratio of proximal slope to distal slope: $\mathcal{S} = S_s/S_c = 3.4 \pm 1.0$. Substituting this value in Eqs. (3.9, 3.10), the mass balance relates, without any additional parameters, the composition of the sediment mixture to the location and the slope of the transition (Fig. 3.14). Despite significant uncertainties, which probably reflect the rudimentary mass balance we used, our observations agree with this semi-empirical relationship.

In principle, one could use Fig. (3.13) to infer the composition of the sediment input from the geometry of the deposit. This method, however, relies on the value of the slope ratio $\mathcal{S}$, which we have fitted on our observations. A more comprehensive theory should explain how a bimodal fan spontaneously selects the value of this ratio.

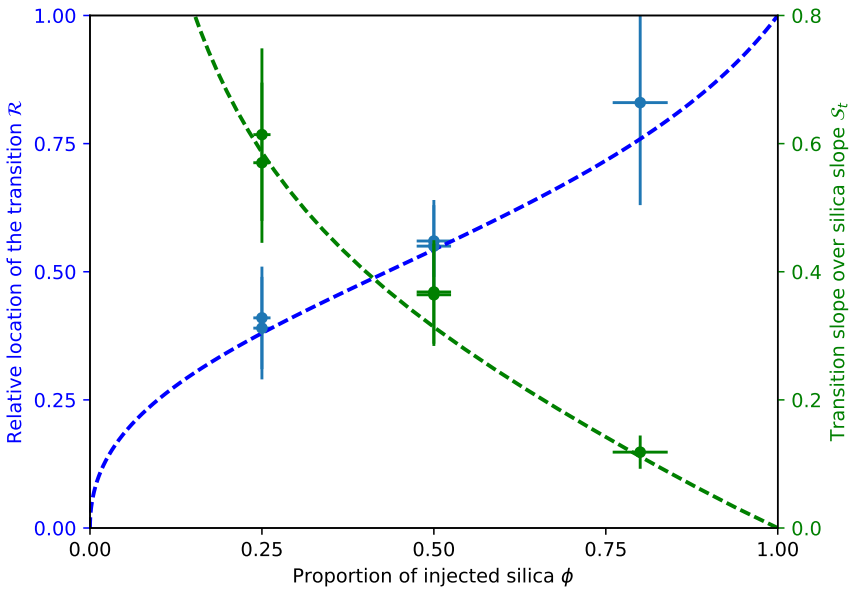

Figure 3.14: Relative position of the transition $\mathcal{R}$ (blue) and dimensionless transition slope $\mathcal{S}_t$ (green), as a function of the composition of the sediment input. Dot: experimental measurements. Dashed line: Eqs. (3.9, 3.10) with $\mathcal{S} = 3.4$.

3.5 Conclusion

Using a laboratory experiment, we generated alluvial fans fed with a bimodal sediment. Five or six active channels deposit their sediment load to form a radially-symmetric fan. The heavier sediment (silica) concentrates around the apex, whereas the lighter one (coal) get deposited near the toe. The location of silica-coal transition fluctuates over about 30% of the total fan length. A radial cross section of the deposit reveals a similar segregation: two superimposed triangles make up the stratigraphy of the fan. The lowest triangle is mostly coal, whereas the upper one, located near the apex, is mostly silica. The transition between the two parts of the fan fluctuates to produce strata, which extend over 30% of the total fan length. As a first approximation, we may represent this transition with a straight line, and treat the fan structure as two imbricated deposits. Combining this geometric model with mass balance, we find that the fan preserves this structure as it grows, with a precision of about 15%. This observation suggests that our laboratory fans act essentially as sieves, which segregates the sediment they are fed with. This process controls the geometry of the resulting deposit. As a consequence, we can use the final geometry of our laboratory fans to infer the composition of the sediment input. In practice, a top-view picture of the deposit suffices to do so. Alternatively, measuring the slope of the transition in the stratigraphy, even if the latter is incomplete, also suffices.

Natural fans often exhibits a sharp transition from gravel to sand (Blair and McPherson, 2009; Miller et al., 2014). Like in our experiments, this front divides the fan profile into two segments. The proximal segment, composed mainly of gravel, is steeper than the distal one, composed mainly of sand. Bull (1964) and Blair (1987a) found natural fans featuring three segments bounded by two successive transitions. Again, the size of the deposited sediment changes abruptly at each front. These observations suggest that the segregation mechanism at work in

our experiment can repeat itself to generate nested deposits. A natural extension of our work would be to enrich the sediment mixture with additional grain sizes (or densities) to produce fans with multiple segments. We would expect these fan to sort sediment species based on their mobility, and reduce their slope downstream, as observed on the surface of many natural fans (Stock et al., 2008). In other words, the structure of an alluvial fan should reflect the composition of its sediment input. For instance, in principle, one could infer the grain-size distribution of the sediment input from a DEM of the fan.

In practice, however, secondary processes such as weathering, runoff, and aeolian erosion reworks the surface of most natural fans, thus hampering our ability to infer their history from their present state (de Haas et al., 2014). To circumvent this issue, one can either reconstruct geometrically the paleosurface of the fan, or use its stratigraphy. Indeed, even partial access to the internal structure of the fan could reveal the slopes of the transitions in the stratigraphy, and thus the grain-size distribution of the input.

In our experiments, the inputs of water and sediment were constant. In general, this is not true for natural fans, and the interpretation we propose here does not apply in its present, oversimplified, form. The self-similar model we propose here thus cannot account for climatic and tectonic signals. However, the fundamental hypothesis upon which it relies, namely that the fan sorts the sediments based on their mobility and adjusts its own slope accordingly, might still hold when the inputs fluctuate. If so, our geometrical model might be extended to account for these fluctuations. This is the subject of present work.

Our experiments also suggest that the process by which an alluvial fan distributes grain sizes in its deposit, although a primary control on its structure, may not be the most puzzling component of its machinery. The way it selects its slope remains a challenging problem, which we have circumvented here by fitting a parameter to our observations (Le Hooke and Rohrer, 1979; Whipple et al., 1998; Stock et al., 2008; Van Dijk et al., 2009; Powell et al., 2012; Guerit et al., 2014). Indeed, the threshold theory can only provide us with a first-order estimate for the slope of a channel. We need to understand how a channel adjusts its slope to its sediment load. Recent investigations have shown that, provided the sediment discharge is low enough, one can produce stable active channels in laboratory experiments (Seizilles et al., 2013; Métivier et al., 2017). If this method works for a laboratory fan as well, it might generate a single-channel fan. This would be a simpler experimental tool to investigate the relationship between the slope of a fan and the intensity of its sediment input.

Chapter 4

Departure from threshold: finite sediment discharge

Comme nous l'avons vu précédemment, l'augmentation du flux de sédiment a plusieurs conséquences sur la morphologie et la dynamique de croissance d'un cône alluvial. Premièrement, l'augmentation du flux de sédiment augmente la fréquence d'avulsion (Bryant et al., 1995; Sinha, 1998; Ashworth et al., 2004; Assine, 2005; Reitz et al., 2010). Deuxièmement, en considérant la conservation de la masse, un flux de sédiment plus important accroît également la vitesse de croissance du cône (Reitz and Jerolmack, 2012; Powell et al., 2012, Section. 2.3). Troisièmement, une augmentation du flux de sédiment modifie le profil en long du cône (Whipple et al., 1998; Stock et al., 2008; Guerit et al., 2014). Dans ce chapitre, nous nous intéressons à cette dernière influence. Dans le chapitre 2, nous avons montré que la pente d'un cône proche du seuil de mise en mouvement des sédiments atteint une pente critique, S_h, qui est contrôlée par la taille des sédiments, d_s, et le débit de fluide, Q_w. Pour comprendre comment l'augmentation du flux de sédiment éloigne la pente de cette valeur seuil, nous utilisons les travaux d'Abramian et al. (prep) concernant la forme d'équilibre d'une rivière transportant des sédiments. Nous montrons ensuite comment l'étude de la pente d'un cône alluvial permet de remonter au flux de sédiment qui l'a construit.

4.1 Influence of sediment transport on alluvial river

In chapter 2, we demonstrate that when a river does not transport sediment, its shape is maintained by a force balance between gravity and the flow-induced shear stress. When the river transports sediment, grain are advected on average along the flow, but a transverse sediment flux appears. Because of the bank slope, gravity pulls the moving grains away from the banks toward the center of the channel (Parker, 1978b, Fig. 4.1). Consequently, the river widens. For a river to reach and maintain an equilibrium shape, sediments must then be transported from the center of the channel to the banks. Looking at the motion of grains in a laboratory channel, Seizilles et al. (2014) demonstrate that this motion follows a random walk in the transverse direction (Fig. 4.1). Sediments diffuse from the center of the bed to the banks. At equilibrium, the inward gravity flux balances the outward diffusive flux.

The gravity flux, q_g, is proportional to the surface concentration of moving grains, n, and to the bank slope, such as,

$$q_g = \alpha n V_s \frac{\partial D}{\partial y}, \tag{4.1}$$

where α is a dimensionless coefficient, V_s the grains velocity, D the channel depth and y the transverse direction. The diffusive flux, q_d, can be measured experimentally (Seizilles de Mazancourt, 2013; Seizilles et al., 2014). It reads

$$q_d = -l_d V_s \frac{\partial n}{\partial y}, \tag{4.2}$$

where l_d is a diffusive length, which depends on the sediment shape and fluid characteristic.

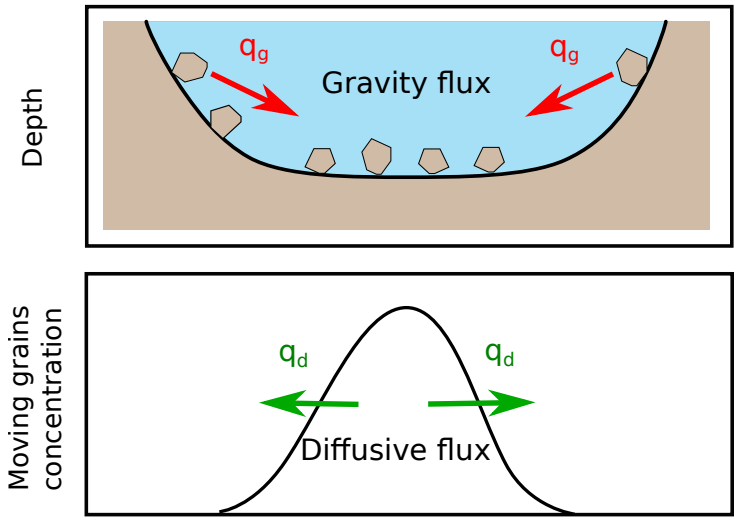

Figure 4.1: Conceptual model of sediment flux in the transverse direction y of a river.

To maintain the equilibrium shape of the river, the diffusive flux must balance the gravity flux, hence

$$l_d \frac{\partial n}{\partial y} = \alpha n \frac{\partial D}{\partial y}. \tag{4.3}$$

Integrating Eq. (4.3) leads to

$$n = n_0 e^{D\alpha/l_d}, \tag{4.4}$$

where l_d, can be measured in a laboratory channel. The surface concentration of moving grain, n, depends on the force exerted by the flow on the sediment bed (Lajeunesse et al., 2010, Appendix A),

$$n = \frac{\beta}{d_s^2}(\mu - \mu_t), \tag{4.5}$$

where β is a dimensionless coefficient. Finally, combining Eqs. (2.3), (4.4) and (4.5) leads to

$$\left(\sqrt{\tilde{D}^2 + \tilde{D'}^2} - \mu_t\right) e^{-\tilde{D}/\epsilon} = \tilde{n_0}, \tag{4.6}$$

where we introduce a dimensionless depth $\tilde{D} = D\,S/\mathcal{L}$, a dimensionless position $\tilde{y} = y\,S/\mathcal{L}$, and we define $\epsilon = S\,l_d/\alpha\mathcal{L}$ and $\tilde{n_0} = n_0 d_s^2/\beta$. The value of $\tilde{n_0}$ depends on the fluid and sediment fluxes (Abramian et al., prep). This equation has no simple analytical solution. To study the solution of Eq. (4.6), Abramian et al. (prep) represent the phase portrait $(\tilde{D}, \tilde{D}')$ for different values of $\tilde{n_0}$ at ϵ constant (Fig. 4.2). In this phase portrait, each value of $\tilde{n_0}$, that defines a solution of Eq. (4.6), is represented by a semi-circular trajectory (Abramian et al., prep, Fig. 4.2a). These solutions are comprised in a narrow region bounded by two asymptotic solutions (red line and green dot in Fig. 4.2a).

The first asymptotic solution corresponds to a river at the threshold of sediment motion $\tilde{D} = \mu_t$ everywhere across the bed (Glover and Florey, 1951, Section. 2.1). In this case, the river cross-section has a cosine shape (Eq. 2.5). The second one is a fixed point which corresponds to an infinitely wide river, $\tilde{D} = \mu_t + \epsilon$ (Seizilles de Mazancourt, 2013; Abramian et al., prep). In the phase space, the distance between these two asymptotic solutions is equal to ϵ, thus proportional to the river slope. Consequently, when the slope becomes small, solutions of Eq. (4.6) tend toward the threshold of sediment motion. In this limit, the river cross section can be decomposed in two components. The banks are represented by two half cosines (Eq. 2.5). They are at the threshold of sediment motion and do not contribute to sediment transport. The central part of the channel is flat and slightly above the threshold of sediment motion. Sediment transport occurs only in this flat section.

In the limit of this assumption, and using the sediment and fluid mass balances we define a first-order approximation for the slope of a river that transports sediment (Abramian et al., prep),

$$\frac{S}{S_h} = \left(1 + \frac{Q_s}{Q_s^*}\right)^{1/3}, \tag{4.7}$$

where Q_s^* is a characteristic sediment flux: $Q_s^* = 4q_0 l_d/3\alpha$, with q_0 the characteristic sediment discharge per unit of river width measured with the transport law $q_s = q_0(\mu - \mu_t)$ (Appendix A). We now suggest to compare this theory (Eq. 4.7) to the slope of an experimental fan when the sediment discharge increases.

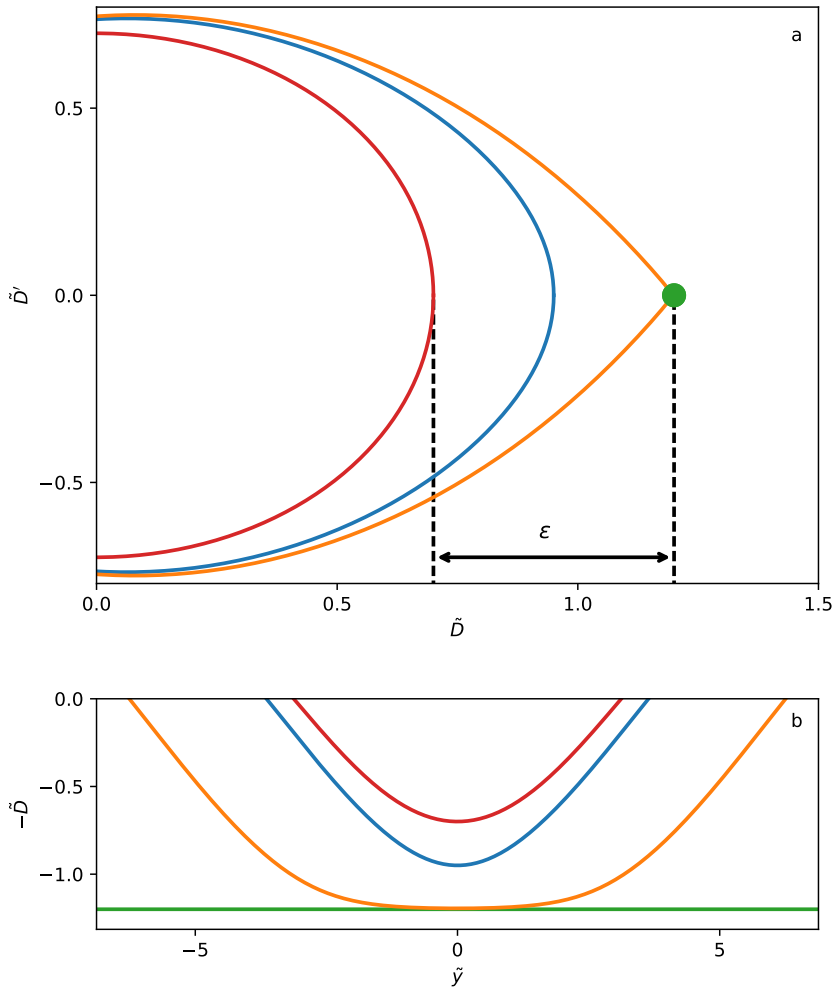

Figure 4.2: a) Phase portrait, b) River cross-section, solutions of Eq. 4.6 for different values of $\tilde{n_0}$. The red lines represent the first asymptotic solution, where $\tilde{D} = \mu_t$, the river cross-section is a cosine. The green dot is the fixed point, it correspond to the second asymptotic solution, where $\tilde{D} = \mu_t + \epsilon$, the corresponding river is flat. The blue and orange lines represent two solutions for different $\tilde{n_0}$.

4.2 Fan profile

To quantify the influence of the sediment discharge on a fan morphology, we use the same experimental set-up as the one described in chapter 2. The sediment and fluid characteristics are also the same. We perform 14 experiments with constant fluid Q_w and sediment Q_s discharges. Table. 4.1 lists the values of Q_w and Q_s used in each experiment.

We use the moiré technique previously described (Chapter 2 and Appendix C.2) to measure the slope of our experimental fan. To compare the slope for different sediment discharge, we normalize the fan elevation, h, and the distance from the apex, r, by the radius, R, of the fan. Qualitatively, we observe that, for a constant fluid discharge, the fan slope increases with the sediment discharge (Fig. 4.3). When the sediment discharge becomes small, the fan slope reaches a minimum value. These observations qualitatively agree with the theory (Section. 4.1). The river that builds the alluvial fan deposits its load along the fan. As a consequence, the sediment

Table 4.1: Experimental parameters for the 14 runs. The error on the sediment discharge corresponds to the sediment deposited in the inlet channel, which is geometrically estimated.

Fluid discharge Q_w ($\mathrm{L\,min^{-1}}$)	Sediment discharge Q_s ($\mathrm{g\,min^{-1}}$)	Sediment discharge Q_s ($\mathrm{g\,min^{-1}}$)	Fluid discharge Q_w ($\mathrm{L\,min^{-1}}$)	Sediment discharge Q_s ($\mathrm{g\,min^{-1}}$)
	0.13 ± 0.0084	1.68 ± 0.048		0.82 ± 0.024
	0.49 ± 0.0056	3.08 ± 0.12	0.73 ± 0.02	4.9 ± 0.15
0.33 ± 0.02	0.68 ± 0.013	4.83 ± 0.14		8.1 ± 0.28
	0.74 ± 0.016	6.18 ± 0.26		
	0.77 ± 0.019	13 ± 0.36		
	1.22 ± 0.028			

discharge decreases downstream. Following the decrease of sediment discharge, the slope of the fan should diminish near the fan toe (Guerit et al., 2014). The profiles of Fig. (4.3) do not exhibit a clear concavity, even though they merge near the fan toe. In our experiments, the sedimentary load is entirely deposited into the fan, since the sediment discharge vanishes at the toe. Consequently, the slope near the fan toe should be the equilibrium slope S_h (Chapter 2).

To test this assumption, we extract the fan slope near its toe. To do so, we extract the slope where the dimensionless radius of the fan, r/R, lies between 0.9 and 1. We then compare these distal slopes to the threshold slopes reach for the corresponding water discharge (Fig. 4.4a). Accordingly to the results of chapter 2, we find that the slope at the fan toe is approximately equals to twice the threshold slope. For the four experiments involving the higher sediment discharge, however, we measure deeper slopes than the one predicted. A possible explanation of this difference is the short duration of the experiments. In fact, we observe in chapter 2 that the time required to reach the threshold slope is approximately 10 hours. When we impose a high sediment discharge the fan reaches the tank boundary before 10 hours. Consequently, we stop the experiment.

Due to sediment deposition along the fan, we only know the sediment discharge near the fan apex. Accordingly, to quantify the influence of sediment discharge on the fan slope, we consider the proximal slope of our fans. However, the presence of the channel at the inlet of the fan disturbs the profile, which can be reversed or flat (Fig. 4.3). To have the best measurement of the proximal slope of our fan, we extract it where the dimensionless radius, r/R, lies between 0.1 and 0.4. Our two sets of experiments involve different water discharge (Table. 4.1). Consequently, their equilibrium slopes, S_h, differ (Chapter 2). To investigate the departure from this threshold slope, we represent the proximal slope of our fans normalized by the equilibrium slope, S/S_h, as a function of the sediment discharge injected into the experiment (Fig. 4.4b).

Figure (4.4b) shows that the data from the two sets of experiments collapse on the same trend. This means that the influence of the fluid discharge is totally captured by the threshold slope S_h. The fluid discharge therefore only controls the threshold slope. Contrary to previous study, here we separate the influence of fluid and sediment discharges (Whipple et al., 1998; Van Dijk et al., 2009; Clarke et al., 2010; Powell et al., 2012). We then fit Eq. (4.7) on the data to estimate the threshold slope, S_h, and the characteristic sediment discharge Q_s^*. We find that

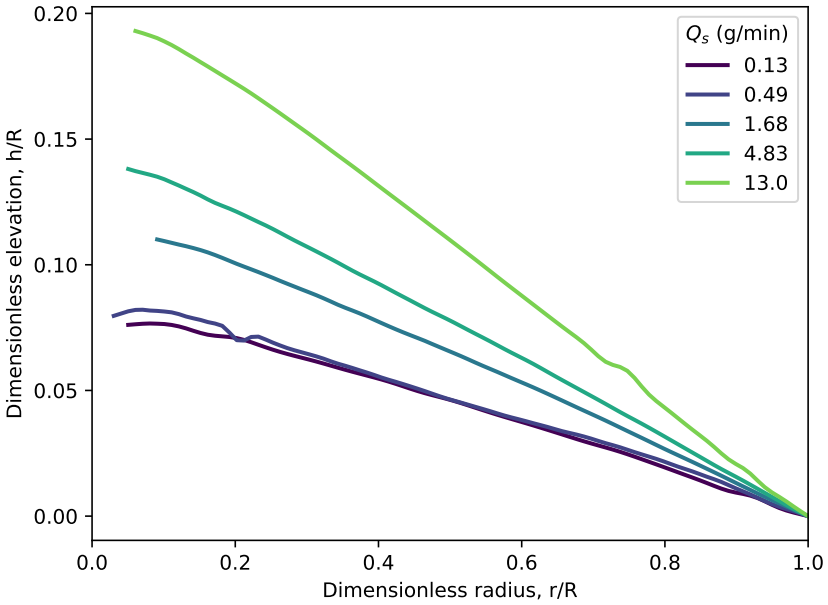

Figure 4.3: Normalized fan profiles for five experiments ($Q_w = 0.33$ L min^{-1}, Q_s varies from 0.13 to 13 g min^{-1}).

the characteristic sediment discharge is about 0.7 g min^{-1} and the threshold slope is 1.9 times the theoretical one. The value of the characteristic sediment discharge depends on the sediment characteristic (d_s, ρ_s) and the diffusive length l_d. In agreement with the observation of chapter 2, the threshold slope is two times higher than the theoretical one, hence $S/S_h = 1.9$, when $Q_s = 0$. Despite this underestimation of about 2, the slope of the fan departs from threshold following the theoretical prediction of Eq. (4.7).

The sediment deposition along the fan generates a concave up profile. Consequently, the volume of our experimental fan cannot be approximated by a semi-cone anymore. The volume of the fan is the volume of sediment injected into the experiment,

$$V = \frac{Q_{s0}t}{1-\lambda} \tag{4.8}$$

To quantify the departure from threshold, we define a volume ratio

$$\mathcal{V} = \frac{V}{V_h} = \frac{6Q_{s0}t}{(1-\lambda)\pi S_h R^3}. \tag{4.9}$$

This volume ratio correspond to the fan volume divided by the volume of a threshold fan, V_h built with the same fluid discharge and composed of the same sediment. In equation (4.9), we note that the volume ratio depends on the aperture angle of the fan (here, this angle is equal to π).

With these experiments, we have quantified the influence of sediment discharge on the slope (Eq. 4.7). Due to sediment deposition along the fan, the slope of the fan shallows along its radius following Eq. (4.7). Using this equation, coupled with mass balance, we can calculate the theoretical fan profile and volume numerically. The next section details this reasoning.

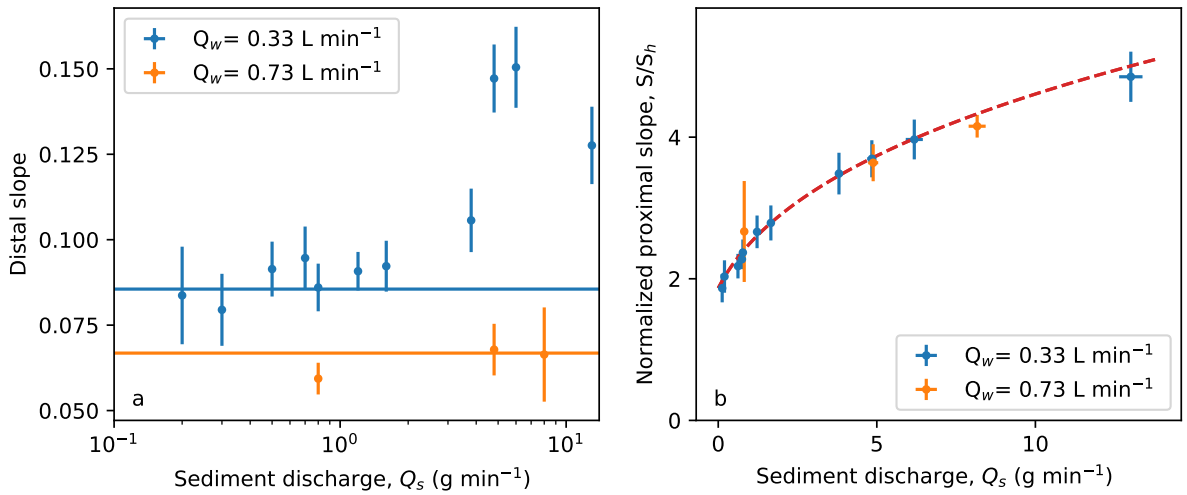

Figure 4.4: Slope of the fan as a function of the sediment discharge. a) Distal slope. Colored areas, threshold slope S_h multiply by a prefactor of two to be in accordance with the result of chapter 2. b) Normalized proximal slope. Red dashed line, Eq. (4.7) with Q_s^* and S_h fitted on the data.

4.3 Mass balance

The fan grows from sediment deposition. This mechanism is described by the sediment mass balance:

$$(1-\lambda)\pi r\frac{\partial h}{\partial t}+\frac{\partial}{\partial r}(Q_s)=0, \tag{4.10}$$

where h is the fan elevation. The relation between the slope of a river and its sediment discharge (Eq. 4.7) allows us to define the sediment transport equation along the fan

$$\frac{Q_s}{Q_s^*}=\left(\frac{S}{S_h}\right)^3-1. \tag{4.11}$$

To solve Eqs. (4.10) and (4.11), we need to define three boundary conditions:

- At the inlet, the sediment discharge is controlled by the experimental input, $Q_s(0,t)=Q_{s0}$.
- We assume that all sediments are trapped into the fan, consequently, at the fan toe the sediment discharge vanishes, $Q_s(R,t)=0$.
- Finally, by definition, the fan elevation vanishes at its toe, $h(R,t)=0$.

Because the fan grows with time, its radius evolves so we can not define R *a priori*. The domain over which we must solve the mass balance equation has a free boundaries. One way around this problem is to rescale variables. Assuming the fan grows self-similarly and using the definition of the volume ratio (Eq. 4.9), we define a similarity variable

$$R=\left(\frac{6Q_{s0}}{(1-\lambda)\pi S_h\mathcal{V}}\right)^{1/3}t^{1/3}. \tag{4.12}$$

Accordingly, we define a dimensionless radius

$$X = \frac{r}{R}, \tag{4.13}$$

which varies between 0 and 1. We also define a dimensionless elevation

$$H(X) = \frac{h(r,t)}{S_h R}, \tag{4.14}$$

and a dimensionless sediment discharge

$$\chi(X) = \frac{Q_s(r,t)}{Q_s^*}. \tag{4.15}$$

Injecting these news variables into the mass-balance and the sediment-deposition equations (Eqs. 4.10 and 4.11), we obtain two ordinary differential equations

$$\chi' = 2X\mathcal{P}(XH' - H), \tag{4.16}$$

where $\mathcal{P} = \dfrac{Q_{s0}}{Q_s^* \mathcal{V}}$, and

$$H' = -(\chi + 1)^{1/3}. \tag{4.17}$$

These differential equation describe the radial evolution of the dimensionless sediment flux χ (Eq. 4.16), and the dimensionless fan elevation H (Eq. 4.17). The three boundary conditions become, at the fan apex $\chi(0) = \dfrac{Q_{s0}}{Q_s^*}$, and at the fan toe $\chi(1) = 0$ and $H(1) = 0$.

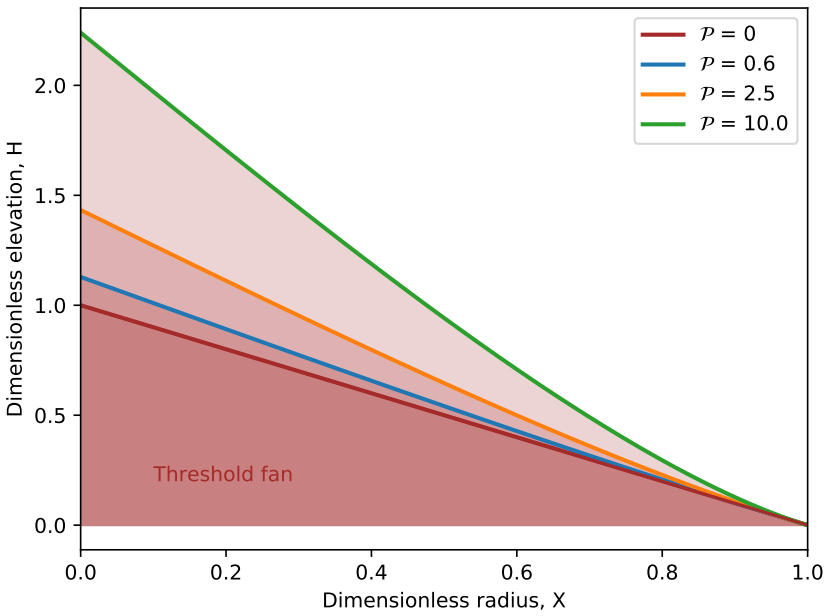

Figure 4.5: Numerical fan profile with different values of $\mathcal{P}$.

All the parameters that influence the fan profile are included into one parameter $\mathcal{P}$. Indeed, the influence of the fluid discharge, the fan aperture angle, and the grain size and density are

included into the volume ratio $\mathcal{V}$. The grain size and density also control the characteristic sediment discharge Q_s^* and finally, $\mathcal{P}$ is proportional to the sediment discharge injected at the fan apex Q_{s0}.

We numerically solve Eqs. (4.16) and (4.17), using the python libraries: *scipy.integrate.ode*. This libraries allows to solve an equation system where we impose the boundary conditions and the integrating step. By definition, we only know the boundary conditions at the fan toe, $\chi(1) = 0$ and $H(1) = 0$. Consequently, we integrate the two ODE from X = 1 to X = 0 using a negative step. The integration gives the spatial evolution of χ and H. To study the influence of the $\mathcal{P}$ parameter on the fan profile, we repeat the integration for four specific values of $\mathcal{P}$, .

These theoretical fan profiles are represented in Fig. (4.5). Similar to our experimental profiles, we find that when the sediment discharge increases, the slope increases. On these theoretical profiles, particularly the one of the highest value of $\mathcal{P}$ (green profile in Fig. 4.5), we can observe the concavity caused by sediment deposition. We also notice that, at the fan toe, the profiles merge and the local slope reaches the threshold slope S_h.

Equations (4.16) and (4.17) cannot be solved analytically. We can, however, investigate two asymptotic regimes: when the sediment discharge vanishes and when the sediment discharge tends toward infinity. Equation (4.17) is non-linear. To solve it, we need to linearize it. At very low sediment discharge we propose that

$$\chi = \xi\chi, \tag{4.18}$$

where $\xi\chi \ll 1$. Combining Eqs. (4.17) and (4.18), we only keep the first order terms to obtain the linearized equation

$$H' = -1. \tag{4.19}$$

Now, it is possible to solve Eqs. (4.16) and (4.19) using the boundary conditions. We finally obtain that when the sediment discharge vanishes:

$$\mathcal{P} = \frac{Q_{s0}}{Q_s^*} \quad \rightarrow \quad \mathcal{V} = 1. \tag{4.20}$$

As expected, when the sediment discharge vanishes, the volume of the fan is the volume of a threshold fan.

When the sediment discharge tends toward infinity, we cannot linearize Eq. (4.17). To find the asymptotic solution, we redefine χ and H such as:

$$\begin{cases} \chi = \mathcal{P}^{\alpha}\,\tilde{\chi} \\ \\ H = \mathcal{P}^{\beta}\,\tilde{H}, \end{cases} \tag{4.21}$$

where the exponents α and β are to be determined. Injecting these news variables into Eqs. (4.16) and (4.17), we find

$$\begin{cases} \mathcal{P}^{\alpha}\,\tilde{\chi}' = 2\,X\,\mathcal{P}^{\beta+1}(X\tilde{H}' - \tilde{H}), \\ \\ \mathcal{P}^{\beta}\,\tilde{H}' = -(\tilde{\chi}\,\mathcal{P}^{\alpha} + 1)^{1/3}. \end{cases} \tag{4.22}$$

When the sediment discharge injected as the inlet is high, $\tilde{\chi}\,\mathcal{P}^{\alpha} \gg 1$, we can now determine the value of the two exponents α and β,

$$\begin{cases} \alpha = \beta + 1, \\ \beta = \dfrac{\alpha}{3}. \end{cases} \tag{4.23}$$

We obtain $\alpha = 3/2$ and $\beta = 1/2$. Now, Eqs. (4.16) and (4.17) read

$$\begin{cases} \mathcal{P}^{1/2}\,\tilde{\chi}' = 2\,X\,\mathcal{P}^{3/2}(X\tilde{H}' - \tilde{H}), \\ \tilde{H}' = -\left(\tilde{\chi} + \dfrac{1}{\mathcal{P}^{3/2}}\right)^{1/3}, \end{cases} \tag{4.24}$$

with the boundary conditions $\tilde{\chi}(1) = 0$, $\tilde{H}(1) = 0$, and $\mathcal{P}^{3/2}\,\tilde{\chi}(0) = \dfrac{Q_{s0}}{Q_s^*}$.

The last of these boundary conditions implies that

$$\mathcal{V} = \tilde{\chi_0}^{3/2}\left(\frac{Q_{s0}}{Q_s^*}\right)^{1/3}. \tag{4.25}$$

This relation determines the evolution of the volume ratio, $\mathcal{V}$, when the sediment discharge is high. The evolution of the volume ratio, $\mathcal{V}$, is proportional to the dimensionless sediment discharge to the power one third. The prefactor of this power law, however, is unknown. The only way to estimate its value is to solve Eq. (4.24) numerically. Doing this we obtain $\tilde{\chi_0} \approx 0.47$.

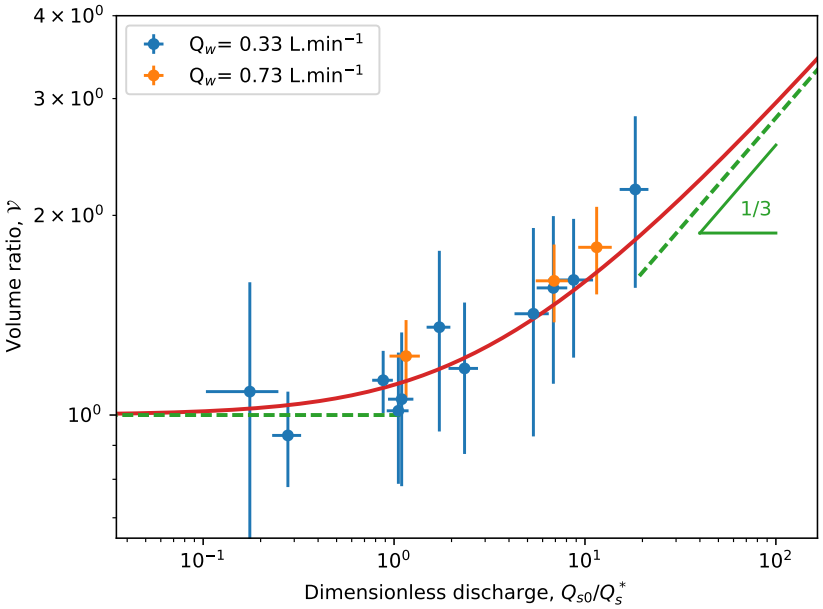

Figure 4.6: Evolution of the volume ratio as a function of the sediment injected. Blue and orange dots: experimental data (Q_w=0.33 L min^{-1} and Q_w=0.73 L min^{-1}). Red line: numerical solution showing two asymptotic solutions (green dashed lines). The coefficients are the ones of (Fig. 4.4).

Quantitatively, these two asymptotic solutions show that, when the sediment discharge is ten times lower than the characteristic sediment discharge, its influence on the fan slope is negligible. In contrast, when the sediment discharge is 100 times higher than the characteristic one, we can approximate the fan slope by the slope of its apex, despite the decrease of slope along the fan.

We now propose to compare our experimental measurements to the theoretical departure from threshold. To do so, we measure the experimental volume ratio of our fan. The volume of the fan, V, is measured using the DEM. We then divide these values by the volume of the corresponding threshold fan, V_h (Eq. 2.11). In this last equation, we assume that the slope is the threshold slope, S_h, reached for a given fluid discharge (0.33 or 0.73 $\mathrm{L\,min^{-1}}$). We calculate these slopes using (Eq. 2.8). In accordance with chapter 2 and Section. 4.2, we multiply the threshold slope by the prefactor estimated experimentally (Fig. 4.4). To estimate the volume of the threshold fan, we also need the radius of the fan, R, at the end of the experiment. We measure this radius using top-view pictures (Appendix C.1). Finally, we represent the experimental volume ratio as a function of the dimensionless sediment discharge for each experimental fans (Fig. 4.6). We use the characteristic sediment discharge estimated by the fit (Fig. 4.4). Figure (4.6) suggest that if we know the water discharge and sediment characteristics of a fan, we can estimate the sediment discharge based on its volume or its slope.

4.4 Conclusion

Using a simplified experimental set-up and a first-order theoretical analysis developed for alluvial rivers (Abramian et al., prep), we assess the influence of sediment transport on an alluvial fan profile. Not surprisingly, the fan slope increases with the sediment discharge. Based on 14 experiments involving different fluid and sediment discharges, we are able to determine the evolution of the sediment discharge along the fan radius (Eq. 4.11). This equation coupled with mass balance allows to determine the fan profile. The slope of the theoretical fan profiles is steeper near the apex than near the toe. At the toe, because we assume all the sediment is deposited onto the fan, the slope reaches the threshold slope, S_h. These results are in agreement with the results of Guerit et al. (2014) for a one-dimensional fan.

In principle, if a natural fan presents a concave-up profile, the measurement of its slope near the toe allows to determine the fluid discharge that built it (Eq. 2.8). If we know the characteristic sediment discharge, the ratio between the slope near the apex and the slope at the toe then gives a direct access to the sediment discharge (Eq. 4.7).

The asymptotic solution demonstrates that, when the sediment discharge, Q_s, is ten times lower than the characteristic sediment discharge, Q_s^*, its influence on the fan slope is negligible. It is then a reasonable assumption to consider that the fan is at the threshold of sediment motion. In this case, if we know the characteristic sediment discharge Q_s^*, we can infer the water discharge that build the fan by measuring the fan slope. It is also possible to estimate the maximum sediment flux that contributes to the fan building. In fact, the sediment flux should be lower than ten times the characteristic sediment discharge.

In this model, we can use the final shape of a fan, thank to its self-similar growth, to determine the fluxes that built it. Strictly speaking, this works only if the input parameters stay constant during the fan history. When forcing vary during the growth, the slope of the fan varies

accordingly. One way to investigate the variations of input parameters and the slope response to these variations is to study the fan stratigraphy.

Chapter 5

Varying forcing

Dans les trois chapitres précédents, nous avons étudié des cônes construits en maintenant constant les paramètres d'entrée (Q_s, Q_w et d_s). Dans ce cas, les cônes croissent de façon auto-similaire et acquièrent une forme d'équilibre contrôlée par ces paramètres. La pente est contrôlée, au premier ordre, par le débit d'eau et la taille des sédiments (Chapitre 2). Lorsque le système est composé de plusieurs taille de grain, on observe alors la formation de cônes imbriqués (Chapitre 3). Enfin, lorsque le flux de sédiment devient important, la pente d'un cône s'éloigne de la pente seuil (Chapitre 4). En se basant sur ces résultats, nous proposons maintenant d'étudier un cône dont les paramètres d'entrée varient au cours de sa formation. Nous proposons de reconstruire l'histoire des flux ayant alimentés le cône en observant la stratigraphie du dépôt.

Dans ce chapitre, nous explorons les conséquences des variations de deux paramètres d'entrée: le debit d'eau et la composition du mélange sédimentaire. Pour étudier l'influence d'une variation du débit d'eau, nous nous plaçons dans le cas le plus simple: un cône au seuil composé d'un sédiment uniforme. Nous considérons donc que le flux de sédiment est suffisamment faible pour ne pas modifier le profil du cône, et utilisons le formalisme présenté au chapitre 2 pour prédire le profil du cône. La deuxième partie se consacre à l'influence de la composition du mélange sédimentaire. Nous utilisons les résultats obtenus au chapitre 3 pour prédire la géométrie des dépôts. En résolvant les équations de conservation de la masse, nous montrons comment des variations du débit d'eau ou de la composition du mélange de sédiment peuvent s'enregistrer dans la stratigraphie du cône.

5.1 Variation of the water discharge

In the previous chapters, we have shown that the slope of the fan depends strongly on the water discharge. When the water discharge increases, the slope of the fan decreases. A remarkable consequence of an increase of the water discharge is incision near the apex of the fan (Weissmann et al., 2005; Guerit et al., 2011; Cesta and Ward, 2016). We propose to use mass balance to determine the conditions necessary to cause an incision.

5.1.1 Incision criterion

We consider a semi-conical fan at the threshold of sediment motion. Following the notations defined in Fig. (5.1), we define its volume,

$$V = \frac{\pi H_a R_f^2}{6}, \tag{5.1}$$

and its slope,

$$S_H = \frac{H_a}{R_f} \tag{5.2}$$

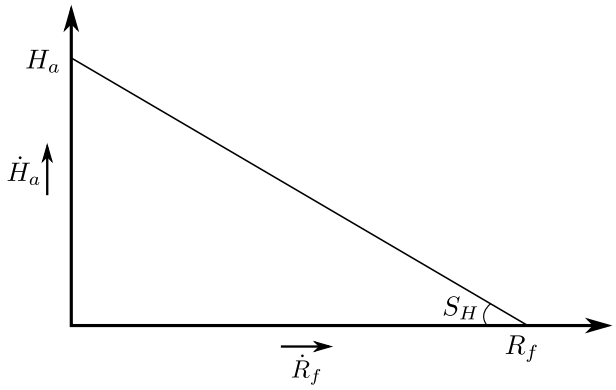

Figure 5.1: A fan at the threshold of sediment motion.

Using Eqs. (5.1) and (5.2), we find that the elevation of the fan, H_a, reads

$$H_a = \left(\frac{6 S_H^2 V}{\pi}\right)^{1/3}, \tag{5.3}$$

where V is the volume of the deposit. Because the fan is at the threshold of sediment motion, the sediment discharge impacts the growth rate of the fan only, whereas the water discharge controls its slope. To be closer to natural system, we chose to use the expression of the threshold slope determined for turbulent river,

$$S_H = \left(g\ \mu^3\ \left(\frac{\theta_c}{\mu}\ \frac{\rho_s - \rho}{\rho}\ d_s\right)^5\right)^{1/4} \sqrt{\frac{2^{3/2}\,\mathcal{K}(1/2)}{3\,C_f\,Q_w}}\,. \tag{5.4}$$

Where $\mathcal{K}(1/2) \approx 1.85$ is the elliptic integral of the first kind, and C_f is Chézy's coefficient of fluid

friction. The Chézy coefficient C_f depends on the bed roughness and the flow Reynolds number (Devauchelle et al., 2011; Gaurav et al., 2015; Métivier et al., 2017).

An incision occurs when the fan apex elevation, H_a, decreases. To investigate the variation of the water discharge necessary to generate incision, we derive Eq. (5.3) to obtain the time evolution of the fan apex elevation $\dot{H}_a$,

$$\frac{\dot{H}_a}{H_a} = \frac{1}{3}\left(2\frac{\dot{S}}{S} + \frac{\dot{V}}{V}\right). \tag{5.5}$$

Incision occurs when $\dot{H}_a < 0$, consequently the condition to generate incision reads,

$$2\frac{\dot{S}}{S} + \frac{\dot{V}}{V} < 0 \tag{5.6}$$

To express this condition as a function of the water discharge, we derive Eq. (5.4). In this equation, we assume that all the parameters, except the water discharge, are constant with time. We obtain

$$\frac{\dot{S}}{S} = -\frac{1}{2}\frac{\dot{Q}_w}{Q_w}. \tag{5.7}$$

Finally, using mass balance $\dot{V} = Q_s$, we infer the condition necessary to generate incision:

$$\frac{\dot{Q}_w}{Q_w}\frac{V}{Q_s} > 1. \tag{5.8}$$

Inequality (5.8) is a necessary condition for incision. Before testing numerically the validity of this criterion, we discuss its meaning.

The first remark concerning this criterion is that, for fans fed with the same water, Q_w, and sediment, Q_s, discharges, the bigger the fan is, the lower the variation of the water discharge has to be to generate incision. This observation can be expressed in terms of time. The volume of the fan corresponds to the integral of the sediment discharge over the period of the fan activity, P,

$$V = \int_0^P Q_s \, \mathrm{d}t \tag{5.9}$$

When the sediment discharge is constant, the volume of the fan equals the sediment discharge times the period of activity, $V = Q_s P$. In such conditions, the incision criterion read,

$$\frac{\dot{Q}_w}{Q_w} P > 1. \tag{5.10}$$

Consequently, if two fans are subjected to the same variation of water discharge, the older one (*i.e.* the biggest) may be incised whereas the younger (*i.e.* the smallest) is not.

Finally, if we impose an abrupt increase of the water discharge characterized by Fig. (5.2), the occurrence of an incision depends on P, T and ΔQ_w. Old fan and abrupt change make the incision easier, whereas a slower change makes incision less likely.

Another consequence of the dependance of this criterion on the fan volume, is that if a fan endures a cyclic water discharge variations of constant amplitude, the incision can occur only

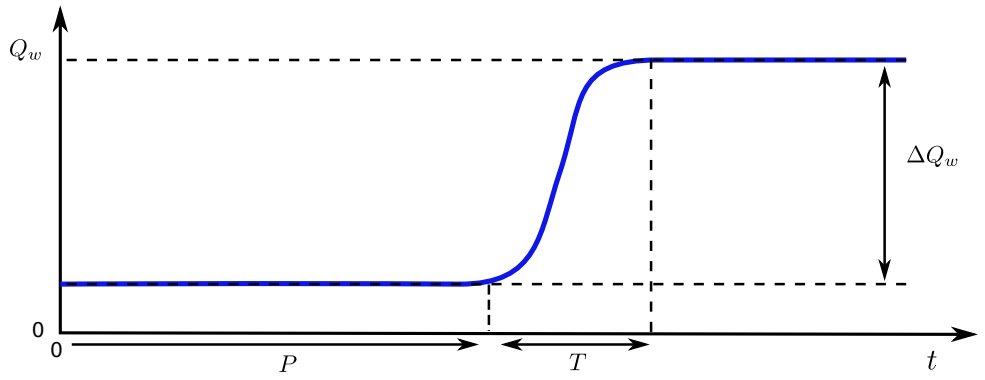

Figure 5.2: Schematic example of a varying water discharge. ΔQ_w is the difference between the minimum and the maximum water discharge, P the period of fan activity, and T the time over which the variation occurs.

after a few cycle, as the volume of the fan increases.

To illustrate this incision criterion, we now vary the water discharge during the fan construction and observe the resulting numerical fan stratigraphy. All equations are made dimensionless and we now use arbitrary units to represent the results of the model. In our model, we assume that the fan is axisymmetric. When the river begins to incise its fan, the axisymmetry is not maintained anymore and mass balance, as we have written it, breaks down. Thus, we stop the simulation when the incision starts.

5.1.2 Numerical simulation

We present two examples, in both cases we keep the sediment discharge constant and we impose an increase of the water discharge from 1 to 3 (Fig. 5.3). The only difference between these two example is the time, T, over which the variation occurs. When T is smaller (*i.e.* when the water discharge varies faster), we observe an incision (Fig. 5.3b).

For each value of the water discharge, we calculate the fan apex elevation H_a, using Eq. (5.3), and its radius R_f, using Eq. (5.2), and we represent the corresponding fan profile (Fig. 5.4). When the apex elevation becomes lower than the previous one, the river has incised the fan apex. Consequently we stop the simulation (Fig. 5.4b).

To test our incision criterion, we calculate its value at each time during the simulation (Eq. 5.8). We then represent its evolution (Fig. 5.5). For the example without incision this criterion does not exceed the value of one. This is in accordance with the stratigraphy of the fan where layers do not overlap (Fig. 5.4a).

In figure (5.4), we observe that the layers making up the fan stratigrahy get closer to each other, near the fan apex, when the water discharge increases. This is a signature of a slope decrease. To study the evolution of the slope when the water discharge decreases, we represent its evolution for both cases (Fig. 5.6).

In the first case, the slope of the fan decreases without generating an incision (Fig. 5.6a). At the end of the first simulation, the slope of the fan, is lower than the one at which incision occurs in the second simulation. When incision occurs, the slope of the fan is 0.078, this slope is reaches at T = 37. In the case without incision the slope of 0.078 is reached earlier, at T = 35.

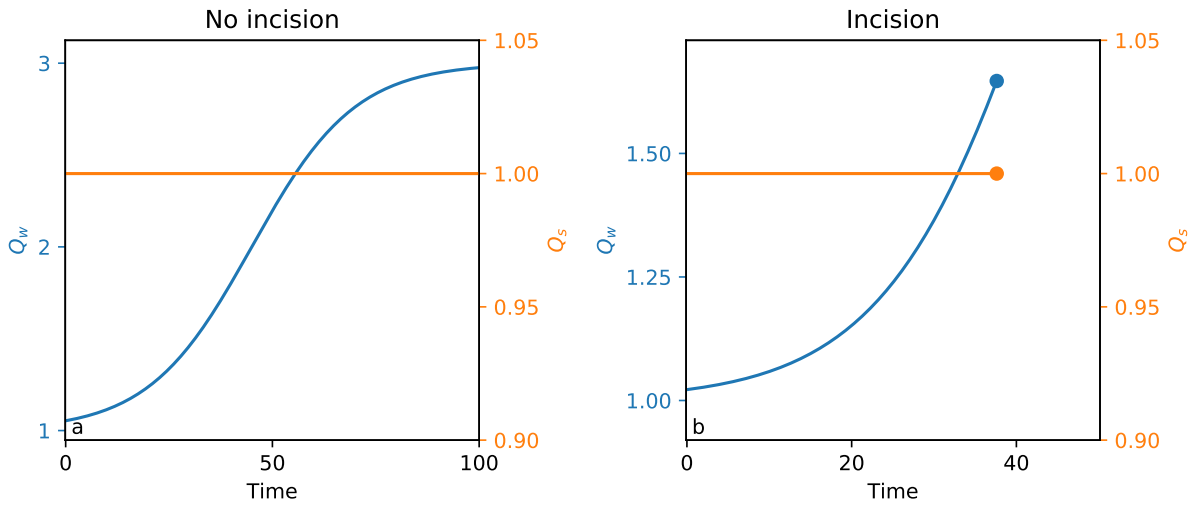

Figure 5.3: Evolution of the forcing in our simulations. a) The variation is too weak to induce incision. b) The change is fast enough to induce incision. Dots: time at which we stop the simulation.

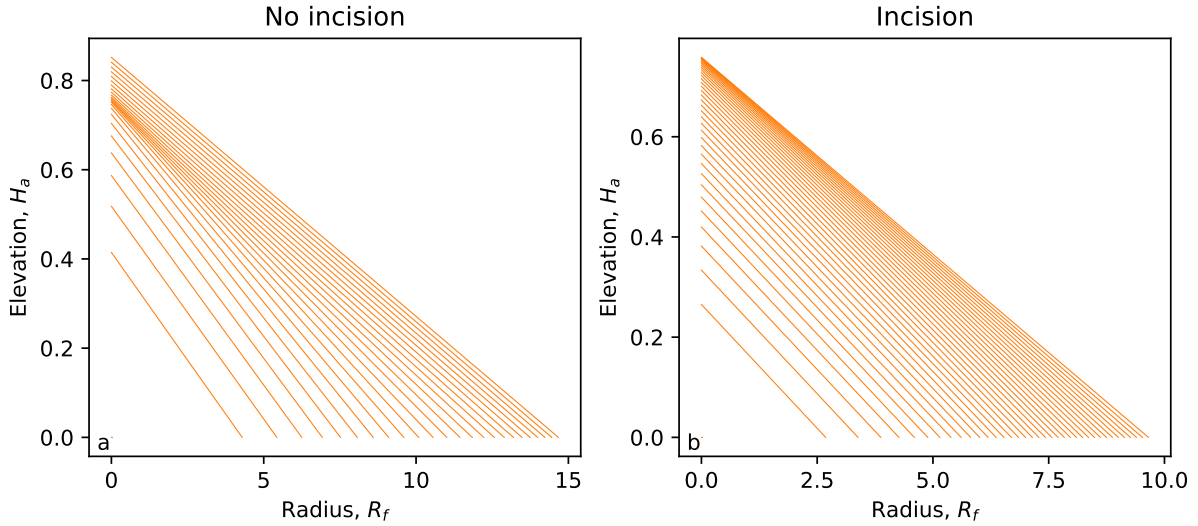

Figure 5.4: Evolution of the fan surface a) The river does not incise the fan. b) The river incises the fan.

Consequently, the fan is smaller and the change of the slope is not enough to generate incision. This observation confirms that a decrease of slope does not always generate incision but can be contemporaneous of an aggradation. The more important criterion to generate incision is the balance between the rate at which the slope decreases and the volume of the fan (*i.e.* its age).

We now propose to numerically investigate the influence of the variation of the sediment composition, following the result of chapter 3.

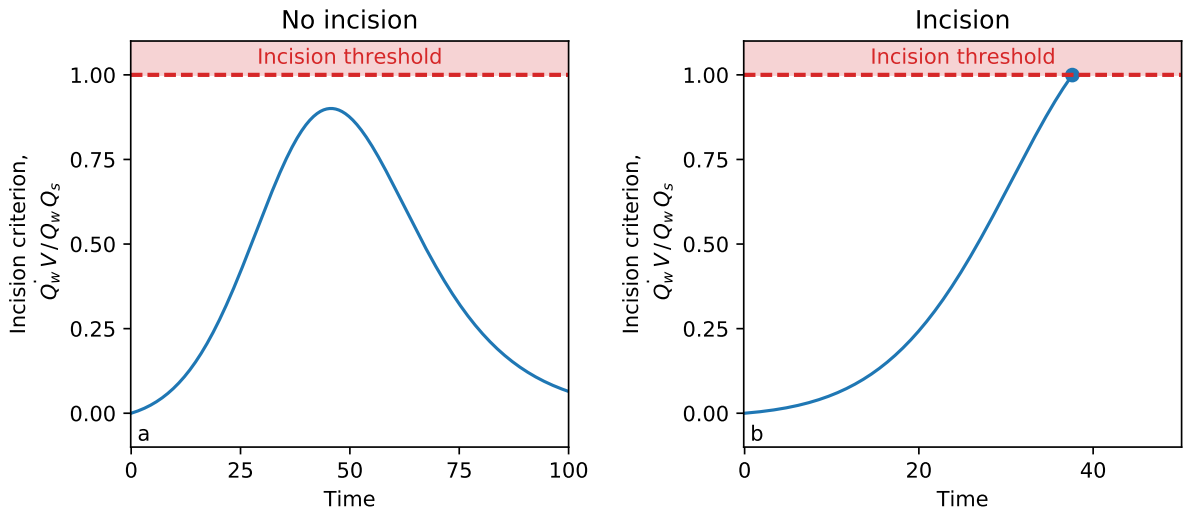

Figure 5.5: Evolution of the incision criterion. a) The criterion remains below one. b) The criterion reaches one.

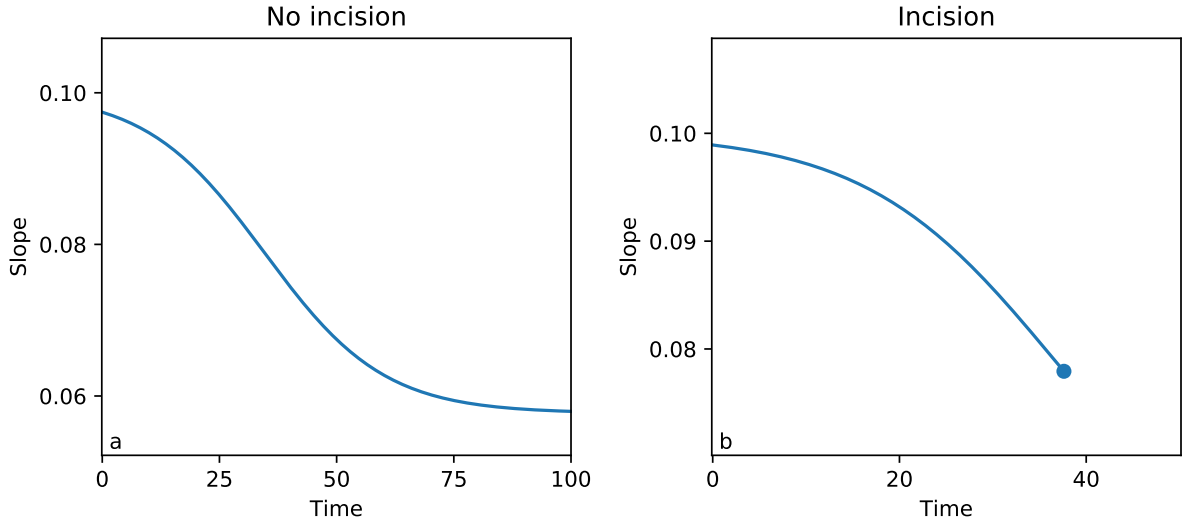

Figure 5.6: Evolution of the fan slope. a) The slope decreases slowly. b) The slope of the fan decreases faster and thus generates an incision.

5.2 Variation of the sediment-mixture composition

Variations of the sediment-mixture composition can result from changes in the climatic conditions or in the lithology of the drainage basin upstream of the fan. (Paola et al., 1992a; Marr et al., 2000). To investigate the influence of such changes, we consider the growth of a fan composed of bimodal sediment. We assume that the two types of sediment have different sizes, and therefore different mobilities. Consequently, the deposit is segregated on the fan morphology and stratigraphy (Paola et al., 1992b; Smith and Ferguson, 1996; Miller et al., 2014; Delorme et al., 2017). We propose to describe the stratigraphy of a fan subjected to variation of the sediment mixture composition.

5.2.1 Mass balance

We consider a fan composed of gravel (in orange) and sand (in green). The gravel deposit lies above the sandy one (Fig. 5.7). Two deposits thus form the fan, one composed of gravels and one composed of sands. Both deposits are characterized by a volume (V_g and V_s), a slope (S_g and S_s), an apex elevation (H_a and H_t), and a radius (R_t and R_f). To introduce our analysis, we first consider the evolution of a one dimensional fan. Then we will extend our results to a three dimensional radially symmetric fan. In both case, we consider that the slope of both deposits is constant and it is defined by the threshold of sediment motion.

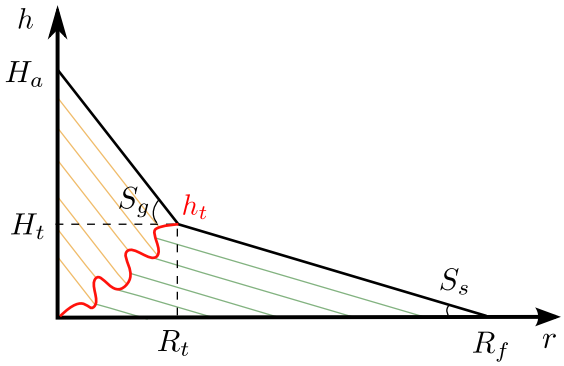

Figure 5.7: Schematic representation of the fan with definitions. Orange hatched area: gravel deposit. Green hatched area: sand deposit. Red line: gravel-sand transition.

We do not know *a priori*, the location of the transition between gravel and sand, defined by the function h_t. The volume of the gravel deposit, however, reads

$$V_g = \int_0^{R_t} (h - h_t)\, \mathrm{d}r, \tag{5.11}$$

where

$$h(r) = H_a - S_g r. \tag{5.12}$$

We can also define the gravel slope,

$$S_g = \frac{(H_a - H_t)}{R_t}. \tag{5.13}$$

Finally, mass balance reads,

$$\frac{dV_g}{dt} = Q_g, \tag{5.14}$$

where Q_g is the gravel flux. The derivative of Eq. (5.11) combined with Eqs. (5.12), (5.13) and (5.14), relates the amount of sediment injected into the fan to its growth,

$$S_g Q_g = \dot{H}_a (H_a - H_t). \tag{5.15}$$

Similarly, we define the volume of the sand deposited in the fan,

$$V_s = \int_0^{R_t} h_t \, \mathrm{d}r + \int_{R_t}^{R_f} h \, \mathrm{d}r, \tag{5.16}$$

where

$$h(r) = H_t - S_s(r - R_t). \tag{5.17}$$

We also define the slope of its surface,

$$S_s = \frac{H_t}{(R_f - R_t)}. \tag{5.18}$$

Using mass balance, its growth reads:

$$\frac{dV_s}{dt} = Q_s, \tag{5.19}$$

where Q_s is the sand discharge. Using Eqs. (5.16), (5.17), (5.18), and (5.19), we finally obtain the relation between the volume of sand injected in the experiment and the growth of the sand deposit,

$$S_s Q_s = \dot{H}_t H_t + \frac{S_s}{S_g}(\dot{H}_a - \dot{H}_t) H_t. \tag{5.20}$$

We can now define the evolution of the fan apex elevation and the evolution of the gravel-sand transition elevation,

$$\begin{cases} \dot{H}_a = \dfrac{S_g \, Q_g}{(H_a - H_t)} \\ \\ \dot{H}_t = \dfrac{\mathcal{S} \, S_s \, Q_s - \dot{H}_a \, H_t}{H_t \, (\mathcal{S} - 1)} \end{cases}, \tag{5.21}$$

where $\mathcal{S} = S_g/S_s$ is the ratio of the proximal over the distal slope. We first solve these equations is steady state.

5.2.2 Steady state

To solve the system of equation (5.21), we need to define two initial conditions, that is the initial geometry of the fan. The only parameters that matter for the fan growth are H_a and H_t. We choose their initial values arbitrarily, respecting one condition: the apex of the fan must be higher than the transition ($H_a > H_t$).

We find that our numerical fan, built with constant forcing, resembles the one of our bimodal laboratory fan (Figs. 3.8 and 5.8a). The two deposits are segregated and the transition line is approximately straight. However, at the beginning of the growth, the slope of the transition differs from the final one. This is caused by the initial conditions we impose. The evolution of fan apex and the location of the transition, show that after a some time, the stratigraphy reaches a self-similar regime. Regardless the initial conditions, when forcing are constant, the growth of the fan becomes self-similar.

This observation suggests a self-similar solution. To find it, we postulate that H_t is propor-

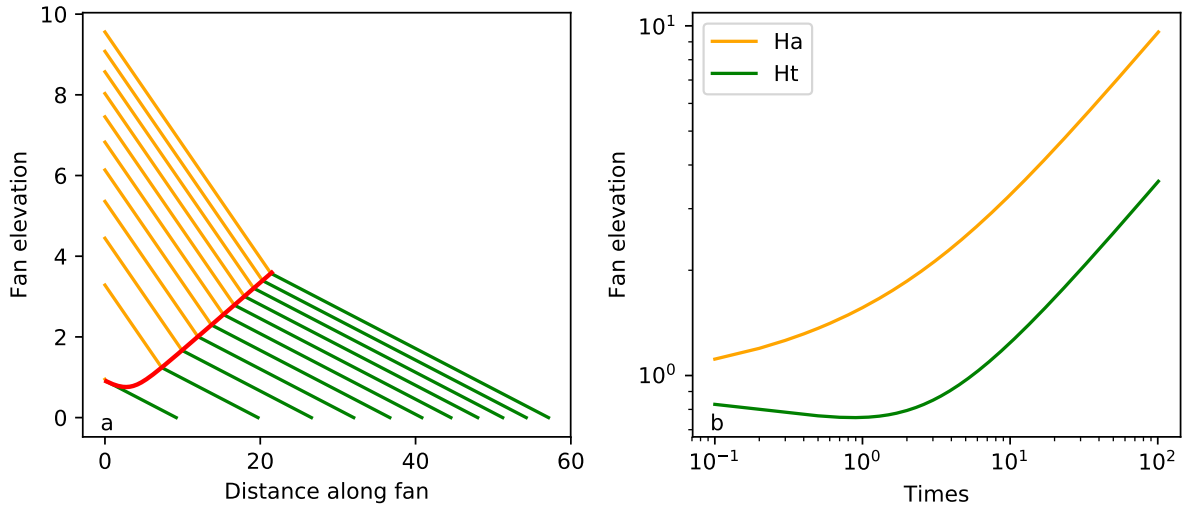

Figure 5.8: Numerical results. a) Stratigraphy of the deposit. Orange: gravel deposit. Green: sand deposit. Layers are separated by a constant amount of time. Red line: gravel-sand front. b) Evolution of the elevation of the fan apex and transition between gravel and sand during growth.

tional to H_a,

$$H_t = \alpha H_a, \tag{5.22}$$

where α is a dimensionless coefficient of proportionality. Using this definition, we can rewrite Eqs. (5.15) and (5.20),

$$\begin{cases} S_g Q_g = \dot{H}_a H_a (1-\alpha) \\ S_s Q_s = \dot{H}_a H_a \left(\alpha^2 + \dfrac{1}{\mathcal{S}} (\alpha - \alpha^2) \right) \end{cases} . \tag{5.23}$$

Using Eqs. (5.23), we can calculate α:

$$\alpha = \frac{-1 + \sqrt{1 + 4\,(\mathcal{S}-1)\,(\phi - \phi^2)}}{2\,\phi\,(\mathcal{S}-1)}, \tag{5.24}$$

where,

$$\phi = \frac{Q_g}{Q_g + Q_s}, \tag{5.25}$$

is the proportion of gravel in the sediment mixture. The self-similar solution can be analytically calculated, we find that the coefficient of proportionality α depends on the composition of the sediment mixture, ϕ, and the ratio of slopes $\mathcal{S}$.

To show that, regardless of initial conditions, the fan always evolves into a self-similar geometry, we represent the phase portrait of the fan dynamics, where solutions of Eqs. (5.21) are represented as lines for different initial values of H_a and H_t. Eqs. (5.21) have no physical solution when the initial value of H_t is larger than H_a (Fig. 5.9). We find that all trajectories in the phase space tend toward the line corresponding to self-similar growth, which slope is α.

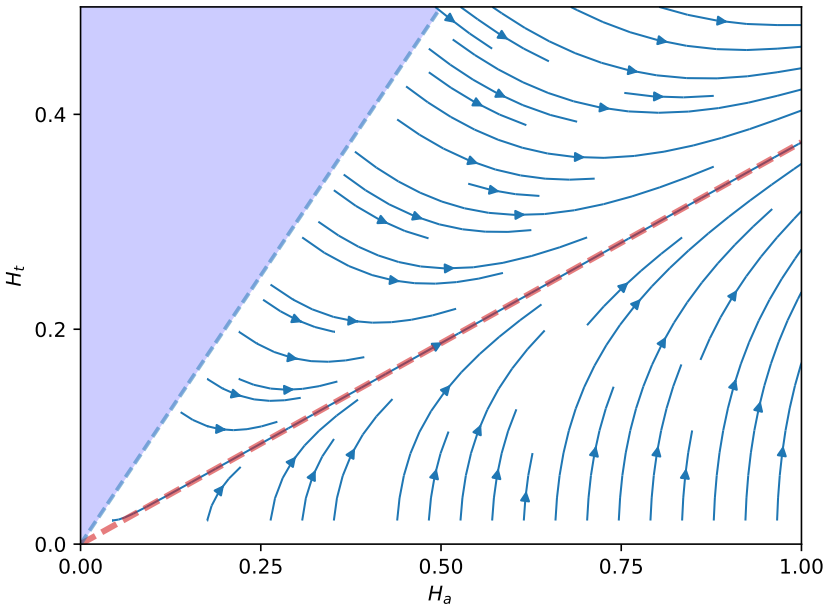

Figure 5.9: Phase portrait for equation (5.21). Red dashed line: self-similar solution (Eq. 5.24). Shaded area: Eqs. (5.21) have no solution.

For a natural fans, this result suggests that regardless of its history, when forcing are constant, the fan growth should become self-similar. We can now turn to the more interesting case, when the climatic, tectonic or lithological forcing vary, and ask whether these variations can be recorded in the fan's stratigraphy?

5.2.3 Influence of the forcing on the stratigraphy

To investigate this question, we extend this model to a radially symmetric fan, closer to natural system. In this geometry, the derivation of the evolution equation is slightly more difficult than for the one-dimensional fan. They are, however, very similar to their one-dimensional counterpart. We therefore present their final form only,

$$\begin{cases} Q_g = \dfrac{\pi}{2}\dot{H}_a R_t^2 \\ Q_s = \dfrac{\pi}{2}\left[\dot{H}_t(R_f^2 - R_t^2) + \dot{R}_t H_t R_f\right] \\ S_g = \dfrac{H_a - H_t}{R_t} \\ S_s = \dfrac{H_t}{R_f - R_t} \end{cases} . \tag{5.26}$$

Similarly, we can link the evolution of the fan apex elevation and the evolution of the gravel front to the input parameters,

$$\begin{cases} \dot{H}_a = \dfrac{2\,S_g^2\,Q_g}{\pi\,(H_a - H_t)^2} \\ \\ \dot{H}_t = \dfrac{\mathcal{S}^2\,S_s^2\,Q_s/\pi - \dot{H}_a\,\left(H_t^2\,(\mathcal{S}-1) + H_a\,H_t\right)}{H_t^2\,(\mathcal{S}^2 - 3\,\mathcal{S} + 1) + H_a\,H_t\,(2\,\mathcal{S} - 1)} \end{cases} . \tag{5.27}$$

In chapter 3, we showed that the location of the gravel-sand transition depends on the composition of the sediment mixture, ϕ. We therefore investigate the influence of a variation of this forcing on the fan stratigraphy.

To do this, we build a fan with a constant water discharge Q_w, and we vary the sediment-mixture composition ϕ. The slope of the gravel and sand deposits remains constant. We assume that the avulsion frequency is high enough to allow the variation to be record in the overall deposit.

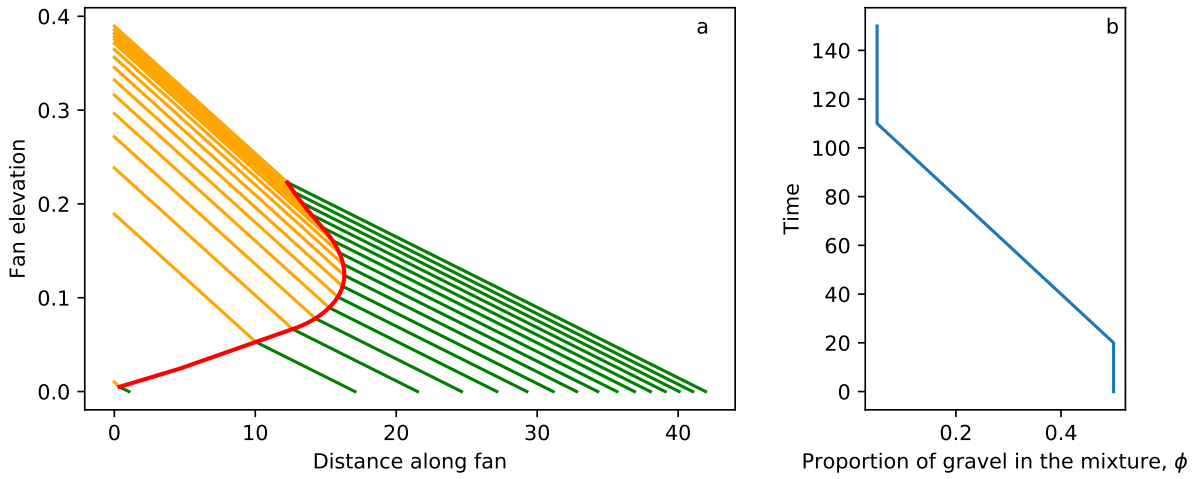

Figure 5.10: a) Stratigraphy of a bimodal fan, time increases by 10 between two lines. b) Evolution of he proportion of gravel, ϕ.

Our first numerical experiment consists in varying the sediment mixture from an equal proportion of sand and gravel to a mixture richer in sand. Hence ϕ varies from 0.5 to 0.05. Figure (5.10) represents the fan cross section and the evolution of the mixture during the fan's growth. At the beginning of the experiment, as well as at its end, we keep the mixture composition constant. During the transient, we decrease linearly the proportion of gravel. The resulting stratigraphy shows an aggradation and progradation of the gravel front following by an aggradtion and retrogradation of this front.

To the contrary, when the gravel proportion in the mixture increases, ϕ varies from 0.5 to 0.95, the slope of the transition changes signs, but we do not observe an alternate upstream and downstream migration of the gravel-sand transition (Fig. 5.11). The gravel front progrades during all the simulation and its elevation increases and then decreases without generate incision.

We now simulate a catastrophic event, such as a landslide, which brings coarse sediment into

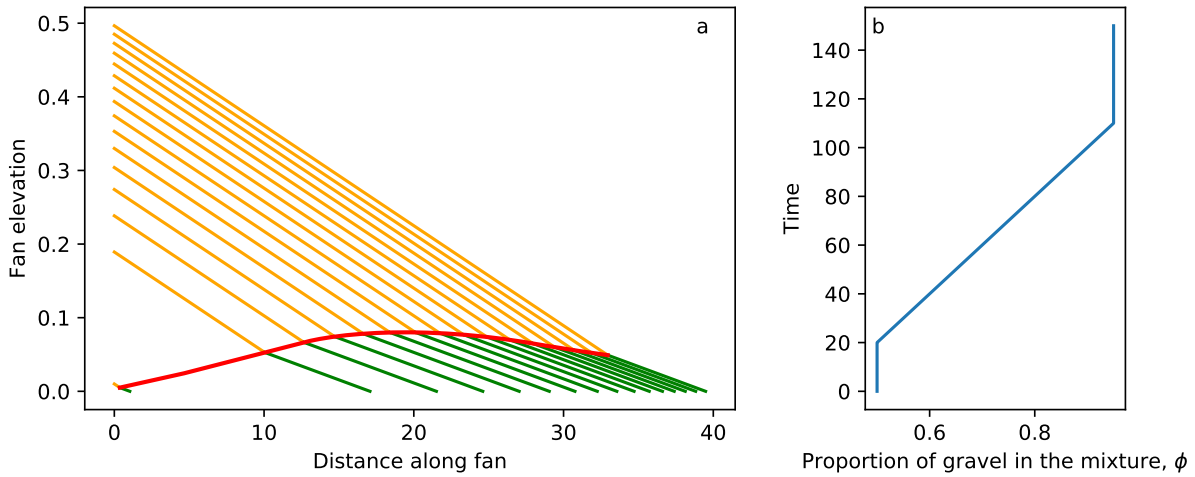

Figure 5.11: a) Stratigraphy of a bimodal fan, time increases by 10 between two lines. b) Evolution of the proportion of gravel, ϕ.

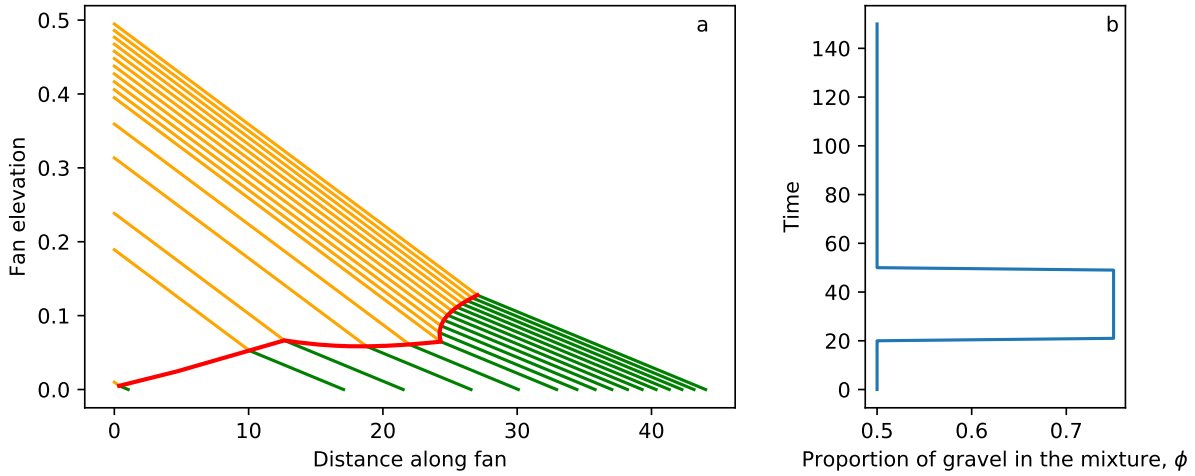

Figure 5.12: a) Stratigraphy of a bimodal fan, time increases by 10 between two lines. b) Proportion of gravel in the mixture increases suddenly and then goes back to its initial value.

the river during a brief period of time. To exemplify this we suddenly multiply by three the amount of gravel into the mixture, hence ϕ evolves from 0.5 to 0.75 to mimic a catastrophic input of gravel in the system. Then, after this catastrophic event, the mixture rapidly returns to its original value (Fig. 5.12). The resulting stratigraphy, shows a sharp decrease of the transition slope, during the event. When the mixture returns to its initial composition, the transition slope returns to its original value.

This simulation raises the question of time scale. Paola et al. (1992b) propose that the time over which a variation has to occur to be recorded in the stratigraphy, has to be higher than a characteristic time which depends on the size of the fan. This assumption should be tested numerically using a systematic study where we should vary the duration of the change and the size of the fan.

5.3 Conclusion

Using the results of chapters 2 and 3, we numerically investigated the evolution of an alluvial fan built under varying forcing. First, we explicit the condition necessary to generate an incision. A balance between the volume of the fan (*i.e.* its age) and the rate of the slope decrease determines the occurrence of incision. Second, we observe the stratigraphic record of a variation of the sediment composition. We notice that the signal in the stratigraphy depends on the forcing. With these simplified models, we propose some tools to better understand the relationships between paleo-variations of the water discharge or of the sediment composition and the inner structure of the alluvial fan.

For simplicity, we vary only one parameter at the same time: the water discharge or the sediment composition. However, in nature, an increase of the water discharge should cause an increase of the sediment discharge. In the case where we vary the water discharge, we assume that the sediment discharge does not influence the slope of the fan and we keep it constant even though the water discharge increases. Consequently, the slope of the fan is only determined by the threshold of sediment motion. On contrary, we propose that changes of the sediment mixture composition occur without change of the water discharge, therefore the slope of both deposit stay the same. To improve these models, we should consider the influence of the sediment discharge on the fan slope, using the results of chapter 4.

Finally, this chapter only presents preliminary results. We now have to perform systematic studies, to test the validity of these models and find their limitations. The record, in the fan stratigraphy, of changes of the forcing seems strongly dependent on the size of the alluvial fan (Paola et al., 1992b). The next step is therefore, to determine scaling laws that link the intensity of the change to the system dimension.

Chapter 6

Perspectives: exploring natural systems

Les résultats présentés dans les chapitres précédents sont obtenus dans des conditions simplifiées. Cependant, ils permettent de mettre en évidence les relations d'échelles entre la morphologie des cônes et les paramètres d'entrée. Dans nos expériences, l'écoulement est laminaire, ce qui n'est pas le cas des rivières naturelles où l'écoulement est turbulent. Néanmoins, dans le cadre expérimental, il semble que la morphologie des rivières laminaires et turbulentes est souvent contrôlée par les mêmes mécanismes physiques (Malverti et al., 2008; Chatanantavet et al., 2010). De plus, les cônes naturels ont une histoire plus complexe que les cônes expérimentaux. Ils sont généralement construit dans des zones tectoniquement actives et leur morphologie peut donc être modifiée par l'action des failles. Les flux qui les alimentent varient également au cours du temps. Enfin les sédiments qui les composent présentent le plus souvent une granulométrie étendue. Les résultats présentés précédemment ne peuvent donc pas être appliqués directement aux objets naturels. Cependant, ils peuvent servir à identifier les paramètres à étudier sur le terrain dans l'espoir de déterminer les paramètres d'entrée ayant permis la formation des cônes examinés.

Dans ce chapitre de perspectives, nous présentons donc des clés pour utiliser nos résultats expérimentaux, dans le cadre d'objets naturels. Dans un premier temps, nous nous intéressons à la pente de cônes alluviaux naturels. Nous montrons que l'étude du profil en long des cônes alluviaux permet de proposer une estimation des flux les ayant construits. Dans une seconde partie nous montrons, à partir de l'exemple des cônes du piedmont Nord du Tianshan, Chine, comment le critère d'incision permet d'étudier les variations de flux d'eau au cours de la formation d'un cône.

6.1 Fan slope

In the previous chapters we have investigated three kinds of alluvial fans characterized by a radial profile that depends on the external forcing:

- A linear profile, when the sediment discharge is low enough (Chapter 2).
- A segmented profile, when the sediment that feeds the fan is bimodal (Chapter 3).
- A concave profile, when the sediment discharge is significantly higher than the characteristic one (Chapter 4).

To investigate whether the knowledge gained from experiments can be used to extract information about the dynamics of natural fans, we now look at three natural examples. Two of them, the Bayingol and the Guertu fans, are located in the Tianshan, China. The third one, the Dog Canyon fan, is located at Oliver Lee Park, New Mexico, USA.

As these fans have been previously investigated, data sets are available (Poisson, 2002; Miller et al., 2014; Guerit et al., 2016; Métivier et al., 2016).

In their study of the Dog Canyon fan, Miller et al. (2014) characterize the channel geometry, the particle size and the elevation at different positions along the fan. The data is available through Figshare[1].

For the Chinese fans, Guerit et al. (2016) and Métivier et al. (2016) provide information about grain size and water discharge. To access the slope of these fan, we use Digital Elevation Models (ALOS-2, AW3D30[2]). These DEMs have a horizontal resolution of approximately 30 m (1 arcsec). Using these DEMs we extract the fan elevation along six radius. We then measure the local slope for each profile and average them. Using this procedure we finally compare the averaged slope of the fan, to our model.

Bayingol fan The first fan we study is located in the South-West part of the Bayanbulak Grassland (Tianshan, China). This intramontane sedimentary basin stands at an elevation of about 2500 m above sea level. The basin is surrounded by sloping meadows, enclosed in the Tianshan mountains, which provide water to the main river, the Kaidu River (Métivier et al., 2016).

The apex of the Bayingol Fan stands at approximately 2600 m above sea level and its toe at a mean elevation of 2400 m. The fan radius is about 20 km. Consequently, the slope of the fan is approximately 0.01 (Fig. 6.1). The Bayingol Fan is fed by a braided river, the Bayingol River, a tributary to the Kaidu River. Its bed is mostly composed of gravel, with a median grain size $d_{50} = 2.8$ cm. The sediment is quite uniform suggesting that the slope of the fan should not be segmented (Chapter 2). To investigate more precisely the slope of the fan, we extract six radial profiles from the DEM. We choose to extract profiles on the western part of the fan to avoid the active river (Fig. 6.1a).

We find that the radial profiles resemble each other, which meaning that the fan is radially symmetric (Fig. 6.1b). Consequently, the average slope of these six profiles is a good approximation of the overall fan slope. By representing this average slope as a function of the distance

[1] http://dx.doi.org/10.6084/m9.figshare.1197211
[2] http://www.eorc.jaxa.jp/ALOS/en/aw3d30/index.htm

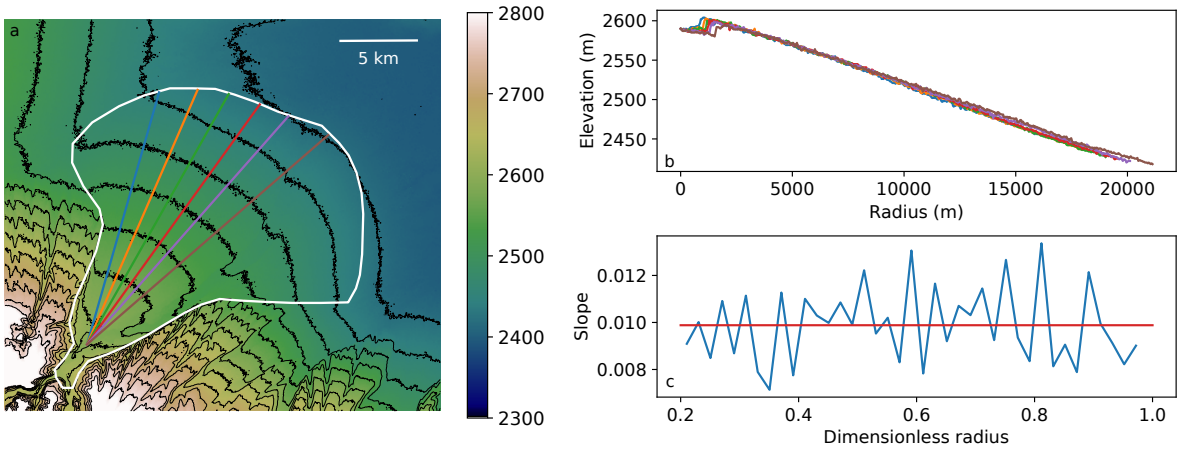

Figure 6.1: a) Digital elevation model of the Bayingol Fan. White line: fan boundaries, and colored lines: profile line. b) Radial profiles of the fan. c) Average slope of the fan as a function of the dimensionless distance from apex, red line: mean value.

from the fan apex, we notice that this slope is reasonably constant along the fan. The Bayingol fan slope is equal to 0.01 with a standard deviation of 20% (Fig. 6.1c).

Following our experimental results, a fan with a constant slope should be close to the threshold of sediment motion (Chapter 2). Accordingly, its slope depends only on the sediment characteristic and the water discharge. We now use the relation between the slope of a fan and the water discharge, in its turbulent version, to estimate the water discharge that built this fan,

$$S_H = \left(g\ \mu^3\ \left(\frac{\theta_c}{\mu}\ \frac{\rho_s - \rho}{\rho}\ d_s \right)^5 \right)^{1/4} \sqrt{\frac{2^{3/2}\,\mathcal{K}(1/2)}{3\,C_f\,Q_w}}\,. \tag{6.1}$$

Using this equation, with $\mathcal{K}(1/2) \approx 1.85$, $C_f \approx 0.1$, $\mu \approx 0.7$, $\theta_c \approx 0.04$, $\rho_s = 2650$ kg.m^{-3}, $\rho = 1000$ kg.m^{-3} and $d_s = d_{50} = 0.028$ m, we finally estimate a water discharge about 0.11 m^3 s^{-1}.

Métivier et al. (2016) have measured the water discharge, Q_w, in the individual threads that compose the Bayingol River. We compare these measurements to our estimate from the fan slope (Fig. 6.2). It corresponds to the lower discharges measured in the field. This suggests that the slope of a fan built by a braided river is controlled mostly by the threshold slope of the smaller threads, that is, the steeper ones.

However, this result has to be considered carefully, as the equation we use does not take the number of threads that compose the river into account. If the flow distributes itself evenly among the threads, though, we can approximate the total discharge by multiplying the water discharge, estimated using Eq. (6.1), by the number of thread that composed the river.

Dog Canyon Fan This fan is located at Oliver Lee State Park near Alamogordo, New Mexico. Dog Canyon drains the Sacramento Mountain range, which makes up the eastern boundary of the Tularosa Basin (Miller et al., 2014). This alluvial fan is an example of a bimodal alluvial fan, composed of gravel and sand. Miller et al. (2014) have collected the particle size along the fan (Fig. 6.3). The fan profile presents a relatively well-defined slope break located at the transition

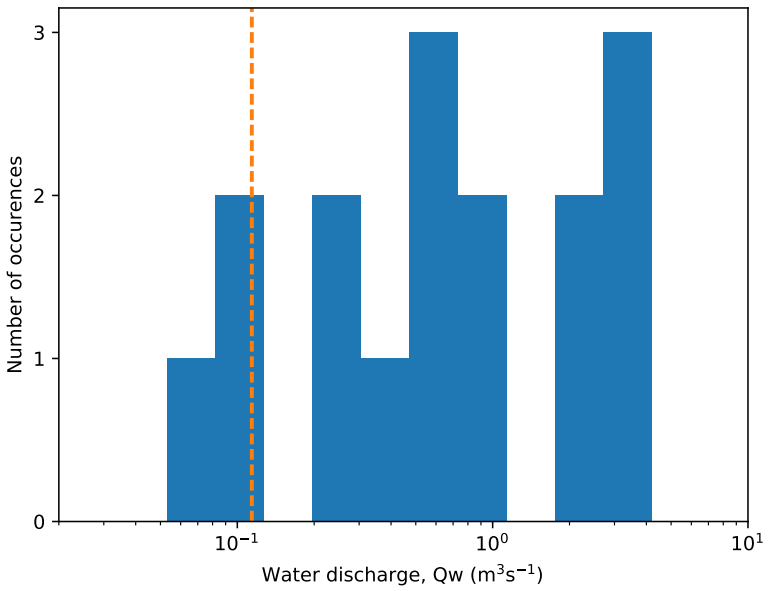

Figure 6.2: Distrubition of water discharge flowing through the threads that compose the Bayingol River. Orange line: water discharge estimated from the slope of the fan. *Data from Métivier et al. (2016).*

from a gravel-dominated bed to a sand-dominated bed. The slope upstream of the gravel-sand transition is constant and steeper than the one downstream of the transition. This structure is typical of bimodal fan (Delorme et al., 2017).

The fan profile is similar to the one we observe in our experiments (Chapter 3). Accordingly, we propose to use the method developed in chapter 3 to decipher the composition of the sediment mixture, $\phi = \dfrac{V_{\text{gravel}}}{V_{\text{sand}} + V_{\text{gravel}}}$, that built this fan. According to Eq. (6.2),

$$\phi = \frac{(1-\mathcal{S})\mathcal{R}^4 - \mathcal{S}\mathcal{R}^3 - \mathcal{R}^2}{(\mathcal{R}+1)\left((1-\mathcal{S})\mathcal{R}^3 - 1\right)}\,, \tag{6.2}$$

the composition of the sediment mixture can be calculated knowing only the relative position, $\mathcal{R} = R_{\text{gravel}}/R_{\text{fan}}$, of the transition and the ratio of slopes, $\mathcal{S} = S_{\text{gravel}}/S_{\text{sand}}$. To estimate this values we represent the evolution of the slope as a function of the distance from the fan apex, and we fit these data with a sigmoid to estimate the value of S_{sand}, S_{gravel}, and $\mathcal{R}$ (Fig. 6.4).

The two plateaus of the sigmoid give the value of the proximal and distal slopes, and the inflexion point the location of the transition (Fig. 6.4). We find that the upper slope is 0.04, the lower slope 0.01 and the relative location of the transition $\mathcal{R} = 0.49$. Introducing these values in Eq. (6.2), we obtain $\phi = 0.16$. We thus expect the initial mixture of sediment to be composed of 16% of gravel. Because we cannot access the fan stratigraphy, we cannot assure that the sediment composition did not change during the fan construction. From the fan surface, we can only obtain the composition of the sediment mixture involved in the more recent period of the fan activity. One way to estimate the evolution of ϕ during the fan growth could be to investigate the stratigraphy of the fan. In the startigraphy, the migration of the gravel front should result from variations of ϕ (Chapter 5).

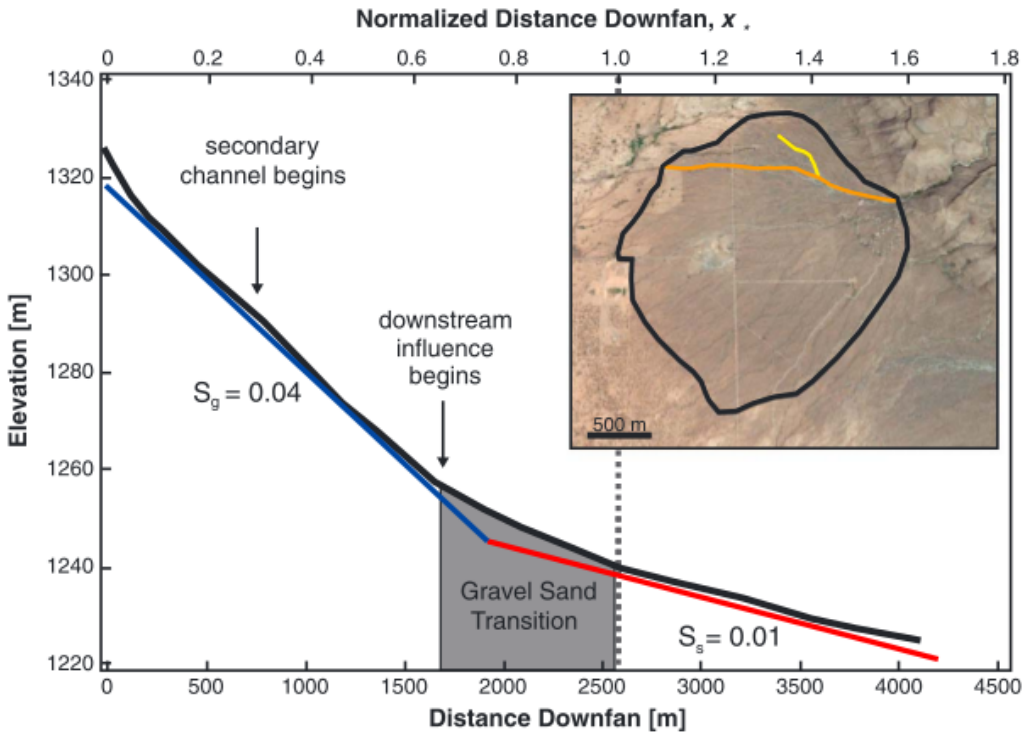

Figure 6.3: Profile of the Dog Canyon fan. Main channel profile from smoothed DGPS data. Inset shows aerial image of fan with the entire fan outlined in black, main channel denoted by orange line, and secondary channel denoted by yellow line. *From Miller et al. (2014).*

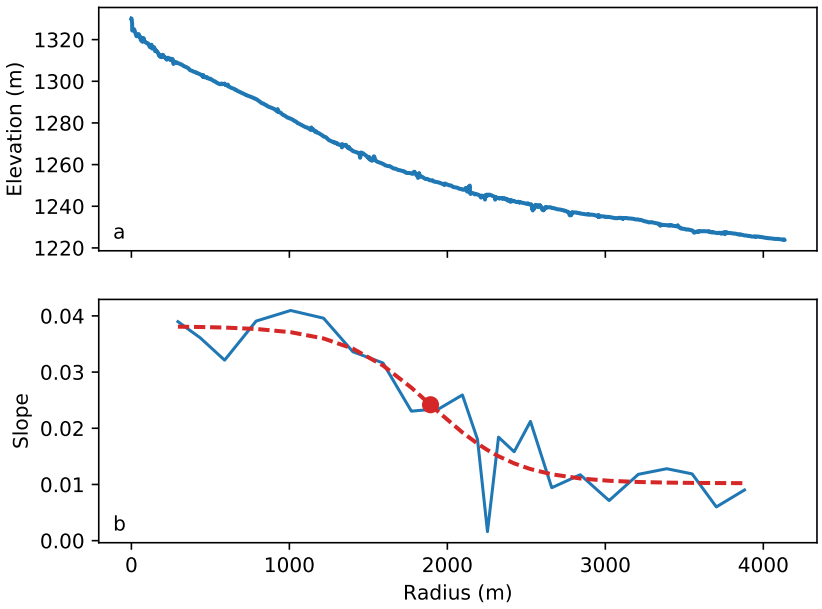

Figure 6.4: a) Radial profile of the Dog Canyon fan. b) Slope of the dog canyon fan as a function of the distance from the apex. Red line: sigmoid function fitted to the data. Red dot: the inflexion point of this fitted function. *Elevation data are from Miller et al. (2014) supplementary materials.*

Guertu fan This fan is located on the northern side of the Tianshan mountains. This range is separated from the Junggar Foreland Basin by series of Est-West-oriented folds (Fig. 6.5). A dozen of large rivers drain the northern side of this range. They originate from glaciers in the hinterland mountains and flow northwards to the Junggar Basin. These rivers have built and incised several alluvial fans (Fig. 6.5). Tectonic and climatic studies show that the cycle of fan aggradation-incision is climate-driven and linked to changes in water and sediment discharges (Poisson, 2002; Poisson and Avouac, 2004; Guerit et al., 2016). These fans are made up by conglomerates (Guérit, 2014). The Urumqi River (10 in Fig. 6.5), is the only river which sediment size and discharge are documented (Liu et al., 2011). The median grain size is about ≈ 20 mm. Because of the geomorphological similarity between these fans, we assume that the Urumqi River shared its characteristics with the other rivers of the range piedmont.

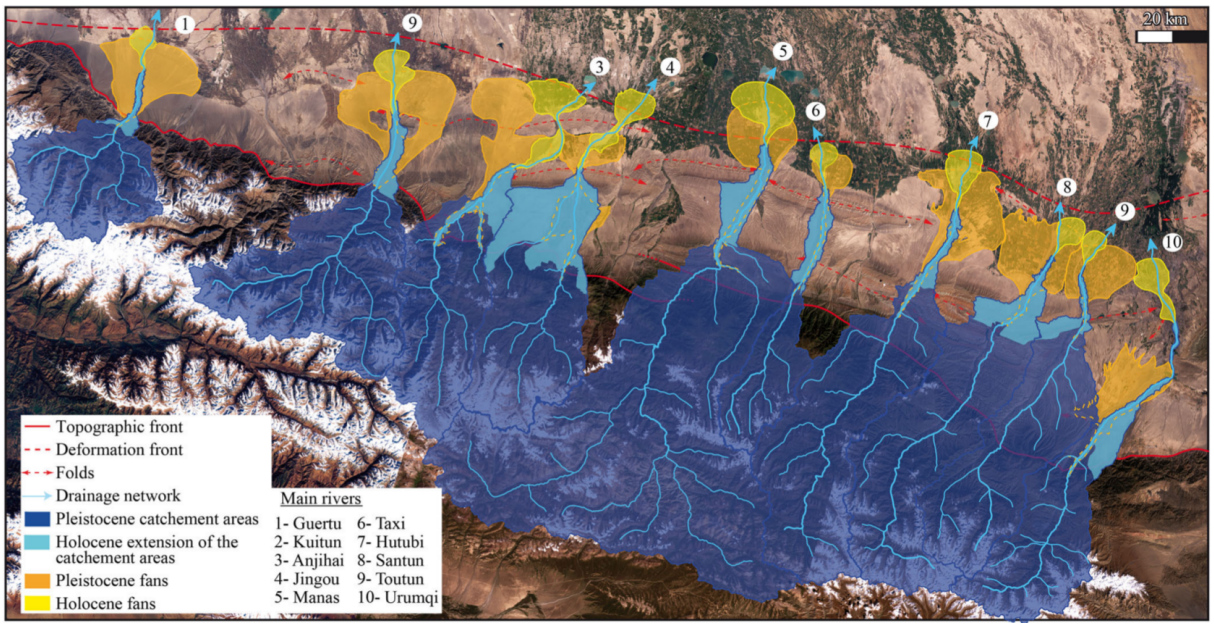

Figure 6.5: Present-day morpho-sedimentary map of the northern side of the Chinese Tianshan. *From Guerit et al. (2016).*

To investigate the influence of water and sediment discharges on the slope of a fan, we chose the western Guertu fan because it is likely to be less affected by fault activity. We thus analyze the Pleistocene fan fed by the Guertu River (1 in Fig. 6.5). This fan was active between 300 kyr and 12 kyr, and then incised during the last deglaciation (Poisson and Avouac, 2004). The Gertu fan apex stands at an elevation of approximately 1000 m above sea level, and its toe at an elevation of 400 m. The fan radius is approximately 25 km. Consequently, its mean slope is about 0.025.

To describe more accurately the shape of the fan radial profile, we extract six profiles on both sides of the entrenched river (Fig. 6.6a). These profiles are gently concave up (Fig. 6.6b). The three eastern profiles cross the entrenched river, so we use only, the three western ones to measure the averaged local slope. Figure (6.6c), shows that the fan slope decreases with the distance from the fan apex. On the proximal part of the fan, where r/R lies between 0.1 and 0.5, the slope is constant and about 0.027. Then the slope slowly decreases to reach a minimum

of about 0.017 at the fan toe, where r/R is between 0.9 and 1.

This slope variation resembles the one induced by a decreases of the sediment discharge along the fan (Stock et al., 2008). If this is true, following the results of chapter 4, the slope reaches at the fan toe should be the threshold slope, S_H, and the ratio of the slope at the fan apex over the slope at the fan toe, can be used to estimate the sediment discharge that fed the fan (Eq. 4.7). This equation was derived for fans fed by a laminar river and thus does not apply directly to natural fans. To adapt it to turbulent rivers, we use the relation, proposed by Seizilles de Mazancourt (2013), between the slope and the sediment discharge of a turbulent river:

$$S = S_H \sqrt{1 + \frac{3}{2^{3/2}\mathcal{K}(1/2)} \frac{Q_s}{Q_s^*}}. \tag{6.3}$$

To estimate the absolute sediment discharge, we need to measure the characteristic sediment discharge, Q_s^*, for this type of sediment. Despite this unknown parameter, we use the ratio of the slope at the fan apex over the slope at the fan toe to estimate, through Eq. (6.3), the relative sediment discharge, Q_s/Q_s^*. Assuming this relation holds, we finally obtain that the sediment discharge that fed this fan is approximately one and a half times the characteristic sediment discharge. To convert this value into an absolute discharge we need to measure the characteristic sediment discharge, Q_s^*, for this sediment.

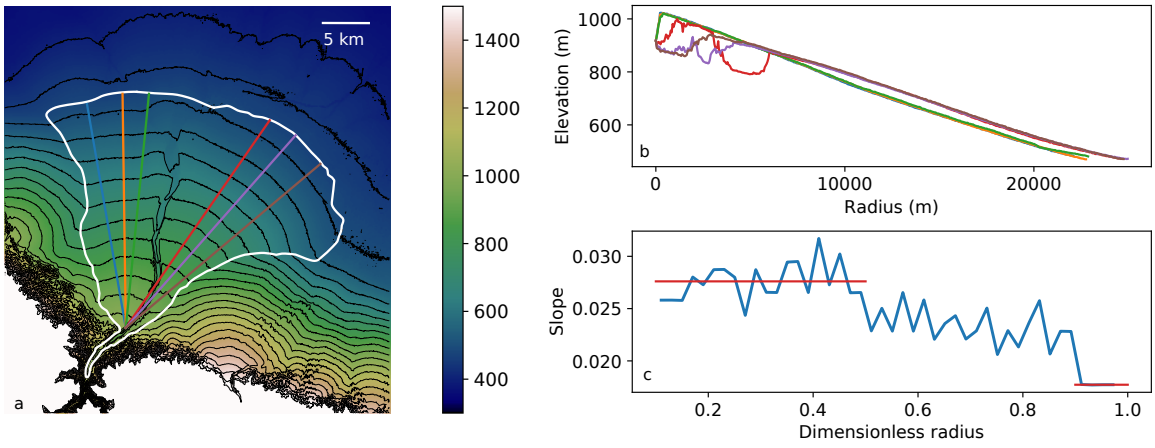

Figure 6.6: a) Digital elevation model of the Guertu fan. White line: fan boundaries; Colored lines: profile lines. b) Radial profiles of the fan. c) Average slope of the fan as a function of the dimensionless distance from apex. Red lines: mean slope near the apex and near the toe.

Using these three natural examples, we have shown that the scaling laws we find experimentally, can in principle be used to estimate the order of magnitude of the input parameters implied in the construction of natural fans. However, we have to consider these estimations carefully. First, we study only the fan surface. Therefore these estimations can only reflect the last stage of fan growth. To investigate the variation of the forcing during the fan's growth, we should explore the fan cross-section. Observed changes of slope in the fan stratigraphy could then be used to reconstruct the history of discharge variations. Second, we assume that the fans are built near the threshold of motion. Third, our scaling laws only apply to a fan fed by a single-thread

river. However, each thread of braided river seems to follow scaling laws that are similar to single-thread rivers (Gaurav et al., 2015). Consequently, as we discussed for the Bayingol fan, we need to characterize the morphology of the individual threads to improve our understanding of the fan dynamics.

One of the most remarkable effects of the increase of water discharge is the fan apex incision (Weissmann et al., 2005; Guerit et al., 2011; Cesta and Ward, 2016). Using the results of chapter 5, we now propose to estimate the rate of discharge variation that generated incision of the northern Tianshan Pleistocene fans.

6.2 Incision criterion

We can use the fans of the northern side of the Tianshan mountain to test our incision criterion (Chapter 5). Indeed, the Pleistocene fans have been incised during the last deglaciation, approximately 12 kyr ago (Poisson, 2002; Poisson and Avouac, 2004; Guerit et al., 2016). This incision induced the formation of smaller fans further downstream, the Holocene fans (Fig. 6.5). Guerit et al. (2016) have investigated these two series of fans. They have estimated the sediment discharge that built them, by reconstruction of their volume. They also measured the water discharge of the rivers that feed the Holocene fans (Table 6.1). Consequently, we can use these two data sets together with the definition of the incision criterion, to propose a lower bound for the rate of variation of the water discharge induced by the last deglaciation.

Table 6.1: Geomorphological characteristics and water and sediment fluxes of the northern Tianshan alluvial fans. Q_s is the total sediment flux, including suspended load and dissolved load. V is the volume of sediment in the fan.

River	Q_s Pleistocene $\times 10^5$ m^{3}yr^{-1}	V Pleistocene $\times 10^9$ m^3	Q_w Holocene $\times 10^8$ m^{3}yr^{-1}	$\dot{Q}_w$ m^{3}yr^{-2}
Kuitun	5.1	23.4	6.3	1169.2
Anjihai	2.5	11.5	3.1	571.5
Jingou	1.1	5.1	3.2	590.2
Manas	1.6	7.3	12.8	2381.1
Taxi	0.6	2.6	2.3	445.7
Hutubi	2.8	12.6	4.8	900.1
Sautun	1.4	6.6	3.1	563.3
Toutun	1.4	6.2	2.3	448.2
Ürümqi	0.9	4.2	2.4	431.1

We assume that all of these Pleistocene fans are incised at the same time 12 kyr ago during the last deglaciation. During the deglaciation, the glaciers melted inducing an increase of the water discharge. Accordingly, using a stream-erosion model, Poisson and Avouac (2004) estimated that during the early Holocene, when incision starts, the Kuitun River discharge was twice the present one. This evolution of water discharge follows the general climatic trend in central Asia. We assume that all the rivers that drain the northern Tianshan evolve similarly during the early Holocene. And we estimate that the fraction of the sediment load deposited on the fan is 17% of the total sediment flux. This value corresponds to the proportion of sediment transported as

bedload (Liu et al., 2008). Using Eq. (5.8) and the data of Guérit (2014), we calculate a minimum rate of variation for the water discharge during the early Holocene. To generate incision, this rate must be at least,

$$\dot{Q}_w = \frac{Q_s Q_w}{V}, \tag{6.4}$$

where Qs, Q_w and V are the sediment discharge, water discharge and volume of the fan just before incision, at the end of the Pleistocene. Following the result of Poisson and Avouac (2004), we estimate that the water discharge at this time is at least the actual one. Finally, we measure the minimum rate of water discharge variation, needed to generate incision, for each fan of the northern Tianshan, using Eq. (6.4) and Table (6.1). Assuming that all the fans were incised simultaneously, the regional minimum rate of water discharge variation, corresponds to the maximum value of $\dot{Q}_w$ calculated. We find that the regional minimum rate of the water discharge variation is approximately 2381.1 $\mathrm{m^3 yr^{-2}}$ (Table 6.1).

To compute the increase of water discharge necessary to incise these fans we need an estimate of the period, T, over which the perturbation occurred. Based on the paleo-levels of the Dzungar Lac, Poisson (2002) suggests that the degalciation causes an increase of the water discharge from 12 kyr to 6 kyr. Accordingly, we assume that the maximum value of T is 6 kyr. Assuming that the water discharge increase linearly during this period $\Delta Q_w = \dot{Q}_w T$, we find that an increase of about 1% of the water discharge is sufficient to generate incision. This low value may explain why all the fans of the northern Tianshan were incised simultaneously.

This example illustrates how the incision criterion could be used to determine the rate at which the water discharge has changed during a climatic event. This criterion is based on the assumption that the sediment discharge is small enough to neglect its influence on the fan slope. In chapter 4, we showed it is true only if the sediment discharge is ten times lower than the characteristic sediment discharge, Q_s^*. Otherwise, we would have to take into account its contribution to the fan slope.

6.3 Conclusion

In this chapter, we discuss the application of our experimental results to natural fans. We do this in order to highlight the parameters that we need to measure on the field to reconstruct the paleo-fluxes that built the fan.

Our analysis of three natural systems in China and the United States of America shows that the scaling laws, we determine experimentally, give a reasonable order of magnitude of the paleo-fluxes that built the fan. However, these estimation have to be considered carefully for several reasons. First, in natural system the flow is turbulent. We therefore need to adapt scaling laws that were derived for laminar flows. Second, natural fans form under varying conditions. Consequently, without access to the fan stratigraphy, we can only infer input parameters that contributed to the last stage of the fan growth. Third, our scaling laws are based on the assumption that the fan is built by a single-thread river. However, in the field a lot of fans are built by braided rivers.

In order to go further and estimate, with a higher accuracy, the parameters and fluxes that control the dynamics of natural fans we need to acquire specific field data. First, we should

characterize the sediment that enter the fan area to estimated the characteristic sediment flux Q_s^*. Second, we also need to quantify and characterize the number of threads that feed the fan to introduce them in our calculations. Finally, to reconstruct the evolution of the input parameters, surface measurements are not enough. We need to study the fan stratigraphy to describe the evolution of the slope and the position of the gravel front.

Conclusions et perspectives

Au cours de cette thèse nous avons montré que la morphologie des cônes alluviaux est contrôlée par les paramètres d'entrée qui les alimentent (Q_w, Q_s et d_s). À l'aide de modèles physiques simplifiés, nous avons montré l'importance de comprendre les phénomènes physiques agissant à l'échelle du grain et de la rivière pour étudier le comportement d'un cône alluvial (Fig. 1.12).

En utilisant ces modèles expérimentaux, nous avons déterminé les lois d'échelles qui relient les caractéristiques géométriques d'un cône alluvial aux paramètres d'entrée qui les alimentent. Expérimentalement, nous avons produit trois types de profils caractéristiques des cônes naturels : (1) un profil linéaire, (2) un profil segmenté et (3) un profil concave. Nous avons pu montrer que chaque type de profil se forme dans des conditions expérimentales particulières.

Dans le premier cas, lorsque le flux de sédiment est très faible, celui-ci n'influence pratiquement pas la pente du cône et le profil radial est linéaire. La pente du cône atteint une valeur seuil qui est contrôlée par le débit d'eau et la taille des sédiments. Pour un écoulement laminaire, la pente croît de façon inverse à la racine cubique du débit d'eau. Pour un écoulement turbulent, la morphologie de la rivière est déterminée par les mêmes mécanismes, seul l'exposant de la loi d'échelle est modifié, la pente du cône évolue proportionnellement à l'inverse de la racine carrée du débit d'eau.

Dans le second cas, l'injection d'un mélange sédimentaire dont les sédiments présentent des mobilités différentes produit un profil segmenté. Chaque segment de ce profil dépend du seuil de mise en mouvement du sédiment composant le lit de la rivière. Nous montrons qu'il est possible, en étudiant la géométrie du dépôt, de reconstruire le mélange sédimentaire ayant conduit à la construction d'un profil segmenté.

Enfin, dans le troisième cas, lorsque le flux de sédiment injecté à l'apex du cône devient important, la pente du cône s'éloigne de sa valeur seuil proportionnellement à $(1 + Q_s/Q_s^*)^{1/3}$. Nous avons pu mettre en évidence que le flux de sédiment, Q_s, était cependant négligeable si sa valeur était dix fois inférieure au flux de sédiment caractéristique, Q_s^*. La valeur de ce flux de sédiment caractéristique dépend de la taille des sédiments ainsi que de leur longueur de diffusion. Ce flux peut être mesuré expérimentalement en suivant la trajectoire des grains ou alors estimé en ajustant la loi de transport à l'échelle de la rivière, Eq. (4.11), sur les données expérimentales.

Ces expériences nous ont permis d'identifier les mécanismes physiques qui contrôlent la pente des cônes alluviaux. Toutefois, ces expériences sont réalisées dans un contexte simplifié et s'appuient sur des approximations. Leur application directe aux objets naturels n'est donc pas immédiate.

La première simplification est l'utilisation d'un fluide visqueux pour obtenir un écoulement laminaire. Lorsque l'écoulement est turbulent, les mécanismes qui déterminent la géométrie de la

rivière restent valables. Seul le profil de vitesse est modifié, celui-ci fait intervenir un coefficient de frottement, C_f, qui dépend de la rugosité du fond ainsi que de la vitesse et de la taille de l'écoulement. En intégrant ce profil de vitesse turbulent sur la largeur de la rivière il est donc possible de retrouver les équations de régime pour un écoulement turbulent.

En outre, dans la nature, de nombreux paramètres, que nous n'avons pas pris en compte, peuvent influencer la dynamique d'un cône :

- l'activité tectonique, qui peut modifier la pente de la rivière,
- la distribution étendue de taille des sédiments transportés,
- la végétation.

Enfin, toutes nos expériences ont été réalisées en maintenant constant les paramètres d'entrée alimentant le cône. De la sorte, le cône croît de façon auto-similaire. Or ce n'est souvent pas le cas dans la nature où les cônes se construisent sur des échelles de temps qui peuvent aller jusqu'à la centaine de milliers d'années.

Pour étudier l'influence de l'évolution de ces forçages pendant de la construction du cône nous avons donc développé un modèle fondé sur la conservation de la masse et l'hypothèse du seuil de transport. Celui-ci nous a permis d'observer la forme des enregistrements sédimentaires dans la stratigraphie du cône, en lien avec des variations de forçages. De nouveau, ce modèle est simplifié : nous ne faisons varier qu'un seul forçage à la fois et négligeons l'influence du flux de sédiment sur la pente du cône. Celle-ci est donc déterminée uniquement par la taille des sédiments et le débit d'eau. Dans la nature, une augmentation du débit d'eau génère souvent une augmentation du flux de sédiment. Il serait donc intéressant de compléter ce modèle en incluant l'influence du flux de sédiment sur la pente du cône, étudiée au chapitre 4.

Enfin, dans un dernier chapitre, nous avons montré comment les résultats obtenus expérimentalement pourraient être utilisés pour étudier les cônes naturels. Évidemment, la complexité des objets naturels nécessite d'adapter nos résultats. Nous avons cependant mis en évidence l'importance de caractériser les sédiments qui composent le cône, afin de quantifier les lois de transport qui contrôlent leur mise en mouvement. Les rivières qui forment les cônes alluviaux sont souvent des écoulements en tresse, or nos résultats expérimentaux, à l'exception du chapitre 3, reposent sur l'hypothèse d'un cône alimenté par un chenal unique. Pour reconstruire les flux à partir de la pente du cône, il est donc nécessaire de décrire avec précision le nombre et les caractéristiques morphologiques des chenaux qui composent la rivière alimentant le cône. Enfin, du fait de la longue période de temps sur laquelle le cône se construit, celui-ci peut enregistrer les variations des flux dans sa stratigraphie. Pour reconstruire l'évolution de ces flux il serait intéressant d'avoir accès à la stratigraphie du cône, soit à l'aide de tranchées naturelles (incision de la rivière) ou artificielles, soit en utilisant des techniques d'imagerie du sous-sol, qui permettraient d'étudier la géométrie des strates (pente et courbure).

Perspectives

Distribution continue de taille de grains

En s'appuyant sur les résultats du chapitre 3, nous pourrions sans doute extrapoler le comportement d'un cône alluvial composé de deux tailles de grains à un cône composé d'un distribution continue de taille de grains. Lorsque le cône est composé de deux types de sédiment de mobilité différentes, nous avons pu observer que les sédiments formant le dépôt étaient ségrégés. Les grains les plus mobiles sont déposés en aval tandis que les grains les moins mobiles se déposent à proximité de l'apex du cône.

En considérant que ce même mécanisme de ségrégation a lieu lorsque le mélange sédimentaire est composé de plus de deux types de sédiments, on peut imaginer que le cône formé présente un profil composé de plusieurs segments linéaires (Fig. 6.7). Chacun de ces segments étant associés à un type de sédiment, sa pente est contrôlée par le seuil de mise en mouvement des sédiments du lit de la rivière. En utilisant une représentation simplifié de la géométrie de ces cônes imbriqués, il serait alors possible à partir du profil du cône de reconstituer la distribution de sédiment ayant alimenté le cône. Enfin, en passant à la limite de dépôt infinitésimaux, nous devrions pouvoir représenter la formation d'un cône alluvial alimenté par une distribution continue de taille de grains.

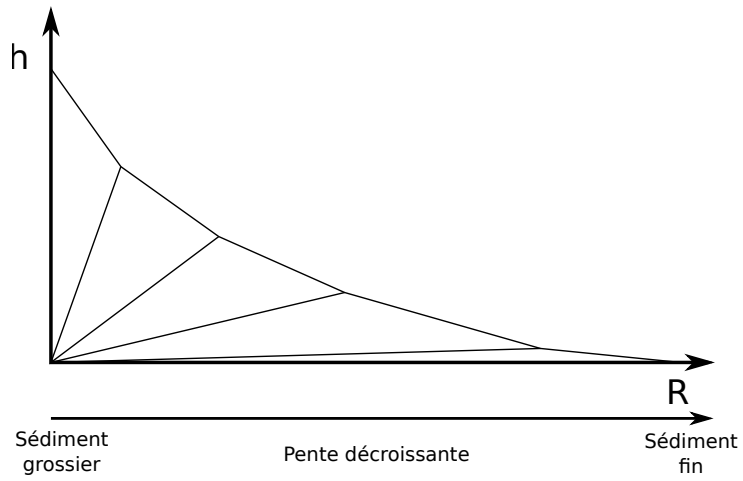

FIGURE 6.7 : Représentation schématique d'un cône alluvial composé de cinq catégories de sédiments, caractérisés par une mobilité croissante vers l'aval.

Ce mécanisme de ségrégation, tel que nous l'avons observé au chapitre 3, engendre aussi une ségrégation verticale. Dans le cas où la composition du mélange sédimentaire n'a pas varié au cours du temps, une coupe verticale du cône devrait nous permettre d'observer la présence des grains les plus fins à la base du cône.

Variation des forçages

Pour vérifier l'enregistrement dans la stratigraphie d'une variation des forçages, nous avons conçu un dispositif expérimental préliminaire à une dimension dans le cadre du stage de licence de Cécile Bidaut (Fig. 6.8). Ce dispositif nous permet d'avoir accès à la stratigraphie du cône au cours de

sa formation. Le cône est confiné dans un chenal en Plexiglass de 20 cm de haut, 1.5 m de long et 2.5 cm de large. Nous avons utilisé deux types de sédiments caractérisés par une mobilité et une couleur différente : des grains de corindon noir (d_s = 800 μm, ρ_s = 3900 kg m^{-3}) et des grains de plastique multicolore (d_s = 800 μm, ρ_s = 1500 kg m^{-3}). La différence de mobilité entre ces deux types de sédiments est déterminée par leur différence de densité. Le corindon, plus lourd, se dépose en premier. Nos expériences préliminaires, ont permis de vérifier que les dépôts sont ségrégés en fonction de la mobilité des grains.

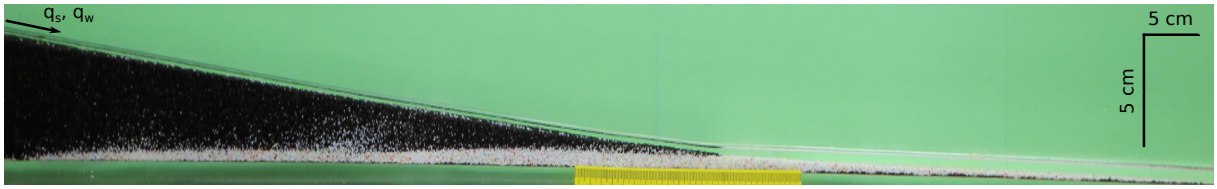

FIGURE 6.8 : Cône alluvial en 1D alimenté par deux types de sédiments. Exagération verticale ×2. *Photographie : Cécile Bidaut.*

Pour aller plus loin, ce dispositif pourra être utilisé en faisant varier les forçages. Grâce à un dispositif équipé de deux systèmes d'alimentation en sédiment, nous pouvons contrôler indépendamment la quantité de chaque type de sédiment injecté. Ainsi, nous pourrons à l'avenir imposer une variation de la composition du mélange, au cours de la formation du cône. Cela nous permettra de vérifier si la localisation du front de sédiment grossier dépend effectivement de cette composition.

Incision du cône

Nous avons proposé un critère d'incision qui indique pour quelle variation du débit d'eau une rivière incise l'apex de son cône (Chapitre 5.1). Ce critère pourrait être testé expérimentalement en utilisant le dispositif présenté dans les chapitres 2 et 4.

Pour en illustrer le principe, nous avons réalisé une expérience préliminaire au cours de laquelle nous maintenons un flux de sédiment constant, puis augmentons soudainement le flux d'eau (Fig. 6.9). Nous observons bien que cette brusque augmentation du débit d'eau provoque l'incision du cône et la formation d'un cône secondaire en aval (Fig. 6.9). Ces cônes expérimentaux sont similaires à ceux que l'on observe dans le piedmont nord du Tianshan. Le dispositif, tel qu'il est conçu actuellement, ne permet pas d'imposer une variation continue du débit d'eau. Cette limitation peut être résolue en installant le château d'eau sur une crémaillère reliée à un moteur. Un tel dispositif nous permettrait de contrôler avec précision l'augmentation du débit d'eau et ainsi de tester expérimentalement la validité de notre critère d'incision.

Cônes extra-terrestres

Nous avons montré dans le chapitre 6, que l'étude des profils des cônes naturels pouvait nous donner une indication de l'ordre de grandeur des flux les ayant construits. Or, on observe sur d'autres planètes des dépôts sédimentaires qui semblent avoir été mis en place par des écoulements liquides, en particulier sur Mars (Moore and Howard, 2005). Il semblerait donc que l'on puisse

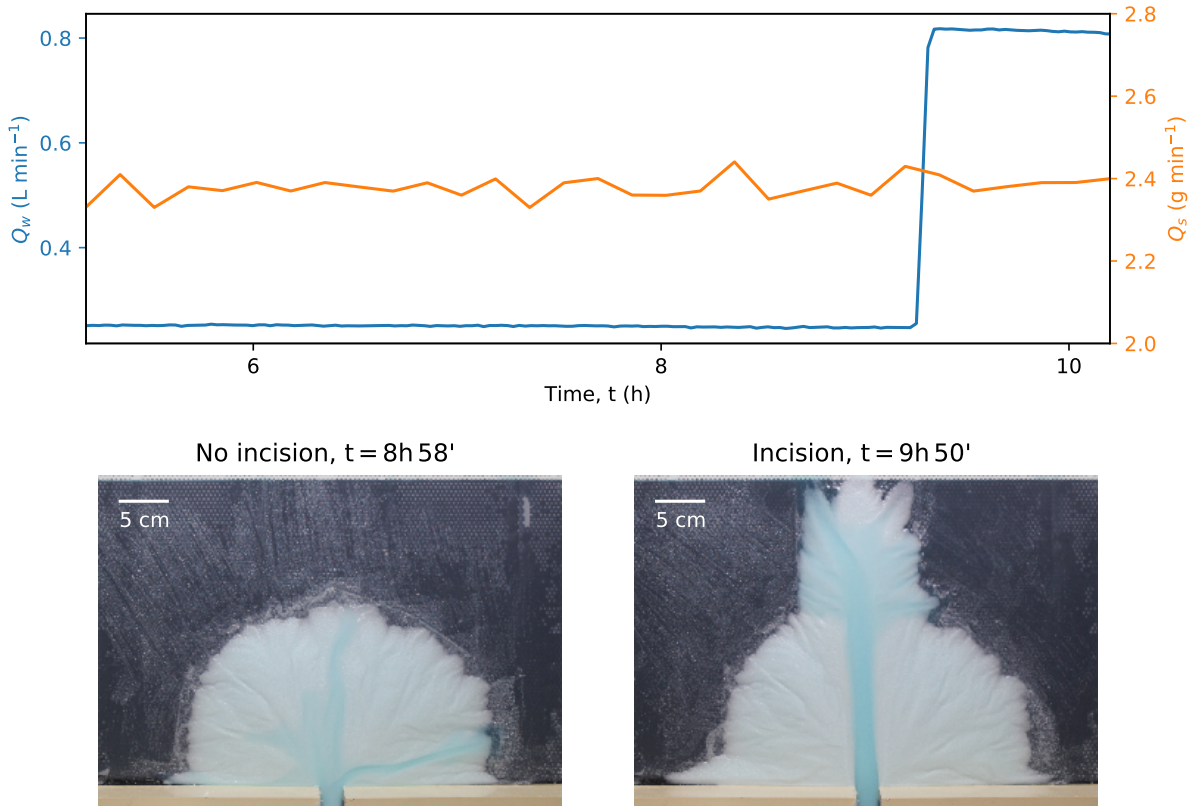

FIGURE 6.9 : Expérience préliminaire de construction d'un cône alluvial lorsque les paramètres d'entrée varient. En haut, évolution du débit d'eau (bleu) et de sédiment (orange). En bas, photographies du cône avant (gauche) et après (droite) l'augmentation du débit d'eau.

appliquer les résultats obtenus dans cette étude aux cônes martiens et proposer une estimation des conditions hydrologiques et des flux sédimentaires ayant permis leur formation.

Pour illustrer cette idée nous nous intéressons au Peace Vallis fan, situé au nord du cratère Gale (Williams et al., 2013; Palucis et al., 2014). Palucis et al. (2014) ont extrait des profils de ce cône à partir du DEM HCN afin d'en étudier le pente (Fig. 6.10). Nous proposons donc d'utiliser ces données pour interpréter la morphologie du cône à la lumière de nos résultats.

On observe que dans la partie supérieure du cône les trois profils sont confondus (Fig. 6.10B). Le dépôt est donc axisymétrique. En outre, ces profils sont similaires aux profils que l'on observe expérimentalement ou sur les cône terrestres. Il semble donc légitime d'utiliser la méthode présentée au chapitre 6 pour estimer les flux ayant permis la construction de ce cône. En représentant la pente du cône en fonction de la distance à l'apex, Palucis et al. (2014) montrent que la pente du cône diminue progressivement de 3% à l'apex, jusqu'à 1%, à la transition entre le cône supérieur et le cône inférieur (Fig. 6.10C). Une diminue de la pente peut être engendrée soit par une diminution de la taille des sédiments vers l'aval, soit par une diminution du flux sédimentaire. Concernant la taille des sédiments nous utilisons les estimations effectuées par Williams et al. (2013) et Palucis et al. (2014). En analysant les images acquises par le *MSL Curiosity rover*, qui s'est posé au pied du cône (Fig. 6.10A), Williams et al. (2013) estiment que la taille des sédiments varie entre 2 et 40 mm. Le modèle hydraulique s'appuyant sur la géométrie des chenaux utilisé

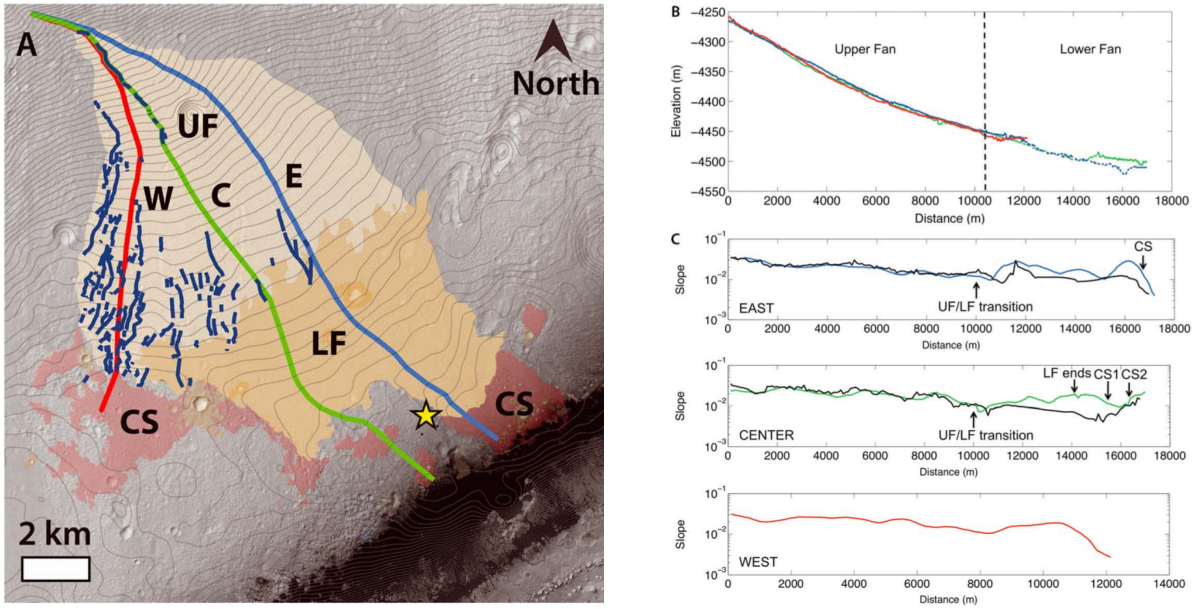

FIGURE 6.10 : (A) Le Peace Vallis fan, sur lequel on observe les lignes de niveau (marron). Les lignes colorées représentent l'emplacement des trois profils longitudinaux, profil ouest en rouge (W), profil central en vert (C) et profil est en bleu (E). UF, représente le cône supérieur, LF le cône inférieur et CS la surface cratérisée. L'étoile jaune représente la zone d'atterrissage du *MSL Curiosity rover*. (B) Profils du cône le long des trois segments représentés sur la figure A (extrait à partir du DEM HCN). La ligne pointillée marque la limite entre les cône supérieur et inférieur. (C) Pente moyenne du cône calculée tous les 100 m. Pour les profils orientaux et centraux, le profil tracé en noir à été reconstruit en prenant en compte l'érosion post dépôt. *D'après Palucis et al. (2014).*

par Palucis et al. (2014) utilise une taille de sédiment minimum de 30 mm. Nous choisissons donc d'utiliser une valeur concordante de $d_s = 40$ mm, et supposons que celle-ci reste constant le long du cône. Nous considérons donc que la diminution de la pente du cône vers l'aval est déterminée par une diminution du flux sédimentaire. Nous pouvons donc, en utilisant les équations reliant la pente du cône aux paramètres d'entrée pour un écoulement turbulent, reconstruire les flux à partir du profil du cône. Pour ce faire, nous considérons que la pente atteinte au pied du cône correspond à la pente seuil, définie par,

$$S_H = \left(g\,\mu^3 \left(\frac{\theta_c}{\mu}\,\frac{\rho_s - \rho}{\rho}\,d_s \right)^5 \right)^{1/4} \sqrt{\frac{2^{3/2}\,\mathcal{K}(1/2)}{3\,C_f\,Q_w}}\,. \tag{6.5}$$

Pour estimer le débit d'eau à partir de l'équation (6.5), nous avons besoin des caractéristiques des grains et de l'écoulement. La majorité de la surface martienne est constituée de basalte, nous considérons donc que la densité des sédiments ρ_s est égale à 3000 $\mathrm{kg\,m^{-3}}$. Pour les raisons explicitées précédemment nous choisissons une taille de grain égal à 40 mm. L'accélération de la gravité g sur Mars est égale à 3.7 $\mathrm{m\,s^{-2}}$. Le coefficient de friction μ, est un paramètre géométrique qui ne doit pas dépendre des conditions environnementales. Les observations de Atwood-Stone and McEwen (2013) ont confirmées que ce paramètre n'est pas modifié par la faible gravité martienne, nous prenons donc $\mu = 0.7$. Enfin, nous prendrons des valeur de $\theta_c = 0.04$ et $C_f = 0.1$

(Williams et al., 2013; Palucis et al., 2014).

Finalement, nous obtenons un débit d'eau de l'ordre de 0.8 $m^3 s^{-1}$. Cette valeur est du même ordre de grandeur (bien que cinq fois inférieure) que celle estimée par Palucis et al. (2014), qui proposent un débit de 3.7 $m^3 s^{-1}$.

En ce qui concerne le flux de sédiment, de la même façon que sur le cône de la Guertu (Chapitre 6), nous proposons d'utiliser le rapport de la pente proximal sur la pente distale pour estimer le débit de sédiment en fonction du débit de sédiment caractéristique,

$$\frac{Q_s}{Q_s^*} = \left(\left(\frac{S}{S_H} \right)^2 - 1 \right) \frac{2^{2/3} \mathcal{K}(1/2)}{3}. \tag{6.6}$$

Dans le cas du Peace Vallis fan, la pente proximale est trois fois supérieure à la pente distale, ce qui donne un flux de sédiment 14 fois supérieur au flux de sédiment caractéristique, Q_s^*. Pour estimer le flux de sédiment absolue il est nécessaire de quantifier ce flux caractéristique. Celui-ci dépend de la taille des grains et de la longueur de diffusion. Des expériences sont actuellement en cours dans l'équipe pour définir la relation entre la longueur de diffusion et les caractéristique de l'écoulement et des sédiments.

Appendix A

Threshold of sediment motion

A.1 The critical Shields number

When a grain is immersed into a flow, two forces act on it; a normal force induced by gravity, F_n, and a tangential force induced by the flow, F_t (Fig. A.1).

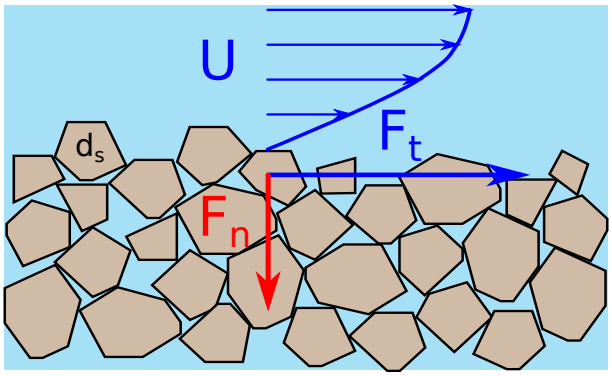

Figure A.1: Forces acting on an immersed grain.

The normal force is proportional to the volume of the grain d_s^3, and the density difference $(\rho - \rho_s)$:

$$F_n = \alpha d_s^3 (\rho_s - \rho) g, \tag{A.1}$$

where d_s is the grain diameter, g the acceleration of gravity, ρ and ρ_s the densities of the fluid and of the sediment respectively and α a shape factor. The tangential force depends on the flow-induced shear stress, τ, and the grain surface, d_s^2, according to

$$F_t = \beta d_s^2 \tau, \tag{A.2}$$

where β is another shape factor.

When the grain is at equilibrium, the ratio of the tangential force over the normal force is equal to the friction coefficient, μ (de Coulomb, 1821)

$$\frac{F_t}{F_n} = \mu. \tag{A.3}$$

When the ratio of the tangential force over the normal force is higher than μ, the grain is set into motion. In the context of fluvial geomorphology, this Coulomb's law is expressed in term of the Shields number (Shields, 1936),

$$\theta = \frac{\tau}{(\rho_s - \rho) g d_s}. \tag{A.4}$$

The critical Shields number corresponds to the threshold of sediment motion. It is related to the friction coefficient, μ, through the shape factors (Seizilles de Mazancourt, 2013):

$$\theta_c = \mu \frac{\alpha}{\beta}. \tag{A.5}$$

The critical Shields number depends on the grain and fluid characteristics, Re_*, (Fig. A.2). A lot of studies, tried to experimentally measure this number, but at present there is no reliable experimental curve (Shields, 1936; Mantz, 1977; Yalin and Karahan, 1979; Charru et al., 2004; Loiseleux et al., 2005; Ouriemi et al., 2007, 2009; Aussillous et al., 2013)

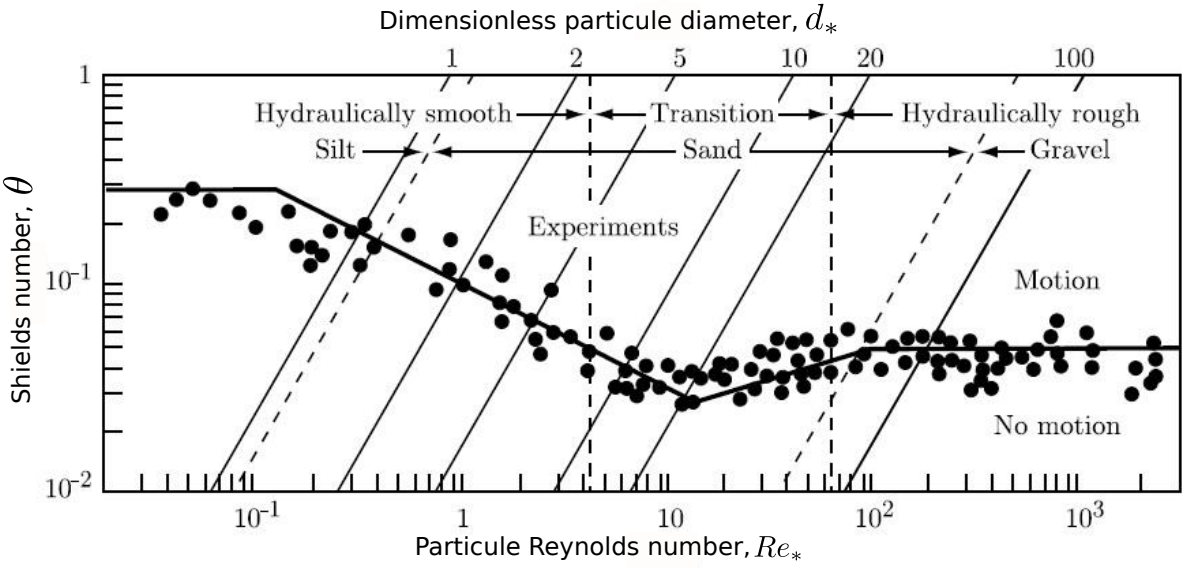

Figure A.2: Threshold of motion for granular material. $Re_* = \frac{u d_s}{\nu}$, where u is the flow velocity, and $d_* = \frac{Re_*^2}{\theta}$. *From (Julien, 2010).*

The critical Shields number θ_t and the particle Reynolds Re_* depend both on the fluid shear stress as a consequence Andreotti et al. (2012) propose to use another dimensionless number, to characterize the fluid and the sediment: the Archimedes number Ar. This dimensionless number represents the ratio of gravitational an inertial stress over viscous stress.

$$Ar = d_s^3 \frac{\rho_s - \rho}{\rho} \frac{g}{\nu^2} \tag{A.6}$$

Near the threshold, the Archimedes number is related to the particle Reynolds number through,

$$Re_* = \theta_c \, Ar \tag{A.7}$$

Because they does not exist a reliable Shields curve, we have to measure the critical Shields number for each sediment and fluid used (*i.e.* for each Archimedes number).

A.2 Experimental set-up

To calibrate the transport laws of our sediments, we use an independent set-up similar to that of Seizilles et al. (2014) (Fig. A.3). The flow is confined between two Plexiglas panels separated by a 3.2 cm-wide gap in which we inject water and sediment at constant rate. Once the experiment has reached equilibrium, typically 10 to 20 hours after it started, we measure the slope of the water surface S to estimate the shear stress τ. We use the same fluid and sediment as the one used in the main experiments.

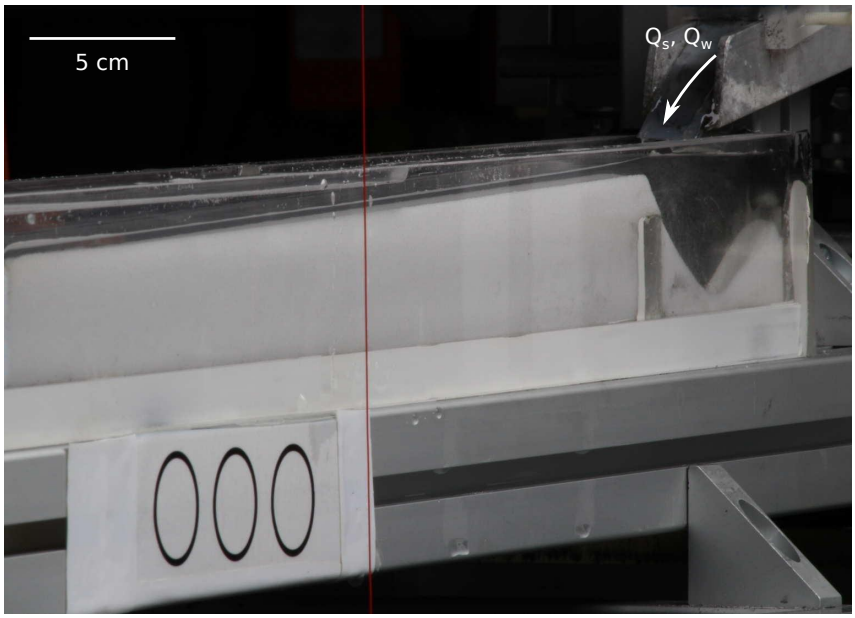

Figure A.3: Experimental set-up used to calibrate our transport laws. Pictures are taken with an angle to increase the slope and facilitate its measurement.

Since the Reynolds number is below 500 in our flume (even when the fluid is water), we may assume that the flow is laminar. For simplicity, we also assume that the bed is flat, consequently the flow-induced shear stress is the same everywhere. The shear stress acting on the sediment thus follows Poiseuille's law:

$$\tau = \rho (Sg)^{2/3} \left(\frac{3 Q_w \nu}{W} \right)^{1/3}, \tag{A.8}$$

where W is the width of the channel, and ν the viscosity of the fluid. We then compute the Shields parameter, which represents the ratio of the flow-induced shear stress τ to gravity:

$$\theta = \frac{\tau}{(\rho_s - \rho) g d_s}, \tag{A.9}$$

During each experiment we maintain constant fluid and sediment discharges then, to calibrate a transport law, we reproduce this experiment with different sediment discharges. For each experiment, we calculate the Shields number using Eq. (A.8). We find that below a critical value θ_c, which correspond to a critical shear stress τ_c, the sediment flux vanishes. Above this threshold, the sediment flux appears proportional to the departure from the critical Shields parameter (Fig. A.4):

$$q_s = \frac{Q_s}{W} = q_0(\theta - \theta_c), \tag{A.10}$$

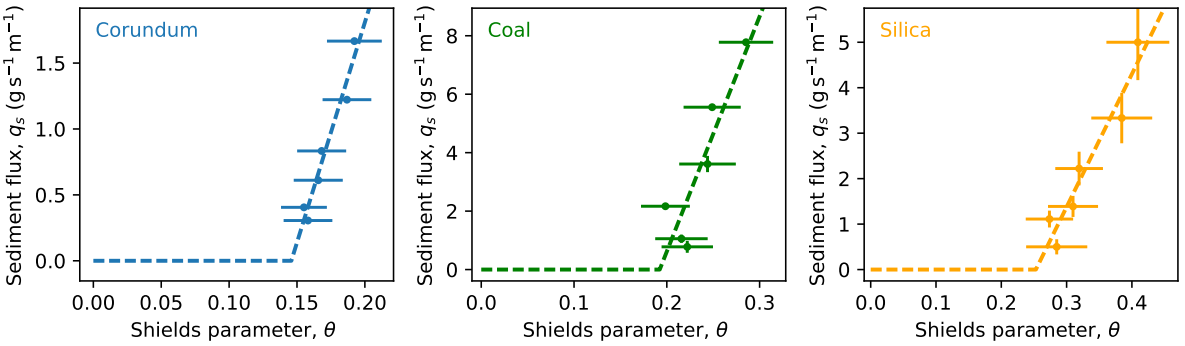

Figure A.4: Transport laws of the three granular material used. For the corundum: $q_0 = 162 \pm 5$ g s^{-1} m^{-1}, $\theta_c = 0.14 \pm 0.005$. For the coal $q_0 = 77 \pm 20$ g s^{-1} m^{-1}, $\theta_c = 0.19 \pm 0.008$. For the silica: $q_0 = 28 \pm 9$ g s^{-1} m^{-1}, $\theta_c = 0.25 \pm 0.02$.

Appendix B

Experimental design

B.1 Sediment feeder

To inject a constant and low sediment discharge over long periods of time (up to 3 days), we designed a conveyor-belt dispenser. Sediments are stored in a hopper placed over a conveyor belt (Norcan). A stepper motor controlled by an Arduino motor Shield imposes the velocity of the belt. To adjust the sediment flux, two parameters can be changed: the distance between the hopper and the belt, and the belt speed. To monitor the sediment discharge injected into the experiment, the entire device is placed on an electronic scale (Ohaus, Explorer 35, Fig. B.1).

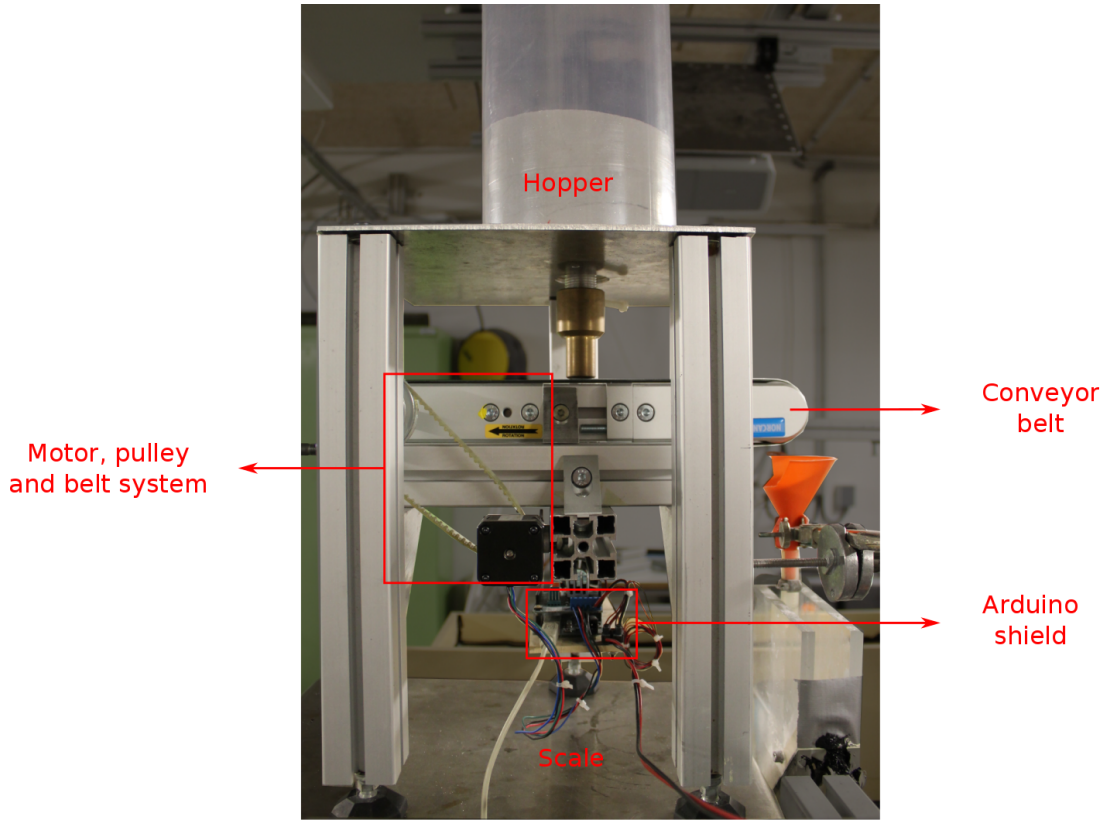

Figure B.1: Sediment feeder designed for our experiments.

B.1.1 Devices

The conveyor belt The conveyor belt is crafted by Norcan (Fig. B.2). To reduce the speed rotation, we fix a pulley on the output shaft.

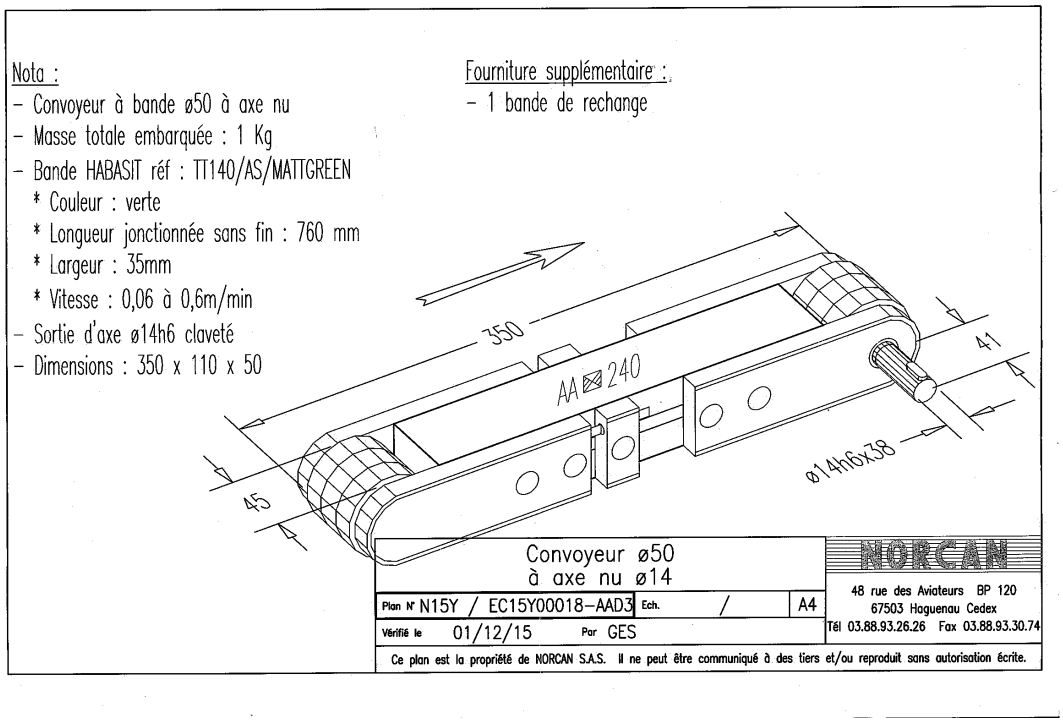

Figure B.2: Plan of the conveyor belt. Dimensions are in millimeters.

The motor The motor used is a high torque hybrid stepper motor[1]. The model is the 42SH33-4AM (Fig. B.3). We also fix a pulley on the output shaft.

The belt and pulley system The conveyor belt and the motor are linked by a belt and pulley system. This allows for mechanical power, torque, and speed to be transmitted across axes. We use one pulley composed of 10 teeth (diameter = 16 mm) fixed on the motor and one composed of 35 teeth (diameter = 55 mm) fixed on the conveyor belt. These pulleys are connected by a belt of 9.8 mm width and 390 mm long. With this system the velocity is divided by 3.5.

B.1.2 Stepper motor control

Arduino UNO The Arduino UNO is a microcontroller board connected to a computer with a USB cable. It converts an analogical signal to a numerical signal and vice versa.

Arduino motor Shield R3 To control the velocity of the motor, we use an Arduino with a motor shield R3[2]. The Arduino motor shield use a dual full bridge driver L298 which drives inductive loads such as stepper motor (Fig. B.4).

[1] `http://docs-europe.electrocomponents.com/webdocs/133e/0900766b8133e904.pdf`
[2] `https://store.arduino.cc/arduino-motor-shield-rev3`

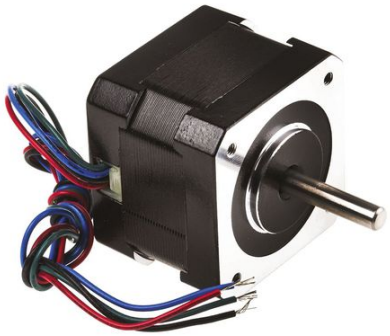

Figure B.3: Stepper motor, model 42SH33-4AM.

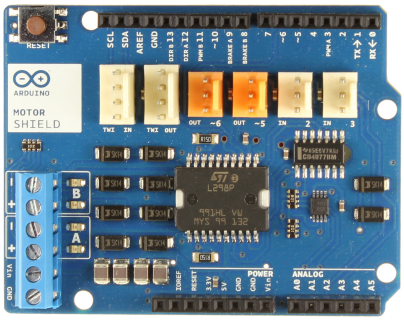

Figure B.4: Arduino motor shield R3

The shield has two separate channels. Each uses four of the Arduino pins to drive or sense the motor (direction, pulse width modulation, brake and current sensing). Combining these two channels, we can drive one bipolar stepper motor. We only need to turn on each channel alternatively. To do so we use the following Arduino sketch[3]. The motor speed is inversely proportional to the delay we impose between the activation of each channel.

```
/* Arduino sketch to control a stepper motor, the delay length, is the time between two
    step and has to be input in the arduino monitor */

// establish motor direction toggle pins
const int dirA = 13;
const int dirB = 12;

// establish motors pins
const int motA = 11;
const int motB = 3;

//establish motor brake pins
const int brakeA = 8;
const int brakeB = 9;

float delayLength = 0;

void setup() {                                  // run once, when the sketch starts
  Serial.begin(9600);                           // set up Serial library at 9600 bps
  pinMode(dirA, OUTPUT);
  pinMode(dirB, OUTPUT);
  pinMode(brakeA, OUTPUT);
  pinMode(brakeB, OUTPUT);
  pinMode(motA, OUTPUT);
  pinMode(motB, OUTPUT);
}

void loop() {                                   // run over and over again
  if (Serial.available()> 0){

    delayLength = Serial.parseFloat();      // read the value of delay length on the
    monitor
    Serial.print("New dt: ");
    Serial.print(delayLength);
    Serial.print("\n");
```

[3] http://www.instructables.com/id/Arduino-Motor-Shield-Tutorial/

```
    Serial.flush();
    }

  digitalWrite(brakeA, LOW);                    // Activation of the first channel
  digitalWrite(brakeB, HIGH);

  digitalWrite(dirA, HIGH);
  digitalWrite(motA, HIGH);

  delay(delayLength);                           // time break

  digitalWrite(brakeA, HIGH);                   // Activation of the second channel
  digitalWrite(brakeB, LOW);

  digitalWrite(dirB, HIGH);
  digitalWrite(motB, HIGH);

  delay(delayLength);                           // time break

  digitalWrite(brakeA, LOW);                    // Activation of the first channel
  digitalWrite(brakeB, HIGH);

  digitalWrite(dirA, LOW);
  digitalWrite(motA, HIGH);

  delay(delayLength);                           // time break

  digitalWrite(brakeA, HIGH);                   // Activation of the second channel
  digitalWrite(brakeB, LOW);

  digitalWrite(dirB, LOW);
  digitalWrite(motB, HIGH);

  delay(delayLength);                           // time break
  }
```

B.1.3 Discharge regularity

To illustrate the constancy of the sediment discharge provided by our conveyor-belt system, Fig. (B.5a) shows the evolution of the mass of sediment in the hopper as a function of time, over more than four hours. The mass of sediment decreases linearly with time, which means that the sediment discharge is constant. In this system, the sediment discharge is controlled by the draining of the hopper. Contrary to fluid draining, the flow of granular solids through orifices does not depend on the height of grains in the hopper (Beverloo et al., 1961). To ensure that, in our system, the sediment discharge does not depend on the mass of sediment in the hopper, Fig. (B.5b) represents the sediment discharge as a function of the mass in the bin . The sediment discharge stays constant. However, we note that there is a slight increase of discharge when the hopper is almost empty. This increase is about 2% (Fig. B.5b). Therefore we only need to ensure that the hopper never empties to keep the sediment discharge constant.

Finally, to make our experiment reproducible, we calibrate the sediment discharge. For a fixed distance between the hopper outlet and the belt, we find that the sediment discharge evolves linearly with the inverse of the delay imposed to the stepper motor (Fig. B.6).

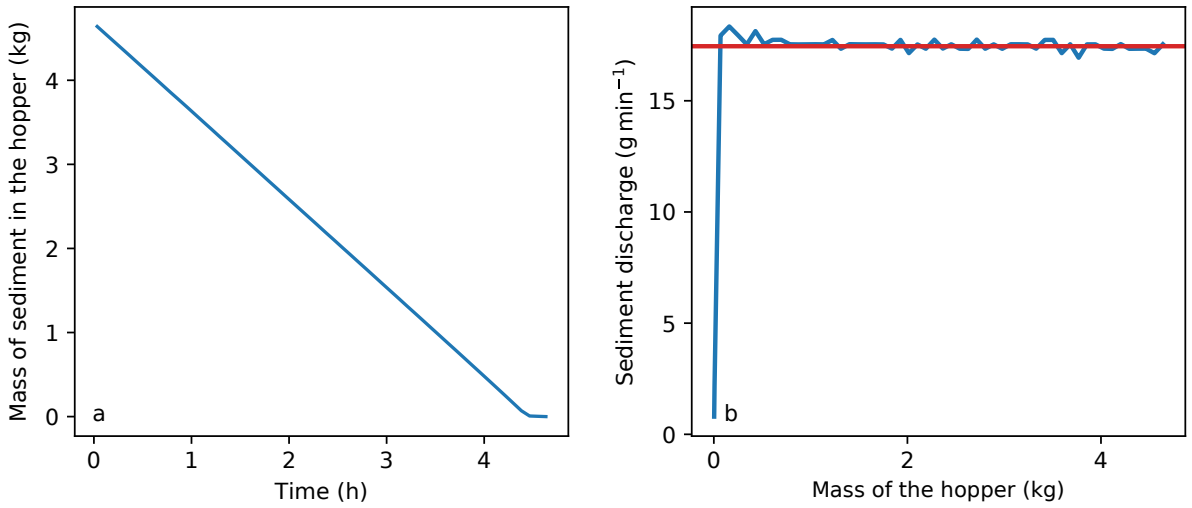

Figure B.5: a) Mass of the hopper versus time, the slope corresponds to the sediment discharge. b) Sediment discharge as a function of the mass of sediment into the hopper. The red line shows the mean sediment discharge.

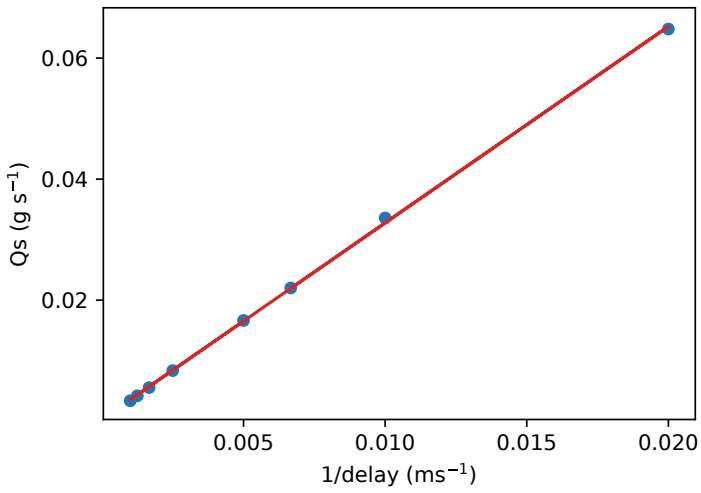

Figure B.6: Sediment discharge as a function of the inverse of the delay time imposed to the motor (proportional to motor speed), $Q_s = 3.25 \times \frac{1}{\text{delay}}$.

B.2 Fluid discharge

The fluid we use is a mixture of water and glycerol. The physical properties, density and viscosity of this mixture depend on its composition (Shankar and Kumar, 1994, Fig. B.7).

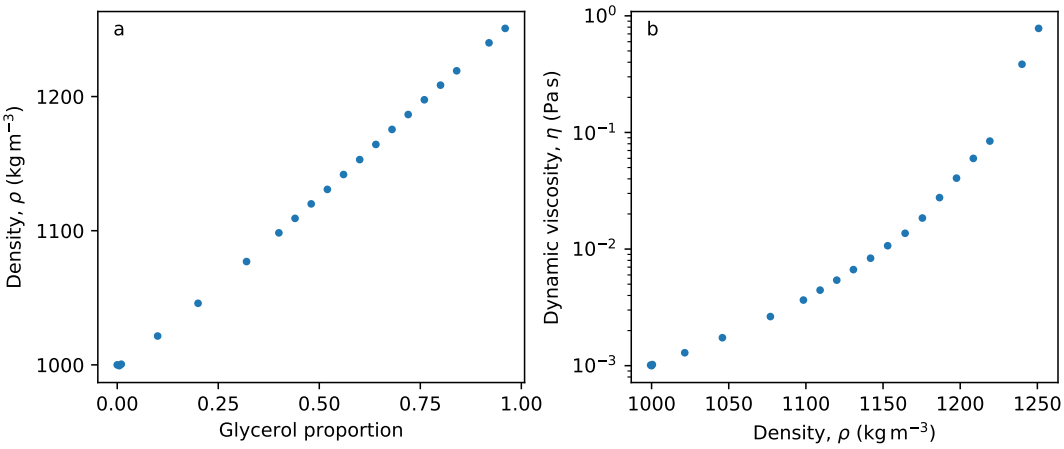

Figure B.7: Evolution of the characteristics of the fluid as a function of its composition. a) Density of the mixture as a function of its glycerol contents. b) Relation between density and viscosity of the mixture.

The fluid discharge has to stay constant during our experiment. We observe that after a long period however, the fluid discharge decreases. This decrease is caused by water evaporation, which increases the fluid density and viscosity. The discharge can be estimated using Poiseuille's law to represent the flow in the pipe connecting the tank to the experiment,

$$Q_w = \pi r^4 \frac{gz\rho}{8\eta L}, \tag{B.1}$$

where r is the tube radius, z the tank elevation, and L the pipe length.

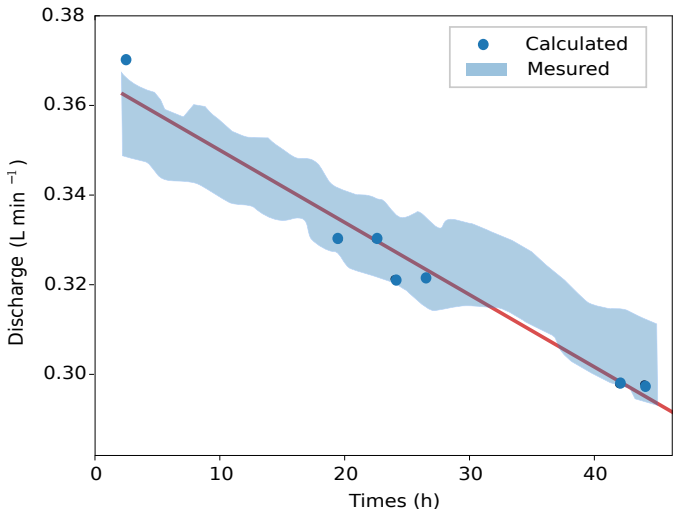

Figure B.8: Variation of the fluid discharge caused by the evaporation of the water from the mixture. The shaded area corresponds to the fluid discharge measured with an electromagnetic flowmeter, dots are calculated using Eq. (B.1).

To test the influence of evaporation, we measure the density and viscosity of the fluid at different times during a test experiment and compare the discharge predicted by Poiseuille's law to the discharge indicated by an electromagnetic flowmeter (Kobold, MIK-5NA10AE34R[4], Fig. B.8). We find that the data accord with each other, suggesting that the discharge variation is indeed caused by evaporation. As a consequence, to keep the fluid discharge constant during the run, we regularly measure the density of our mixture, and, when necessary, we add water to compensate for evaporation.

B.3 Experiment monitoring

During the experiment, we regularly record the fluid discharge, the mass of sediment in the hopper and we acquire top-view pictures. Because the experiment runs continuously for more than one day, we automate these acquisitions using Python codes. The libraries *pySerial*[5] and *pyFirmata* [6] allow us to control the Arduino, and we use the *gphoto*[7] library to control the camera. The following library (called *pyCone.py*) contains the necessary functions to control our devices.

```
import time
from pyfirmata import Arduino, util
import os

#####################################
#ARDUINO#
#####################################
################################################## Connection to Arduino

def connect_arduino():

        port_base_name = '/dev/ttyACM'
        port_suffix_list = ['0','1','2','3','4']

        board_conneced = False

        for port_suffix in port_suffix_list :

                port = port_base_name + port_suffix

                try :
                        print 'Trying port ' + port
                        board = Arduino(port)
                        board_connected = True
                        break

                except :
                        print 'Failed on port ' + port

        if board_connected :

                it = util.Iterator(board)
```

[4] http://www.kobold.com/fr/product/detail/~nm.61~nc.17~id.566/Electromagnetic-Dosing-Electronic-MIK-..G.html

[5] https://pypi.python.org/pypi/pyserial/2.7

[6] https://pypi.python.org/pypi/pyFirmata

[7] http://gphoto.org/

```
                it.start() # necessary for tension meausurements

                time.sleep(.1)

                print 'Connected to Arduino at ' + port

        else :

                print 'Failed to connect to Arduino!'

        return board

#####################################
#FLOWMETER#
#####################################
############################################ Measure tension

def get_tension(board, pin_number, nb_measures = 10 ) :

        board.analog[pin_number].enable_reporting()
        time.sleep(.1)

        tension = []

        for n in range(nb_measures) :
                tension = tension + [ board.analog[pin_number].read() ]

        tension = array(tension)

        if ( abs(tension) > 1.0 ).any() :
                return nan

        else :
                return mean(tension)*5. # volts

########################################### Convert tension into discharge

def tension2discharge(tension):

        range_intensity = [ 4e-3, 20e-3] # Amp
        range_discharge = [ 0, 1.001 ] # L/min
        resistance = 217. # ohm
        intensity = tension/resistance # ampere

        return range_discharge[0] + ( intensity - range_intensity[0]) *(range_discharge
    [1] - range_discharge[0])/(range_intensity[1] -range_intensity[0])

########################################### record discharge

def get_discharge(board) :
        return tension2discharge(get_tension(board,0))

#####################################
#CAMERA#
#####################################
############################################ Camera configuration

def param(iso=0, shutterspeed= 20, aperture= 21): #Default parameters
        os.system('gphoto2 --set-config-index iso=%i'%iso)
        os.system('gphoto2 --set-config-index shutterspeed=%i'%shutterspeed)
        os.system('gphoto2 --set-config-index aperture=%i'%aperture)
```

```
        time.sleep(2)
        os.system('gphoto2 --get-config iso=%i'%iso)
        os.system('gphoto2 --get-config shutterspeed=%i'%shutterspeed)
        os.system('gphoto2 --get-config aperture=%i'%aperture)

#####################################
#BALANCE#
#####################################

class balance:
        """ A simple class to control a weighting device
                        specifies the parameters of three common weighting devices
                        enables to get the weight using a simple function call
        """
        def __init__(self,bal='Ohaus50',com='/dev/ttyACM0'):
                """ initilize the balance: specify it type and the com por tot be used
    """
                self.PortComm=serial.Serial()
                self.PortComm.timeout = 5
                self.PortComm.port=com

                # sets the parameters for acquisition
                # checked for the Ohaus 50 and the Explorer 35
                self.bal=bal
                if self.bal == 'Ohaus50':
                        print self.bal
                        self.PortComm.baudrate = 9600
                        self.PortComm.parity = serial.PARITY_NONE
                        self.PortComm.stopbits = serial.STOPBITS_TWO
                        self.PortComm.bytesize = serial.SEVENBITS
                        self.Ordre = "P\r\n"
                        self.Ilength = 8
                elif self.bal=='Explorer35':
                        print self.bal
                        self.PortComm.baudrate = 9600
                        self.PortComm.parity = serial.PARITY_NONE
                        self.PortComm.stopbits = serial.STOPBITS_TWO
                        self.PortComm.bytesize = serial.SEVENBITS
                        self.Ordre = "SI\r\n"
                        self.Ilength = 19
                elif self.bal=='Explorer22':
                        print self.bal
                        self.PortComm.baudrate = 9600
                        self.PortComm.parity = serial.PARITY_NONE
                        self.PortComm.stopbits = serial.STOPBITS_TWO
                        self.PortComm.bytesize = serial.SEVENBITS
                        self.Ordre = "P\r"
                        self.Ilength = 8
                elif self.bal=='KERN':
                        print self.bal
                        self.PortComm.baudrate  = 9600
                        self.PortComm.parity = serial.PARITY_NONE
                        self.PortComm.stopbits = serial.STOPBITS_ONE
                        self.PortComm.bytesize = serial.EIGHTBITS
                        self.Ordre=""
                if self.PortComm.isOpen():
                        self.PortComm.close()
                self.PortComm.open()

        def GetWeight(self):
                """ retrieves the current weight of the balance"""
```

```
            if self.Ordre<>"":
                    self.PortComm.flushInput()
                    self.PortComm.write(self.Ordre)
                    bytesread=self.PortComm.read(self.Ilength)
            else:
                    self.PortComm.flushInput()
                    bytesread=self.PortComm.readline()

            if self.bal == 'Explorer22':
                            poids = bytesread[1:8]
            elif self.bal== 'Ohaus50':
                            poids = bytesread
            elif self.bal == 'Explorer35':
                            poids = bytesread[6:13]
            elif self.bal == 'KERN':
                            poids= str(bytesread)[:-6]

            # if a value of weight is returned convert to float
            if poids!='':
                    try:
                            poids = float(poids)
                    except:
                            poids = -999
            else:
                    poids=0

            return poids

    def close(self):
            """ close COM port"""
            self.PortComm.close()
```

Using these functions, we can automatically acquire the fluid discharge, the sediment discharge and take pictures of our experiment. We choose to save all of our experimental data in a database using MySQL. The following code allows to measure the fluid discharge from the flowmeter every ten seconds and take picture every five minutes. To have homogeneous lighting for our picture, a light panel is automatically switched on before the picture is taken.

```
from pyCone import *
from datetime import *
import time
import sys
import os
import MySQLdb

# Connection database

conn = MySQLdb.connect(host="localhost", user="manip", passwd="manip", db="
    experimental_fan")

cursor = conn.cursor()

# Connection Arduino

board = connect_arduino()

# initialisation

t0 = time.time()
```

```
d=datetime.today()

print d.strftime("%d/%m/%y , %H:%M:%S")

###Specific arguments of the experiment

code_manip = sys.argv[1]

#time sleep between two flow measurement

inter=sys.argv[2] # 10 s

#Folder and name of the saved pictures

folder=sys.argv[3]
fname=sys.argv[4]

# Sediments characteristics

rhos = sys.argv[5]
ds = sys.argv[6]

# Camera configuration
iso=sys.argv[7]
shutterspeed=sys.argv[8]
aperture=sys.argv[9]

## Save experiment characteristic in database

sql = "insert into manip values (%s, %s, %s, %s)"
cursor.execute (sql, (int(code_manip), d, rhos, ds))
conn.commit()

#start the loop of measurement, until we stop the experiment
j = 1
i = 1

while True:

        # fluid discharge measurement
        valtime=time.time()
        T = valtime - t0
        tension = get_tension( board, 0 )
        discharge = tension2discharge(tension)
        print T , discharge

        # save value in database
        sql = "insert into fluid values (%s, '', %s, %s)"
        cursor.execute (sql, (int(code_manip), T, discharge))
        conn.commit()


        if j/30. == fix(j/30.) : # 30 correspond to an interval of 5 min between two
    pictures

                # Switch on light
                board.digital[3].write(1)
                board.digital[2].write(1)

                # Configuration camera
                param(int(iso),int(shutterspeed), int(aperture))
```

```
                # picture name
                output="%s/%s_%s" % (folder,fname,i)

                # takes picture
                command="gphoto2 --capture-image-and-download --filename %s" % (output)
                os.system(command)
                valtime=time.time()
                T = valtime - t0
                print output,T
                i = i+1

                # Switch off light
                board.digital[3].write(0)
                board.digital[2].write(0)

                # save picture path in database
                sq = "insert into picture values (%s, '', %s, %s)"
                cursor.execute (sq, (int(code_manip), output, T))
                conn.commit()

        #time sleep before next loop
        time.sleep(int(inter))

        j = j + 1

end = datetime.today()
print end.strftime("%d/%m/%y, %H:%M:%S")
conn.close()
```

The next code allows to measures and records the mass of sediment on the scale. This measurement allow us to estimate the sediment discharge.

```
from pylab import *
from pyCone import *
import time
import serial
import MySQLdb

# Connection database

conn = MySQLdb.connect(host="localhost", user="manip", passwd="manip", db="
    experimental_fan")

cursor = conn.cursor()

## arguments

code_manip=sys.argv[1]
tstep=float(sys.argv[2])  # time sleep between two measurements

#connection to balance

a=lab.balance('Explorer35','/dev/ttyUSB0')
a_weight=[]
t=[]
t0=time.time()

#loop to measure weight until we stop the experiment
while 1:
```

```
        # get weight
        valWa=a.GetWeight()

        # register time
        tm=time.time()-t0

        # save data in databse
        sql = "insert into sediment values (%s,'', %s, %s)"
        cursor.execute (sql, (int(code_manip), tm, valWa))
        conn.commit()
        st="%f\t%s\n" % (tm,valWa)
        print st
        time.sleep(tstep)

conn.close()
```

Appendix C

Measurements

C.1 Detection of the fan boundary

To detect the fan boundary automatically, we use the *canny* filter function of the *skimage*[1] python libraries. We first convert our fan picture from RGB to grayscale (Fig. C.1a). This conversion attributes one value, between 0 and 1, to each pixel. Because the color of our fan differs from the color of the shelf on which it is built, we can select a threshold value to isolate the pixels that compose the fan. In our case, the threshold value is 0.4. The *canny* filter then detects the boundary of the domain where pixels have a value higher than the threshold. Finally, we extract the x and y positions of this boundary (Fig. C.1b).

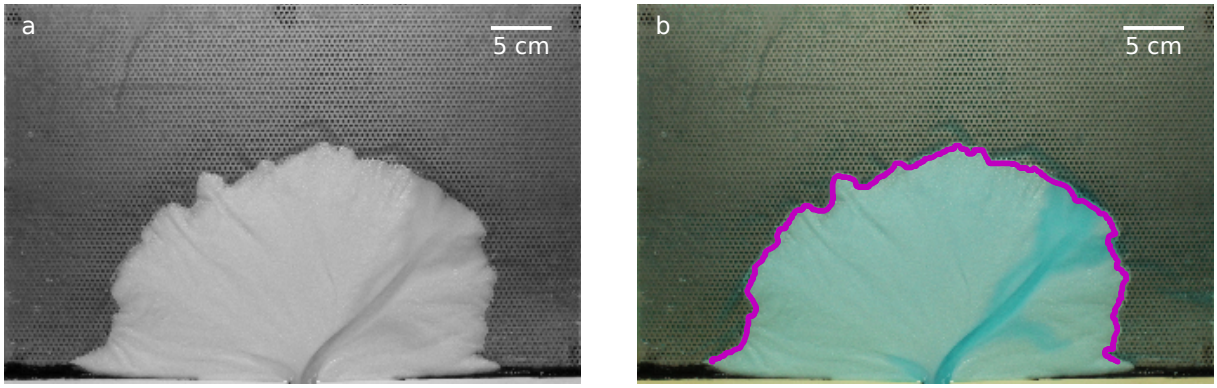

Figure C.1: a) Top-view grayscale picture of the fan. b) Top-view picture of the fan (RGB mode), with the boundary detected (magenta line).

To measure the average radius of the fan, we calculate the distance from the apex of the fan to each pixel of the boundary. Because we assume our fan is axisymmetric, we consider that the mean radius is a good approximation of the fan size. We treat the variability of this radius as an error.

[1] `http://scikit-image.org/docs/dev/api/skimage.html`

C.2 Fan morphology acquisition

C.2.1 Moiré pattern

To measure the morphology of our experimental fan, we use a phase unwrapping technique (Bruning et al., 1974; Brémand, 1994). A video-projector projects a pattern, composed of sinusoidal fringes with a grating spacing p and an incidence angle i, on the experiment (Fig. C.2). The topography of the fan deforms the projected pattern, which is then recorded using a camera fixed above the experiment (Ueyes USB 2 SE[2], with a Pentax Ricoh 5 megapixel lens FL-CC1614-5M[3])

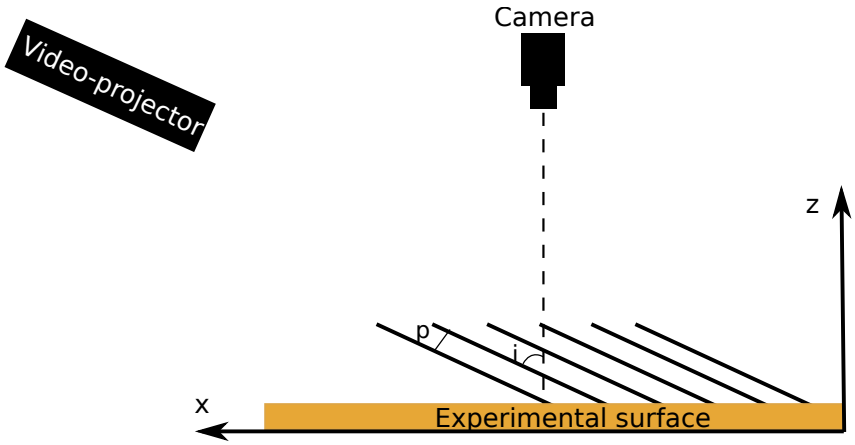

Figure C.2: Digital elevation model acquisition, using a Moiré pattern.

Projected on a flat surface the fringes are regularly spaced,

$$\varphi(x) = \frac{2\pi}{p} x \cos i. \tag{C.1}$$

On the contrary, when the surface is irregular, the phase is shifted proportionally to the height of the surface,

$$\delta\varphi(z) = \frac{2\pi}{p} z \tan i. \tag{C.2}$$

The phase expression, Eqs. (C.1) and (C.2), are modulo 2π. Consequently, the reconstruction of the surface map requires phase unwrapping procedure (Limare et al., 2011). Using a set of phase-shifting pictures, this procedure allows the removal of jumps larger than π between adjacent pixels (Limare et al., 2011, Fig. C.3).

This method allows for image-based measurements over a continuous surface at high frequency. We use the *Light3D* commercial software package to measure our fan topography every hour during an experimental run.

C.2.2 Calibration

To measure precisely the elevation of our experimental fan, we need to calibrate and estimate the accuracy of our measurement system. To do so, we scan the surface of a milk bath, and we use it

[2] https://fr.ids-imaging.com/store/products/cameras/usb-2-0-cameras/ueye-se.html
[3] https://industry.ricoh.com/en/fa_camera_lens/lens/5m/

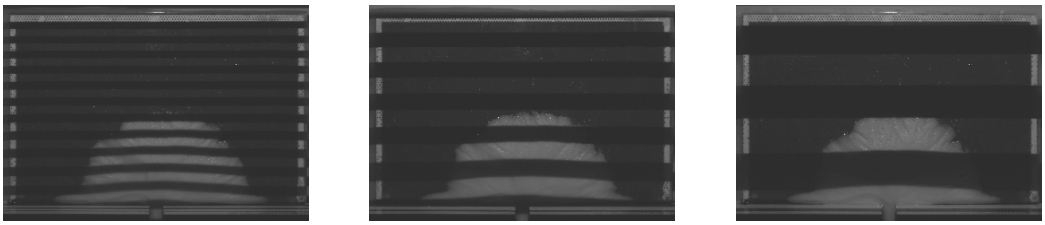

Figure C.3: Phase-shifting pictures showing the deformation of the projected pattern induced by the fan topography.

as a reference for horizontality. We then elevate this bath at different elevations, h (Fig. C.4). We observe that the elevation of the milk plane is measured with an uncertainty of approximately 1 mm. Furthermore, the measured plane is not perfectly flat, it presents a curvature which depends on the distance from the camera. We suspect this deformation is caused by the lens.

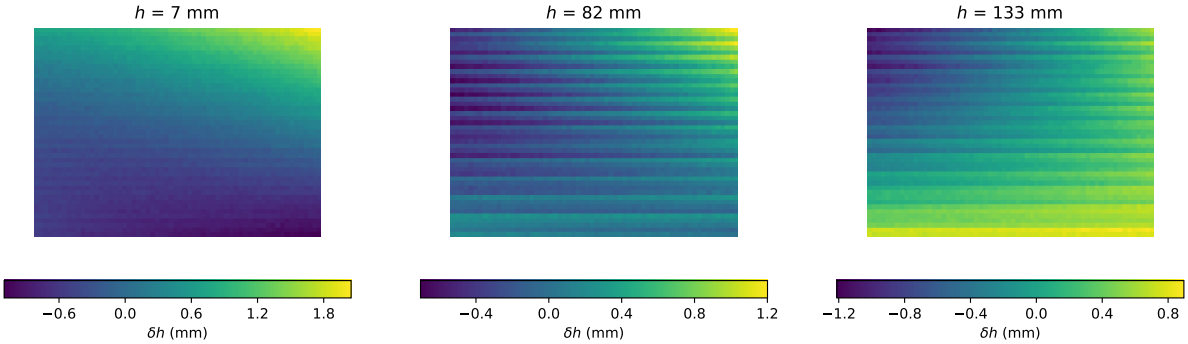

Figure C.4: Topographies of flat horizontal surfaces (milk plate) at different elevations h.

To correct this optical deformation, we apply a numerical correction to the measured data. To do so, we estimate the lens-induced deformation at different elevations throughout the surface extension of the experimental set-up. We measure the elevation of reference surfaces (milk surface), at nine different elevations from 7 to 132 mm above the bottom of the tank, and compare the digital elevation models to the real elevation of the plane. In Fig. (C.4), we observe that the deformation depends on the coordinates X and Y of the pixel. To correct this deformation, we fit the plane by a polynomial function, f,

$$f = c_0 + xc_x + yc_y + xy\ c_{xy} + x^2 c_{xx} + \dots, \tag{C.3}$$

where c_0, c_y, c_{xy} and c_{xx} are the polynomial coefficients which have to be estimated. To know at which order we need to develop this polynomial, we represent the residual error of the fit as a function of the order of the polynomial (Fig. C.5).

We can see that the residual error is mostly accounted by a polynomial of order two, and that a higher one does not improve the correction. Consequently, we fit the deformed surfaces by a second-order polynomial. This function has 6 coefficients which have to be determined.

The aim of our method is to determine the coefficients of the polynomial for each elevation. To do so, we fit the polynomial function to the different planes and calculate the coefficients. We

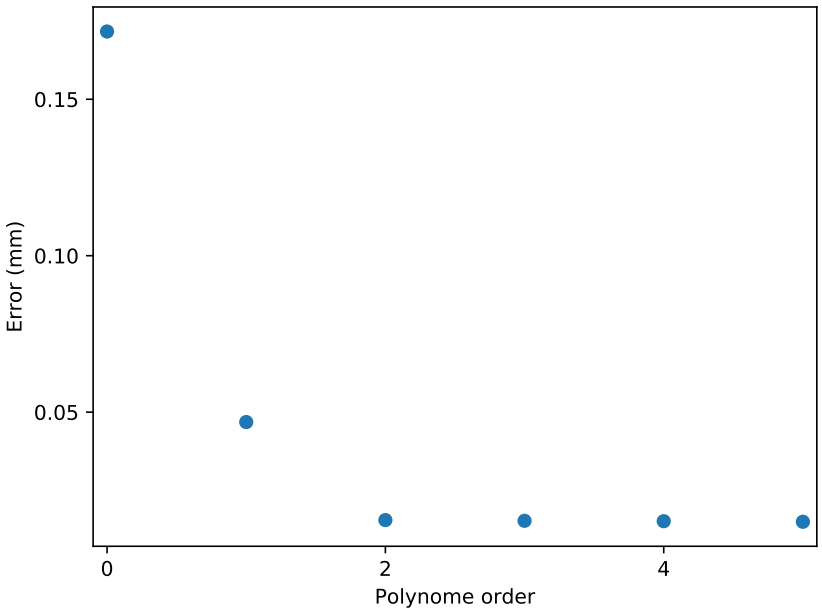

Figure C.5: Error on the fit as a function of the polynomial order.

define $\underline{\underline{M}}(Z)$, the matrix of the coefficient, such as,

$$\underline{\underline{M}}(Z) \cdot P_{xy} = Z_{\text{meas}} - Z_{\text{true}}, \tag{C.4}$$

where P_{xy} is the coordinates vector ($P_{xy} = [1, x, y, xy, x^2, ...]$) of each Z point, Z_{meas} is the elevation given by the DEM and Z_{true} is the real elevation of the plane (*i.e.* h).

We then estimate the evolution of these coefficients with the elevation, h. Figure (C.6) shows that the coefficients vary linearly with elevation. Accordingly, we rewrite $\underline{\underline{M}}(Z)$ as

$$\underline{\underline{M}}(Z) = \underline{\underline{M_0}} + h\underline{\underline{M_1}}, \tag{C.5}$$

where $\underline{\underline{M_0}}$ and $\underline{\underline{M_1}}$ are the matrix containing the coefficients of the linear regressions performed on the data (Fig. C.6).

Finally, using Eqs. (C.4) and (C.5), we are able to determine the real elevation of the plane.

$$Z_{true} = \frac{Z_{meas} - \underline{\underline{M_0}} \cdot P_{xy}}{1 + \underline{\underline{M_1}} \cdot P_{xy}} \tag{C.6}$$

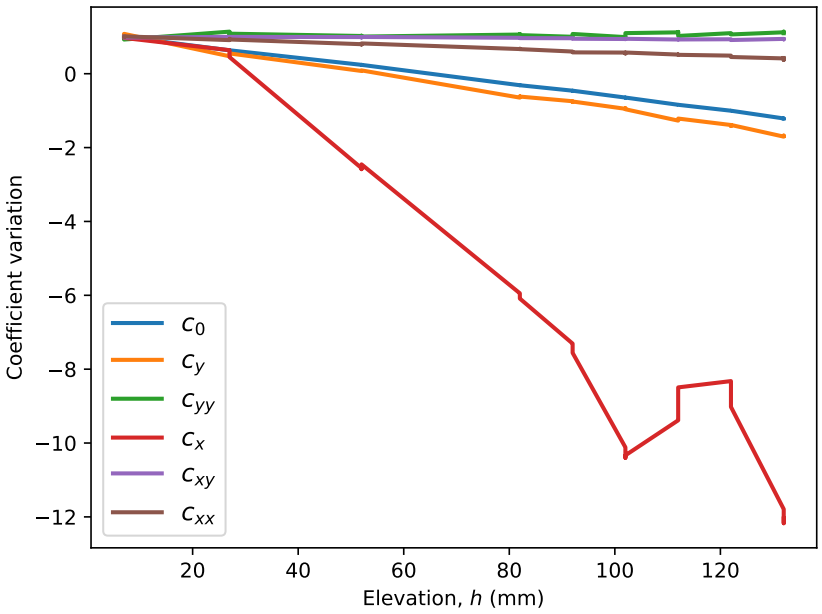

Figure C.6: Variation of the correction-polynomial coefficients with the elevation of the milk surface.

To test the robustness of our numerical correction, we apply Eq. (C.6), to our reference planes (Fig. C.7). After correction, the uncertainty on the measured elevation is less than 400 μm, which corresponds approximately to the size of a grain.

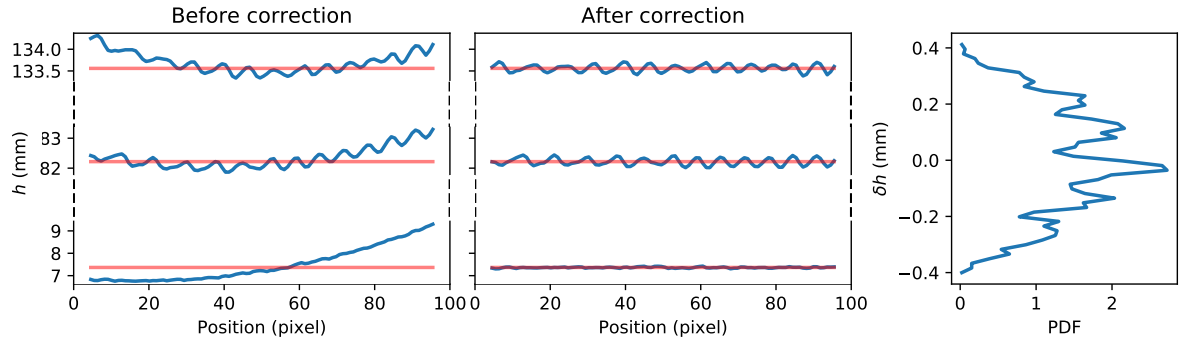

Figure C.7: Blue line: profile along the line of maximum deformation; red line: real elevation of the milk plane. Left: milk plane at different h before correction. Center: milk plane at different h after correction. Right: probability distribution function of the error on the corrected elevation.

Appendix D

List of variables

The units are indicated to introduce the dimension of the variable.

C_f	page 36	Chézy's coefficient of fluid friction	
χ	page 74	dimensionless sediment discharge	
d_s	page 15	sediment diameter	μm
d_{50}	page 37	sediment median diameter	μm
D	page 34	flow depth	cm
ΔQ_w	page 82	variation of the water discharge	
η	page 26	dynamic viscosity	kg $m^{-1}s^{-1}$
f	page 18	fraction of sediment deposited in the fan	
g	page 30	acceleration of gravity	m s^{-2}
h	page 15	fan elevation	m
H_s	page 59	elevation of the silica deposit	m
H_c	page 59	elevation of the coal deposit	m
H	page 74	dimensionless fan elevation	
H_a	page 80	fan apex elevation	m
H_t	page 85	elevation of the gravel-sand transition	m
$\mathcal{K}(1/2)$	page 36	elliptic integral of the first kind	
L	page 27	fan length	m
$\mathcal{L}$	page 34	characteristic length	m
λ	page 18	packing fraction	
l_d	page 30	diffusive length	m
μ	page 34	friction coefficient	
μ_t	page 69	threshold friction coefficient	
n	page 68	number of moving grain	
ν	page 35	kinematic viscosity	m^2s^{-1}
n_c	page 61	number of channnel	
P	page 18	period of fan activity	
ϕ	page 52	composition of the sediment mixture	
ψ	page 34	bed angle in the transverse direction	°
Q_g	page 85	gavel discharge	m^3s^{-1}/g min^{-1}

Q_s	page 15	sediment (or sand) discharge	m^3s^{-1}/g min^{-1}
Q_s^*	page 30	characteristic sediment discharge	m^3s^{-1}/g min^{-1}
Q_w	page 15	fluid discharge	m^3s^{-1}
q_0	page 30	characteristic sediment discharge per unit of width	m^2s^{-1}/kg $s^{-1}m^{-1}$
q_d	page 68	diffusive flux	$m^{-1}s^{-1}$
q_g	page 68	gravity flux	$m^{-1}s^{-1}$
q_s	page 27	sediment discharge per unit of width	m^2s^{-1}/kg $s^{-1}m^{-1}$
q_w	page 27	fluid discharge per unit of width	m^2s^{-1}
R	page 13	fan radius	m
R_c	page 54	radius of coal deposit	m
R_f	page 80	fan radius	m
R_s	page 54	radius of silica or sand deposit	m
R_t	page 85	radius of the gravel-sand transition	m
$\mathcal{R}$	page 55	ratio of proximal over distal radius	
Re	page 26	Reynolds number	
ρ	page 26	fluid density	kg m^{-3}
ρ_s	page 15	sediment density	kg m^{-3}
S	page 14	fan slope	
S_c	page 58	slope of coal deposit	
S_g	page 85	slope of gravel deposit	
S_h	page 30	threshold slope for laminar flow	
S_H	page 62	threshold slope for turbulent flow	
S_s	page 58	slope of silica or sand deposit	
S_t	page 59	slope of the transition	
$\mathcal{S}$	page 59	ratio of the proximal over distal slope	
$\mathcal{S}_t$	page 59	ratio of the proximal over the transition slope	
t	page 23	time	s
T	page 82	time over which variation occurs	s
τ	page 34	flow-induced shear stress	kg $m^{-1}s^{-2}$
τ_c	page 30	critical flow-induced shear stress	kg $m^{-1}s^{-2}$
θ	page 30	Shield number	
θ_c	page 30	critical Shield number	
Θ	page 13	fan aperture angle	°
U	page 35	flow velocity	m s^{-1}
V	page 18	fan volume	m^3
V_c	page 59	volume of coal deposit	m^3
V_g	page 85	volume of gravel deposit	m^3
V_h	page 72	volume of a fan at the threshold	m^3
V_s	page 59	volume of silica or sand deposit	L^3
$\mathcal{V}$	page 72	volume of a fan divided by the corresponding threshold fan	
W	page 43	channel width	m
W_h	page 36	threshold width for laminar flow	m
W_H	page 36	threshold width for turbulent flow	m
X	page 74	dimensionless fan radius	

Bibliography

Abramian, A., Seizilles, G., Devauchelle, O., and Lajeunesse, E. (in prep). Equilibrium shape of rivers by bedload diffusion.

Allen, P. A. (2009). Earth surface processes. John Wiley & Sons.

Allen, P. A. and Densmore, A. (2000). Sediment flux from an uplifting fault block. Basin Research, 12(3-4):367–380.

Andreotti, B., Forterre, Y., and Pouliquen, O. (2012). Les milieux granulaires, Entre fluide et solide. EDP Sciences, Collection Savoirs Actuels.

Armitage, J. J., Duller, R. A., Whittaker, A. C., and Allen, P. A. (2011). Transformation of tectonic and climatic signals from source to sedimentary archive. Nature Geoscience, 4(4):231–235.

Ashworth, P. J., Best, J. L., and Jones, M. (2004). Relationship between sediment supply and avulsion frequency in braided rivers. Geology, 32(1):21–24.

Ashworth, P. J., Best, J. L., and Jones, M. A. (2007). The relationship between channel avulsion, flow occupancy and aggradation in braided rivers: insights from an experimental model. Sedimentology, 54(3):497–513.

Assine, M. L. (2005). River avulsions on the taquari megafan, pantanal wetland, brazil. Geomorphology, 70(3):357–371.

Atwood-Stone, C. and McEwen, A. S. (2013). Avalanche slope angles in low-gravity environments from active martian sand dunes. Geophysical Research Letters, 40(12):2929–2934.

Aussillous, P., Chauchat, J., Pailha, M., Médale, M., and Guazzelli, É. (2013). Investigation of the mobile granular layer in bedload transport by laminar shearing flows. Journal of Fluid Mechanics, 736:594–615.

Beverloo, W., Leniger, H., and Van de Velde, J. (1961). The flow of granular solids through orifices. Chemical engineering science, 15(3-4):260–269.

Blair, T. C. (1987a). Sedimentary processes, vertical stratification sequences, and geomorphology of the roaring river alluvial fan, rocky mountain national park, colorado. Journal of Sedimentary Research, 57(1).

Blair, T. C. (1987b). Tectonic and hydrologic controls on cyclic alluvial fan, fluvial, and lacustrine rift-basin sedimentation, jurassic-lowermost cretaceous todos santos formation, chiapas, mexico. Journal of Sedimentary Research, 57(5).

Blair, T. C. and McPherson, J. G. (1994). Alluvial fans and their natural distinction from rivers based on morphology, hydraulic processes, sedimentary processes, and facies assemblages. Journal of sedimentary research, 64(3):450–489.

Blair, T. C. and McPherson, J. G. (2009). Processes and forms of alluvial fans. In Geomorphology of Desert Environments, pages 413–467. Springer.

Blissenbach, E. (1952). Relation of surface angle distribution to particle size distribution on alluvial fans. Journal of Sedimentary Research, 22(1):25–28.

Blom, A., Viparelli, E., and Chavarrías, V. (2016). The graded alluvial river: Profile concavity and downstream fining. Geophysical Research Letters, 43(12):6285–6293.

Bluck, B. J. (1964). Sedimentation of an alluvial fan in southern nevada. Journal of Sedimentary Research, 34(2).

Bonnet, S. and Crave, A. (2003). Landscape response to climate change: Insights from experimental modeling and implications for tectonic versus climatic uplift of topography. Geology, 31(2):123–126.

Brémand, F. (1994). A phase unwrapping technique for object relief determination. Optics and lasers in engineering, 21(1):49–60.

Bruning, J. H., Herriott, D. R., Gallagher, J., Rosenfeld, D., White, A., and Brangaccio, D. (1974). Digital wavefront measuring interferometer for testing optical surfaces and lenses. Applied optics, 13(11):2693–2703.

Bryant, M., Falk, P., and Paola, C. (1995). Experimental study of avulsion frequency and rate of deposition. Geology, 23(4):365–368.

Bull, W. B. (1964). Geomorphology of segmented alluvial fans in western Fresno County, California. US Government Printing Office.

Bull, W. B. (1977). The alluvial-fan environment. Progress in physical geography, 1(2):222–270.

Candy, I., Black, S., and Sellwood, B. (2004). Interpreting the response of a dryland river system to late quaternary climate change. Quaternary Science Reviews, 23(23):2513–2523.

Cesta, J. M. and Ward, D. J. (2016). Timing and nature of alluvial fan development along the chajnantor plateau, northern chile. Geomorphology, 273:412–427.

Charreau, J., Gumiaux, C., Avouac, J.-P., Augier, R., Chen, Y., Barrier, L., Gilder, S., Dominguez, S., Charles, N., and Wang, Q. (2009). The neogene xiyu formation, a diachronous prograding gravel wedge at front of the tianshan: Climatic and tectonic implications. Earth and Planetary Science Letters, 287(3):298–310.

Charru, F., Mouilleron, H., and Eiff, O. (2004). Erosion and deposition of particles on a bed sheared by a viscous flow. Journal of Fluid Mechanics, 519:55–80.

Chatanantavet, P., Lajeunesse, E., Parker, G., Malverti, L., and Meunier, P. (2010). Physically based model of downstream fining in bedrock streams with lateral input. Water Resour. Res, 46:W02518.

Chow, V. T. (1959). Open channel hydraulics.

Clarke, L., Quine, T. A., and Nicholas, A. (2010). An experimental investigation of autogenic behaviour during alluvial fan evolution. Geomorphology, 115(3):278–285.

Clarke, L. E. (2015). Experimental alluvial fans: Advances in understanding of fan dynamics and processes. Geomorphology, 244:135–145.

Clarke, L. E., Quine, T. A., and Nicholas, A. P. (2008). An evaluation of the role of physical models in exploring form–process feedbacks in alluvial fans. IAHS publication, (325):175–183.

Clevis, Q., de Boer, P., and Wachter, M. (2003). Numerical modelling of drainage basin evolution and three-dimensional alluvial fan stratigraphy. Sedimentary Geology, 163(1):85–110.

Coulthard, T., Macklin, M., and Kirkby, M. (2002). A cellular model of holocene upland river basin and alluvial fan evolution. Earth Surface Processes and Landforms, 27(3):269–288.

Davidson, S. K. and Hartley, A. J. (2010). Towards a quantitative method for estimating paleohydrology from clast size and comparison with modern rivers. Journal of Sedimentary Research, 80(7):688–702.

de Coulomb, C. A. (1821). Théorie des machines simples: en ayant égard au frottement de leurs parties et à la roideur des cordages. Bachelier.

de Haas, T., Ventra, D., Carbonneau, P. E., and Kleinhans, M. G. (2014). Debris-flow dominance of alluvial fans masked by runoff reworking and weathering. Geomorphology, 217:165–181.

Decelles, P. G., Gray, M., Ridgway, K., Cole, R., Pivnik, D., Pequera, N., and Srivastava, P. (1991). Controls on synorogenic alluvial-fan architecture, beartooth conglomerate (palaeocene), wyoming and montana. Sedimentology, 38(4):567–590.

Delorme, P., Voller, V., Paola, C., Devauchelle, O., Lajeunesse, E., Barrier, L., and Métivier, F. (2017). Self-similar growth of a bimodal laboratory fan. Earth Surface Dynamics, 5(2):239–252.

Denny, C. S. (1965). Alluvial fans in the Death Valley region, California and Nevada. Number 466. US Government Printing Office.

Densmore, A. L., Allen, P. A., and Simpson, G. (2007). Development and response of a coupled catchment fan system under changing tectonic and climatic forcing. Journal of Geophysical Research: Earth Surface, 112(F1).

Devauchelle, O., Petroff, A., Lobkovsky, A., and Rothman, D. H. (2011). Longitudinal profile of channels cut by springs. Journal of Fluid Mechanics, 667:38–47.

Drew, F. (1873). Alluvial and lacustrine deposits and glacial records of the upper-indus basin. Quarterly Journal of the Geological Society, 29(1-2):441–471.

Dubille, M. and Lavé, J. (2015). Rapid grain size coarsening at sandstone/conglomerate transition: similar expression in himalayan modern rivers and pliocene molasse deposits. Basin Research, 27(1):26–42.

Einstein, H. A. (1950). The bed-load function for sediment transportation in open channel flows. Number 1026. US Department of Agriculture.

Fedele, J. J. and Paola, C. (2007). Similarity solutions for fluvial sediment fining by selective deposition. Journal of Geophysical Research: Earth Surface, 112(F2).

Field, J. (2001). Channel avulsion on alluvial fans in southern arizona. Geomorphology, 37(1):93–104.

France-Lanord, C., Bourlès, D., and Gayer, E. (2001). Erosion rates determined from the accumulation of in situ-produced 10be in fluvial sediments of himalayan rivers. Journal of Asian Earth Sciences, 19(3A):21.

Fraser, G. S. and DeCelles, P. G. (1992). Geomorphic controls on sediment accumulation at margins of foreland basins. Basin Research, 4(3-4):233–252.

Frostick, L. E. and Reid, I. (1989). Climatic versus tectonic controls of fan sequences: lessons from the dead sea, israel. Journal of the Geological Society, 146(3):527–538.

Galloway, W. and Hobday, D. (1996). Terrigenous clastic depositional systems. applications to fossil fuel and groundwater resources, 2nd ed. Springer-Verlag.

Gaurav, K. (2016). Morphology of the Kosi megafan. PhD thesis, Institut de Physique du Globe de Paris, Université Paris Dierot, Sorbonne Paris Cité.

Gaurav, K., Métivier, F., Devauchelle, O., Sinha, R., Chauvet, H., Houssais, M., and Bouquerel, H. (2015). Morphology of the kosi megafan channels. Earth Surface Dynamics, 3(3):321.

Glover, R. E. and Florey, Q. (1951). Stable channel profiles. US Department of the Interior, Bureau of Reclamation, Hydr. Lab. Report.

Gómez-Villar, A. and Garcıa-Ruiz, J. (2000). Surface sediment characteristics and present dynamics in alluvial fans of the central spanish pyrenees. Geomorphology, 34(3):127–144.

Guerit, L., Barrier, L., Jolivet, M., Fu, B., and Métivier, F. (2016). Denudation intensity and control in the chinese tian shan: new constraints from mass balance on catchment-alluvial fan systems. Earth Surface Processes and Landforms, pages 1088–1106.

Guerit, L., Barrier, L., Métivier, F., Lui, Y., Narteau, C., Lajeunesse, É., Gayer, É., Meunier, P., and Ye, B. (2011). Reconstruction of the sediment trans-port conditions in the urumqi alluvial fan (northeast tian shan, china). In River, Coastal and Estuarine Morphodynamics: RCEM2011.

Guerit, L., Métivier, F., Devauchelle, O., Lajeunesse, E., and Barrier, L. (2014). Laboratory alluvial fans in one dimension. Physical Review E, 90(2):022203.

Guérit, L. (2014). Caractéristiques morpho-sédimentaires des cônes alluviaux et reconstitution de leurs paléo-flux d'eau et de sédiments: Exemples naturels du piedmont nord du Tian Shan (Xinjiang, Chine) et modélisation expérimentale. PhD thesis, Paris 7.

Hartley, A. J., Mather, A. E., Jolley, E., and Turner, P. (2005). Climatic controls on alluvial-fan activity, coastal cordillera, northern chile. Geological Society, London, Special Publications, 251(1):95–116.

Hartley, A. J., Weissmann, G. S., Nichols, G. J., and Warwick, G. L. (2010). Large distributive fluvial systems: characteristics, distribution, and controls on development. Journal of Sedimentary Research, 80(2):167–183.

Harvey, A. (2002). The role of base-level change in the dissection of alluvial fans: case studies from southeast spain and nevada. Geomorphology, 45(1):67–87.

Harvey, A. M. (2005). Differential effects of base-level, tectonic setting and climatic change on quaternary alluvial fans in the northern great basin, nevada, usa. Geological Society, London, Special Publications, 251(1):117–131.

Harvey, A. M., Mather, A. E., and Stokes, M. (2005). Alluvial fans: geomorphology, sedimentology, dynamics—introduction. a review of alluvial-fan research. Geological Society, London, Special Publications, 251(1):1–7.

Heller, P. L., Paola, C., Hwang, I.-G., John, B., and Steel, R. (2001). Geomorphology and sequence stratigraphy due to slow and rapid base-level changes in an experimental subsiding basin (xes 96-1). AAPG bulletin, 85(5):0817–0838.

Henderson, F. M. (1961). Stability of alluvial channels. Journal of the Hydraulics Division, 87(6):109–138.

Hinderer, M. (2012). From gullies to mountain belts: a review of sediment budgets at various scales. Sedimentary Geology, 280:21–59.

Hooke, R. L. (1968). Model geology: prototype and laboratory streams: discussion. Geological Society of America Bulletin, 79(3):391–394.

Horton, B. K., Constenius, K. N., and DeCelles, P. G. (2004). Tectonic control on coarse-grained foreland-basin sequences: An example from the cordilleran foreland basin, utah. Geology, 32(7):637–640.

Houssais, M. and Lajeunesse, E. (2012). Bedload transport of a bimodal sediment bed. Journal of Geophysical Research: Earth Surface, 117:(F4).

Ikeda, H. and Iseya, F. (1988). Experimental study of heterogeneous sediment transport. Environmental Research Center Papers, 12:1–50.

Jayko, A. (2005). Late quaternary denudation, death and panamint valleys, eastern california. Earth-Science Reviews, 73(1):271–289.

Jolivet, M., Barrier, L., Dominguez, S., Guerit, L., Heilbronn, G., and Fu, B. (2014). Unbalanced sediment budgets in the catchment–alluvial fan system of the kuitun river (northern tian shan, china): Implications for mass-balance estimates, denudation and sedimentation rates in orogenic systems. Geomorphology, 214:168–182.

Julien, P. Y. (2010). Erosion and sedimentation. Cambridge University Press.

Kiefer, E., Dorr, M. J., Ibbeken, H., and Gotze, H.-J. (1997). Gravity-based mass balance of an alluvial fan giant: the arcas fan, pampa del tamarugal, northern chile. Andean Geology, 24(2):165–185.

Kim, W., Paola, C., Voller, V. R., and Swenson, J. B. (2006). Experimental measurement of the relative importance of controls on shoreline migration. Journal of Sedimentary Research, 76(2):270–283.

Kuhlemann, J., Frisch, W., Székely, B., Dunkl, I., and Kázmér, M. (2002). Post-collisional sediment budget history of the alps: tectonic versus climatic control. International Journal of Earth Sciences, 91(5):818–837.

Lacey, G. (1930). Stable channels in alluvium. In Minutes of the Proceedings of the Institution of Civil Engineers, volume 229, pages 259–292. Thomas Telford-ICE Virtual Library.

Lajeunesse, E., Malverti, L., and Charru, F. (2010). Bed load transport in turbulent flow at the grain scale: Experiments and modeling. Journal of Geophysical Research: Earth Surface, 115(F4).

Latrubesse, E. M. (2015). Large rivers, megafans and other quaternary avulsive fluvial systems: A potential "who's who" in the geological record. Earth-Science Reviews, 146:1–30.

Le Hooke, R. B. and Rohrer, W. L. (1979). Geometry of alluvial fans: Effect of discharge and sediment size. Earth Surface Processes, 4(2):147–166.

Leier, A. L., DeCelles, P. G., and Pelletier, J. D. (2005). Mountains, monsoons, and megafans. Geology, 33(4):289–292.

Limare, A., Tal, M., Reitz, M., Lajeunesse, E., and Métivier, F. (2011). Optical method for measuring bed topography and flow depth in an experimental flume. Solid Earth, 2(2):143–154.

Liu, Y., Métivier, F., Gaillardet, J., Ye, B., Meunier, P., Narteau, C., Lajeunesse, E., Han, T., and Malverti, L. (2011). Erosion rates deduced from seasonal mass balance along the upper urumqi river in tianshan. Solid Earth, 2(2):283.

Liu, Y., Métivier, F., Éric Lajeunesse, Lancien, P., Narteau, C., Ye, B., and Meunier, P. (2008). Measuring bedload in gravel-bed mountain rivers: averaging methods and sampling strategies. Geodinamica Acta, 21(1-2):81–92.

Loiseleux, T., Gondret, P., Rabaud, M., and Doppler, D. (2005). Onset of erosion and avalanche for an inclined granular bed sheared by a continuous laminar flow. Physics of fluids, 17(10):103304.

Lustig, L. K. (1965). Clastic sedimentation in deep springs valley, California, volume 352. US Government Printing Office.

Macklin, M., Fuller, I., Lewin, J., Maas, G., Passmore, D., Rose, J., Woodward, J., Black, S., Hamlin, R., and Rowan, J. (2002). Correlation of fluvial sequences in the mediterranean basin over the last 200ka and their relationship to climate change. Quaternary Science Reviews, 21(14):1633–1641.

Makse, H. A., Cizeau, P., and Stanley, H. E. (1997a). Possible stratification mechanism in granular mixtures. Physical review letters, 78(17):3298–3301.

Makse, H. A., Havlin, S., King, P. R., and Stanley, H. E. (1997b). Spontaneous stratification in granular mixtures. Nature, 386(6623):379–382.

Malverti, L., Lajeunesse, E., and Métivier, F. (2008). Small is beautiful: Upscaling from microscale laminar to natural turbulent rivers. Journal of Geophysical Research: Earth Surface (2003–2012), 113(F4).

Mantz, P. A. (1977). Incipient transport of fine grains and flakes by fluids-extended shield diagram. Journal of the Hydraulics division, 103(ASCE 12992).

Marr, J., Swenson, J., Paola, C., and Voller, V. (2000). A two-diffusion model of fluvial stratigraphy in closed depositional basins. Basin Research, 12(3-4):381–398.

McCarthy, T. (1993). The great inland deltas of africa. Journal of African Earth Sciences (and the Middle East), 17(3):275–291.

McDonald, E. V., McFadden, L. D., and Wells, S. G. (2003). Regional response of alluvial fans to the pleistocene-holocene climatic transition, mojave desert, california. Special papers-geological society of America, pages 189–206.

Métivier, F. and Barrier, L. (2010). Alluvial landscape evolution: What do we know about metamorphosis of gravel-bed meandering and braided streams? Gravel-Bed Rivers: Processes, Tools, Environments, pages 474–501.

Métivier, F., Devauchelle, O., Chauvet, H., Lajeunesse, E., Meunier, P., B., K., Ashmore, P., Zhang, Z., Fan, Y., and Liu, Y. (2016). Geometry of meandering and braided gravel-bed threads from the bayanbulak grassland, tianshan, pr china. Earth Surface Dynamics, 4(1):273–283.

Métivier, F. and Gaudemer, Y. (1997). Mass transfer between eastern tien shan and adjacent basins (central asia): constraints on regional tectonics and topography. Geophysical Journal International, 128(1):1–17.

Métivier, F., Lajeunesse, E., and Devauchelle, O. (2017). Laboratory rivers: Lacey's law, threshold theory, and channel stability. Earth Surface Dynamics, 5(1):187.

Meunier, P., Métivier, F., Lajeunesse, E., Mériaux, A., and Faure, J. (2006). Flow pattern and sediment transport in a braided river: The "torrent de st pierre"(french alps). Journal of Hydrology, 330(3):496–505.

Meyer-Peter, E. and Müller, R. (1948). Formulas for bed-load transport. 2nd Mtg Int. Ass. Hydraulic Structures Research Stockholm, pages 39–64.

Miller, K. L., Reitz, M. D., and Jerolmack, D. J. (2014). Generalized sorting profile of alluvial fans. Geophysical Research Letters, 41(20):7191–7199.

Moody, L. F. (1944). Friction factors for pipe flow. Trans. Asme, 66(8):671–684.

Moore, J. and Howard, A. (2005). Large alluvial fans on mars. J. Geophys. Res, 110:E04005.

Muto, T. and Steel, R. J. (2004). Autogenic response of fluvial deltas to steady sea-level fall: Implications from flume-tank experiments. Geology, 32(5):401–404.

Muto, T., Steel, R. J., and Burgess, P. M. (2016). Contributions to sequence stratigraphy from analogue and numerical experiments. Journal of the Geological Society, 173(5):837–844.

Nicholas, A. P. and Quine, T. A. (2007). Modeling alluvial landform change in the absence of external environmental forcing. Geology, 35(6):527–530.

Oguchi, T. (1997). Late quaternary sediment budget in alluvial-fan–source-basin systems in japan. Journal of Quaternary Science, 12(5):381–390.

Ouriemi, M., Aussillous, P., and Guazzelli, E. (2009). Sediment dynamics. part 1. bed-load transport by laminar shearing flows. Journal of Fluid Mechanics, 636:295–319.

Ouriemi, M., Aussillous, P., Medale, M., Peysson, Y., and Guazzelli, É. (2007). Determination of the critical shields number for particle erosion in laminar flow. Physics of Fluids, 19(6):061706.

Palucis, M., Dietrich, W., Hayes, A., Williams, R., Gupta, S., Mangold, N., Newsom, H., Hardgrove, C., Calef III, F., and Sumner, D. (2014). The origin and evolution of the peace vallis fan system that drains to the curiosity landing area, gale crater, mars. J. Geophys. Res. Planets, 119:705–728.

Pang, C.-J., Li, Z.-X., Xu, Y.-G., Wen, S.-N., and Krapež, B. (2016). Climatic and tectonic controls on late triassic to middle jurassic sedimentation in northeastern guangdong province, south china. Tectonophysics, 677:68–87.

Paola, C., Heller, P. L., and Angevine, C. L. (1992a). The large-scale dynamics of grain-size variation in alluvial basins, 1: Theory. Basin Research, 4(2):73–90.

Paola, C., Mullin, J., Ellis, C., Mohrig, D. C., Swenson, J. B., Parker, G., Hickson, T., Heller, P. L., Pratson, L., Syvitski, J., et al. (2001). Experimental stratigraphy. GSA TODAY, 11(7):4–9.

Paola, C., Parker, G., Mohrig, D. C., and Whipple, K. X. (1999). The influence of transport fluctuations on spatially averaged topography on a sandy, braided fluvial fan.

Paola, C., Parker, G., Seal, R., Sinha, S. K., Southard, J. B., and Wilcock, P. R. (1992b). Downstream fining by selective deposition in a laboratory flume. Science, 258(5089):1757–1761.

Paola, C., Straub, K., Mohrig, D., and Reinhardt, L. (2009). The "unreasonable effectiveness" of stratigraphic and geomorphic experiments. Earth-Science Reviews, 97(1):1–43.

Parker, G. (1978a). Self-formed straight rivers with equilibrium banks and mobile bed. part 1. the sand-silt river. Journal of Fluid Mechanics, 89(01):109–125.

Parker, G. (1978b). Self-formed straight rivers with equilibrium banks and mobile bed. part 2. the gravel river. Journal of Fluid Mechanics, 89(01):127–146.

Parker, G. (1999). Progress in the modeling of alluvial fans. Journal of Hydraulic Research, 37(6):805–825.

Parker, G., Paola, C., Whipple, K. X., and Mohrig, D. (1998a). Alluvial fans formed by channelized fluvial and sheet flow. i: Theory. Journal of Hydraulic Engineering, 124(10):985–995.

Parker, G., Paola, C., Whipple, K. X., Mohrig, D., Toro-Escobar, C. M., Halverson, M., and Skoglund, T. W. (1998b). Alluvial fans formed by channelized fluvial and sheet flow. ii: Application. Journal of Hydraulic Engineering, 124(10):996–1004.

Poisson, B. (2002). Impact du climat et de la tectonique sur l'évolution géomorphologique d'un piémont-Exemple du piémont Nord du Tian Shan depuis la fin du Pléistocène. PhD thesis, Université Paris Sud-Paris XI.

Poisson, B. and Avouac, J.-P. (2004). Holocene hydrological changes inferred from alluvial stream entrenchment in north tian shan (northwestern china). The Journal of Geology, 112(2):231–249.

Pope, R. J., Candy, I., and Skourtsos, E. (2016). A chronology of alluvial fan response to late quaternary sea level and climate change, crete. Quaternary Research, 86(2):170–183.

Powell, E. J., Kim, W., and Muto, T. (2012). Varying discharge controls on timescales of autogenic storage and release processes in fluvio-deltaic environments: Tank experiments. Journal of Geophysical Research: Earth Surface (2003–2012), 117:(F2).

Rachocki, A. and Church, M. A. (1990). Alluvial fans: a field approach. John Wiley & Sons.

Reitz, M. D. and Jerolmack, D. J. (2012). Experimental alluvial fan evolution: Channel dynamics, slope controls, and shoreline growth. Journal of Geophysical Research: Earth Surface (2003–2012), 117(F2).

Reitz, M. D., Jerolmack, D. J., Lajeunesse, E., Limare, A., Devauchelle, O., and Métivier, F. (2014). Diffusive evolution of experimental braided rivers. Physical Review E, 89(5):052809.

Reitz, M. D., Jerolmack, D. J., and Swenson, J. B. (2010). Flooding and flow path selection on alluvial fans and deltas. Geophysical Research Letters, 37(6).

Rice, S. (1999). The nature and controls on downstream fining within sedimentary links. Journal of Sedimentary Research, 69(1):32–39.

Ritter, J. B., Miller, J. R., Enzel, Y., and Wells, S. G. (1995). Reconciling the roles of tectonism and climate in quaternary alluvial fan evolution. Geology, 23(3):245–248.

Rohais, S. (2007). Architecture stratigraphique et flux sédimentaires sur la marge sud du golfe de Corinthe (Grèce): Analyse de terrain, modélisations expérimentales et numériques. PhD thesis, Rennes 1.

Rohais, S., Bonnet, S., and Eschard, R. (2012). Sedimentary record of tectonic and climatic erosional perturbations in an experimental coupled catchment-fan system. Basin Research, 24(2):198–212.

Romans, B. W., Castelltort, S., Covault, J. A., Fildani, A., and Walsh, J. (2016). Environmental signal propagation in sedimentary systems across timescales. Earth-Science Reviews, 153:7–29.

Saito, K. and Oguchi, T. (2005). Slope of alluvial fans in humid regions of japan, taiwan and the philippines. Geomorphology, 70(1):147–162.

Schumm, S. A., Mosley, M. P., and Weaver, W. (1987). Experimental fluvial geomorphology. John Wiley and Sons Inc., New York, NY.

Seizilles, G., Devauchelle, O., Lajeunesse, E., and Métivier, F. (2013). Width of laminar laboratory rivers. Physical Review E, 87(5):052204.

Seizilles, G., Lajeunesse, E., Devauchelle, O., and Bak, M. (2014). Cross-stream diffusion in bedload transport. Physics of Fluids (1994-present), 26(1):013302.

Seizilles de Mazancourt, G. (2013). Forme d'équilibre d'une rivière. PhD thesis, Paris 7.

Shankar, P. and Kumar, M. (1994). Experimental determination of the kinematic viscosity of glycerol-water mixtures. Proceedings of the Royal Society of London. Series A: Mathematical and Physical Sciences, 444(1922):573–581.

Shields, A. (1936). Anwendung der ahnlichkeits mechanik und der turbulenz-forschung auf die geschiebebewegung. Preussische Versuchsanstalt fur Wasserbau und Schiffbau, 26:524–526.

Singer, M. B. (2008). Downstream patterns of bed material grain size in a large, lowland alluvial river subject to low sediment supply. Water Resources Research, 44(12).

Sinha, R. (1998). On the controls of fluvial hazards in the north bihar plains, eastern india. Geological Society, London, Engineering Geology Special Publications, 15(1):35–40.

Sinha, R. (2009). The great avulsion of kosi on 18 august 2008. Current Science (00113891), 97(3).

Slingerland, R. and Smith, N. D. (2004). River avulsions and their deposits. Annu. Rev. Earth Planet. Sci., 32:257–285.

Smith, G. H. S. and Ferguson, R. I. (1996). The gravel-sand transition: flume study of channel response to reduced slope. Geomorphology, 16(2):147–159.

Stanistreet, I. and McCarthy, T. (1993). The okavango fan and the classification of subaerial fan systems. Sedimentary Geology, 85(1):115–133.

Stock, J. D., Schmidt, K. M., and Miller, D. M. (2008). Controls on alluvial fan long-profiles. Geological Society of America Bulletin, 120(5-6):619–640.

Van Dijk, M., Postma, G., and Kleinhans, M. G. (2009). Autocyclic behaviour of fan deltas: an analogue experimental study. Sedimentology, 56(5):1569–1589.

Viparelli, E., Solari, L., and Hill, K. (2015). Downstream lightening and upward heavying: Experiments with sediments differing in density. Sedimentology, 62(5):1384–1407.

Waters, J., Jones, S., and Armstrong, H. (2010). Climatic controls on late pleistocene alluvial fans, cyprus. Geomorphology, 115(3):228–251.

Weissmann, G., Bennett, G., and Lansdale, A. (2005). Factors controlling sequence development on quaternary fluvial fans, san joaquin basin, california, usa. Special Publication-Geological Society of London, 251:169.

Weissmann, G., Hartley, A., Nichols, G., Scuderi, L., Olson, M., Buehler, H., and Banteah, R. (2010). Fluvial form in modern continental sedimentary basins: Distributive fluvial systems. Geology, 38(1):39–42.

Weissmann, G. S., Mount, J. F., and Fogg, G. E. (2002). Glacially driven cycles in accumulation space and sequence stratigraphy of a stream-dominated alluvial fan, san joaquin valley, california, usa. Journal of Sedimentary Research, 72(2):240–251.

Whipple, K. X., Parker, G., Paola, C., and Mohrig, D. (1998). Channel dynamics, sediment transport, and the slope of alluvial fans: Experimental study. The Journal of geology, 106(6):677–694.

Whipple, K. X. and Trayler, C. R. (1996). Tectonic control of fan size: the importance of spatially variable subsidence rates. Basin Research, 8(3):351–366.

Whittaker, A. C., Duller, R. A., Springett, J., Smithells, R. A., Whitchurch, A. L., and Allen, P. A. (2011). Decoding downstream trends in stratigraphic grain size as a function of tectonic subsidence and sediment supply. Geological Society of America Bulletin, 123(7-8):1363–1382.

Wilcock, P. R. and Crowe, J. C. (2003). Surface-based transport model for mixed-size sediment. Journal of Hydraulic Engineering, 129(2):120–128.

Williams, R. M., Grotzinger, J. P., Dietrich, W., Gupta, S., Sumner, D., Wiens, R., Mangold, N., Malin, M., Edgett, K., Maurice, S., et al. (2013). Martian fluvial conglomerates at gale crater. science, 340(6136):1068–1072.

Williams, R. M., Zimbelman, J. R., and Johnston, A. K. (2006). Aspects of alluvial fan shape indicative of formation process: A case study in southwestern california with application to mojave crater fans on mars. Geophysical research letters, 33(10).

Yalin, M. S. and Karahan, E. (1979). Inception of sediment transport. Journal of the hydraulics division, 105(11):1433–1443.

UNIVERSITÉ SORBONNE PARIS CITÉ

Morphologie des cônes alluviaux

par

Pauline Delorme

Résumé

Les cônes alluviaux sont des dépôts sédimentaires qui se mettent en place à la sortie des reliefs en érosion. Cette position leur confère un rôle d'archive sédimentaire. Leur géométrie est déterminée par les trois paramètres clés que sont le débit d'eau, la taille des sédiments et le débit de sédiment. Dans ce manuscrit, nous présentons trois séries d'expériences qui permettent de quantifier indépendamment l'influence de chacun des paramètres d'entrée sur la morphologie du cône. Nous montrons que le profil longitudinal du cône est contrôlé par la rivière qui le construit.

Lorsque le flux de sédiment est faible, la rivière alimentant le cône est au seuil de mise en mouvement des sédiments. En conséquence, sa pente, et donc celle du cône, dépendent uniquement de la taille des sédiments charriés et du débit d'eau. Cette pente augmente avec la taille des sédiments et diminue avec le débit d'eau.

Les cônes composés de sédiment de mobilité différentes permettent d'illustrer l'influence de la taille des sédiments sur leur pente. Dans nos expériences, à l'instar des cônes naturels, le dépôt est ségrégé: les sédiments les moins mobiles se déposent en amont du cône, où la pente est plus forte. Cette ségrégation nous permet d'estimer la composition du mélange initial à partir de la géométrie du dépôt.

Enfin, nous avons montré que lorsque le débit sédimentaire augmente, la pente du cône s'élève au dessus de sa valeur seuil. Dans ce cas, puisque la rivière dépose les sédiments, le débit sédimentaire diminue vers l'aval, ce qui induit un profil concave. Nous montrons ainsi que la pente proximale du cône enregistre la valeur de ce débit sédimentaire.

Finalement, nous présentons des résultats préliminaires permettant de prendre en compte l'enregistrement de la variation des forçages dans la stratigraphie du cône, et envisageons des pistes pour appliquer ces observations aux cônes naturels.

Mots clefs: cône alluvial, rivière, seuil de mise en mouvement, archive sédimentaire

Abstract

Alluvial fans are sedimentary deposits growing at the outlet of drainage areas. This position makes them valuable sedimentary records. Three key parameters determine their geometry: the water discharge, the sediment size and the sediment discharge. In this manuscript, based on three series of experiments, we quantify independently the influence of each parameter on the structure of the deposit. We find that the morphology of the fan is controlled by the river that builds it.

For a low sediment discharge, the river that feeds the fan is at the threshold of sediment motion. As a result, its slope, and therefore that of the fan, depend only on the size of the sediment and on the water discharge. The slope increases with sediment size and decreases with water discharge.

Experimental alluvial fans composed of bimodal sediment, like to their natural counterparts, are segregated. The less mobile sediments are deposited first, near the fan apex, where the slope is steeper. This segregation allows us to estimate the composition of the sediment mixture from the fan geometry.

When the sediment discharge injected at the apex increases, the slope of the fan departs from its threshold value. Sediments are deposited along the fan, thus causing the sediment discharge to decrease downstream, generating a concave profile. As a consequence, the proximal slope of the fan records the sediment discharge.

Finally, we present preliminary results showing how the stratigraphy of the fan records variations of the forcing (sediment and water discharges). We then discuss the applicability of these observations to the natural fans.

Key words: alluvial fan, river, threshold of motion, sedimentary record